

HIGH INTENSITY, HIGH CONTRAST LASER SOLID INTERACTIONS WITH SHORT PULSES

by

Franklin Jon Dollar

A dissertation submitted in partial fulfillment
of the requirements for the degree of
Doctor of Philosophy
(Applied Physics)
in The University of Michigan
2012

Doctoral Committee:

Professor Karl Michael Krushelnick, Chair
Professor R. Paul Drake
Assistant Professor Alexander George Roy Thomas
Research Professor Dale William Litzenberg
Research Scientist Anatoly M. Maksimchuk
Research Scientist Victor P. Yanovsky

© Franklin Jon Dollar 2012

All Rights Reserved

For those who could not be here, and for those who have yet to come.

ACKNOWLEDGEMENTS

There could not have been a better advisor for my graduate research than Professor Karl Krushelnick, who gave me the opportunity to complete this dissertation. I am thankful for his advising, complemented by the dream team that is the High Field Science group. The simulations performed for this doctoral work were made possible by the long conversations with Professor Alec Thomas, whose patience knows no bounds. The typography and readability of all publications that I have presented are a direct result of the support provided by Dr. Louise Willingale. The scale and complexity of the experiments became feasible with the instruction and supervision of Dr. Anatoly Maksimchuk. None of the experiments would be possible without the continued operation and maintenance of the HERCULES Laser, which I am indebted to the time and effort of Dr. Victor Yanovsky, as well as Dr. Vladmir Chvykov, Pascal Rousseau, and Dr. Galina Kalinchenko. I also possess the deepest respect for the Applied Physics Program at University of Michigan, and am extremely thankful for Charles Sutton, Cynthia McNabb, and Professors Brad Orr, Cagliyan Kurdak, and Roy Clark.

I could not have made it to graduate school without the world class mentorship provided by Diana Lizarraga, Dr. Michele DeCoteau, Ruth Hopper, and Bridget Wilson from the University of California, Berkeley. I am extremely grateful for the opportunities provided by Dr. Eric Gullikson and the Center for X-Ray Optics, which was made possible through Professor David Attwood, for whom I dedicate Chapter VI. Before University I had the teachers at Geyserville High School, whom I would

like to thank. In particular, Brad Goodhart, Keith Muelrath, and Fernando Nugent are key people pushing me towards the academy. The American Indian Science and Engineering Society hold a special place in my heart, and I would like to thank the community and the Council of Elders for their support and guidance.

I would like to thank my hawk brother Dr. Chris McGuffey, as well as the amazing Dr. Stefan Kneip, whose collaboration proved invaluable. I would also like to thank Calvin Zulick for the help with the neutron experiment among others; Dr. Channing Huntington for the premium mentorship; the graduate students and research scientists in CUOS; Nicole Wilson for being a pillar of support; Pedro Gomez for being the other pillar; Dr. Takeshi Matsuoka for being my instructor and Sensei; and Joanna Hernandez for more than words can say.

Random things that I must thank are the Brick House; the Fightin' First Years; Michelle and the Killer Flamingos; Miss Mary and La Familia; the Native Caucus; Delta Airlines; Jupiter Laser Facility; invertebrates that give themselves to science; the Hot Tub Time Machine; iPhones; the Laser Plasma Interactions Group at Imperial College; Karl again; Tedford and Hoke; the Multilayer Optics Group at LLNL; and Douglas Adams.

This doctoral work was supported financially by the National Science Foundation through the Physics Frontier Center FOCUS (Grant No. PHY-0114336) and Graduate Research Fellowship Program (Grant No. DGE-0718128), as well as by the Office of Naval Research and the Defense Threat Reduction Agency. I would like to acknowledge the OSIRIS consortium of UCLA and IST Portugal for the use of OSIRIS framework. Simulations were performed on the Nyx Cluster at Center for Advanced Computing at the University of Michigan, Ann Arbor.

TABLE OF CONTENTS

DEDICATION	ii
ACKNOWLEDGEMENTS	iii
LIST OF FIGURES	viii
LIST OF NOMENCLATURE	xiii
ABSTRACT	xvi
CHAPTER	
I. Introduction & Motivation	1
1.1 Laser Based Acceleration	2
1.1.1 Electron Acceleration	2
1.1.2 Ion Acceleration	5
1.1.3 Laser Technology	8
1.2 Laser Based Light Sources	9
1.2.1 Hard X-ray Sources	10
1.2.2 Soft X-Ray Sources	11
1.3 Applications of Laser Based Sources	12
1.3.1 Ion Applications	12
1.3.2 Nuclear Reactions	14
1.4 Comparison with Existing Facilities	20
1.5 Thesis Organization	21
II. Theoretical Background	22
2.1 Laser Physics	22
2.1.1 Dispersion	22
2.1.2 Nonlinear Effects	25
2.1.3 Laser Contrast	27
2.2 Single Electron Dynamics	30

2.2.1	Ionization	30
2.2.2	Relativistic Motion	34
2.2.3	Ponderomotive Force	36
2.2.4	Circular Polarization	39
2.3	Laser Plasma Interactions	40
2.3.1	Relativistic Effects	40
2.3.2	Absorption	42
2.3.3	Parametric Instabilities	45
2.3.4	Radiation Generation	46
2.4	Ion Acceleration Mechanisms	48
2.4.1	Target Normal Sheath Acceleration	48
2.4.2	Radiation Pressure Acceleration	50
2.4.3	Breakout Afterburner	52
2.4.4	Directed Coulomb Explosion	53
2.4.5	Ion Acceleration Challenges	54
III. Methods & Capabilities		55
3.1	HERCULES Laser Facility	55
3.1.1	Solid Target Experimental Area	58
3.2	High Contrast Capabilities	58
3.2.1	Pre-compression Cleaning	58
3.2.2	Staged Plasma Mirrors	61
3.3	High Intensity Capabilities	67
3.4	Diagnostics	70
3.4.1	Optical Diagnostics	71
3.4.2	Particle Diagnostics	72
3.4.3	X-Ray Diagnostics	77
3.5	Computational Capabilities	80
IV. Control of ion spectra		82
4.1	Introduction	82
4.2	Experimental Setup	84
4.2.1	Prepulse introduction	84
4.3	Ion Spectra Results	86
4.3.1	Numerical Simulations	89
4.4	Discussion	91
4.4.1	Implications for Ion Acceleration	93
4.4.2	Monoenergetic Ion Acceleration	94
4.5	Conclusions	96
V. Polarization effects on thin targets		98
5.1	Introduction	98

5.1.1	Light-sail Radiation Pressure Acceleration	99
5.2	Experimental Setup	100
5.3	Normal Incidence Results	102
5.4	High Intensity Absorption	105
5.4.1	S Polarization	106
5.4.2	P Polarization	107
5.5	Discussion and Simulations	107
5.6	Thin Foil Absorption at High Intensities	109
5.7	Simulation Validation	114
5.8	Outlook of Radiation Pressure Acceleration	117
5.9	Conclusions	118
 VI. High-order harmonic generation from solid density targets .		119
6.1	Introduction	119
6.2	Plasma Scale Length	120
6.3	Experimental Setup	121
6.3.1	EUV Spectrometer	123
6.4	Scale Length Results	124
6.5	2D Simulations & Discussion	126
6.6	1D Simulations	129
6.7	Attosecond Generation	130
6.8	Conclusions	131
 VII. Conclusion & Future Outlooks		132
7.1	Thesis Discussion	132
7.2	Future Applications & Outlook	133
 APPENDICES		135
 BIBLIOGRAPHY		137

LIST OF FIGURES

Figure

1.1	A 2 dimensional particle-in-cell simulation of the electron density of a laser wakefield acceleration interaction for a high intensity laser pulse. Due to the symmetry of the electric potential this nonlinear regime is termed the “bubble regime”. Figure courtesy of [126]. . .	4
1.2	A wedged target and the radiochromic film that detected the accelerated protons. There are clearly two beams of protons generated, that come normal from the rear surfaces. Note that there is not a third beam in the laser direction. Data courtesy of [52].	6
1.3	Schematic diagram of a Chirped Pulse Amplification laser system. .	9
1.4	Energy loss of protons in liquid water. The sharp region where most of the energy is deposited is known as the Bragg peak.	13
1.5	Neutron time-of-flight data from a (d,Li) interaction using the HERCULES laser.	17
1.6	A view of one of the two laser bays at the National Ignition Facility. Credit: Lawrence Livermore National Laboratory.	19
2.1	3rd order autocorrelation of the HERCULES laser pulse without cleaning (black) and with cleaning (red). The measurements are taken at low amplification, with several data points at full power given by the square crosses.	28
2.2	1D Hydrodynamic simulations of intensity v. preplasma scale length of the main pulse for a variety of targets at the time that the main pulse arrives.	29
2.3	Diagram of tunneling ionization. The superposition of the standard Coulomb potential (a) and the intense laser potential (b) produce a situation where a narrow barrier traps the electron (c). When the laser potential is sufficiently large the electron can freely escape in barrier suppression ionization.	32
2.4	Appearance intensities for various elements. Note that the presence of Si ¹³⁺ indicates an intensity greater than 10 ²¹ Wcm ⁻²	33
2.5	Electron motion in a linear plane wave at the electron rest frame. The left figure is for a small a_0 (0.3) and the right is for a large a_0 (100).	37

2.6	Electric field solution for a reflected beam of a $2\omega_0$ driver for low amplitudes (blue) and high amplitudes (red). The bottom graph shows the Fourier transform of the produced spectra, and the harmonics are clearly visible.	47
3.1	Schematic diagram of the HERCULES laser system.	56
3.2	Schematic diagram of a Treacy double pair grating compressor. Negative Group Velocity dispersion occurs since the optical path length of blue light is shorter than that of red, compensating for dispersion elsewhere in the laser system. The separation of each pair controls the amount of dispersion added.	57
3.3	Typical experimental setup of the solid target experimental area. Drawing not to scale.	59
3.4	(a) Full regen shown with XPW engaged (red) and without (blue). (b) Comparison between 30 TW shots (blue) and the full regen with XPW engaged (red). This shows that there is no significant increase in contrast for full power shots.	59
3.5	(a) Photograph of plasma mirror during the experiment. The plasma expands after the interaction into a jet near normal to the surface. (b) Schematic drawing of the dual plasma mirror configuration. . . .	62
3.6	(a) The reflectivity of a single plasma mirror as a function of position relative to the focus of the OAP for the case of without XPW (red) and with XPW (blue). (b) The measured contrast improvement with a pair of plasma mirrors. With two plasma mirrors the nanosecond prepulse is below the detection threshold of the diode, indicating contrast improvement of better than 3 orders.	63
3.7	1D Hydrodynamic simulations of the HERCULES prepulse at plasma mirror intensities. (a) The electron density profile for various intensities in Wcm^{-2} . Also shown is the comparison between the XPW and non XPW prepulse at (b) $4 \times 10^{15} \text{Wcm}^{-2}$ and (c) $4 \times 10^{16} \text{Wcm}^{-2}$	66
3.8	(a) CCD image of the focal spot. (b) Logarithmic line-out of the focal spot.	70
3.9	Schematic Diagram of a Thomson Parabola ion spectrometer. The particles are deflected with respect to energy due to the magnetic field, and are deflected by the charge to mass ratio by the electric field. X-rays and neutral atoms produce a zero order point for alignment.	74
3.10	Thomson parabola trace with overlays from the analytical solution for particle motion for various atoms. The straight through is used as a reference.	75
3.11	(a) Stopping power of a proton through liquid water. Note that the stopping power is almost entirely due to the electrons. (b) The energy loss of protons through water for several different initial energies. The point at which all remaining energy is abruptly lost is known as the Bragg peak.	77

3.12	Diagram of CR-39 energy calibration. Foils are in strips along a piece of CR-39, allowing for divergence information in one axis and energy information in the other.	78
3.13	Focal scan of a 550 micron silicon target at high contrast. Signal is clearly peaked, showing the region of highest intensity.	79
4.1	Beam diagnostic images of the laser far field after plasma mirrors. No difference in intensity is observed for prepulse being present compared to regen amplification or at full power without prepulse.	86
4.2	Energy spectra for prepulse (50 nm Si_3N_4) and clean pulse (30 nm Si_3N_4) for (a) Protons and (b) Carbon 4+. The sharp drop on the clean pulse case is due to the edge of the detector. The raw traces for these spectra are also shown for (c) clean pulse and (d) prepulse.	87
4.3	(Color online) (a) Proton spectra for prepulse case for 0 and 45 degrees incidence for 1 μ m Mylar targets. (b) Prepulse proton spectra for 3 target thicknesses. (c) Maximum proton energy for prepulse and clean pulse case. Lines are shown for visual aid only.	88
4.4	Raw TP traces of 6 successive shots on 1 μ m Mylar with prepulse present. The proton spectra is clearly displays quasi-monoenergetic features in every shot.	89
4.5	PIC simulation results at 202 fs of proton energy spectra for clean pulse (a) and prepulse (c) for 1 μ m carbon target at target normal ($p_y \approx 0$) with charge density individually normalized to 1 for comparison. Proton phase space P_x v. P_y are also shown for clean pulse (b) and prepulse (d) in units of normalized momentum. <i>Note that the color scale is logarithmic.</i>	92
4.6	PIC simulations at 202 fs of proton density profile for clean pulse and prepulse.	93
4.7	Deuteron energy spectra from 13 μ m Mylar target with prepulse present.	96
5.1	Schematic Diagram of experimental setup for absorption measurements.	102
5.2	Proton energy spectra for both right-hand circular and linearly polarized laser pulse interactions for a) 30 nm and b) 100 nm thickness Si_3N_4 targets. Maximum proton energy vs. target thickness is also shown (c) with lines shown as visual aid only.	103
5.3	Signal on NaI scintillator for varying focal position for both linear and circular polarization at normal incidence. Target is a silicon wafer. A quadratic fit is made to the data points to identify the optimal focal position. Intensities of interest are noted. Focal positions are relative.	104
5.4	Electron energy spectra for right-hand circular (solid) and linear (dashed) polarized laser pulse interaction for a) 30 nm and b) 100 nm Si_3N_4 targets.	105
5.5	Reflection profiles for S polarization. The reflectivity at 800 nm is shown in the upper right, while the focal position is shown in the upper left.	106

5.6	Reflection profiles for P polarization. The reflectivity at 800 nm is shown in the upper right, while the focal position is shown in the upper left.	107
5.7	C_6^+ energy spectra for a) right-hand circular and b) linear polarized laser pulse interaction for 30 nm Si_3N_4 targets. Detector background levels are shown for comparison. Raw spectra are shown for c) circular and d) linear polarization, with the high energy carbon peak denoted by the red circle.	110
5.8	PIC simulated proton energy spectra overlaid with experimental spectra. Circular results are shown for a thin (a) and thick (c) target, while linear results are shown for thin (b) and thick (d) targets. The simulation results are shown with the dashed line.	110
5.9	Proton density space of OSIRIS 2D PIC simulations for a) thin linear, b) thick linear, c) thin circular, and d) thick circular cases taken at 168 fs. For the circular case, the mean target displacement along the laser axis v. time is shown in e), and the effective temperature v. time is shown in f). “Thin” and “thick” correspond to a total target thickness of 36 nm and 108 nm respectively with the target left justified at an x position of 0.	112
5.10	Stopping power of protons in the MCP electrode. Protons with an energy of 60-80 keV will be fully stopped in the electrode, as highlighted in red.	113
5.11	PIC simulations for circular polarization and 30 nm targets. Rear proton density (Top) and the rear proton phase space (bottom) are shown. The base case is (a), quadratic particle weighting is shown in (b), 1.5 nm resolution is shown in (c), and 8 times the particles per cell is shown in (d).	116
6.1	Experimental conditions for generating a slightly perturbed reflected spectra from (a) a sharp density profile, (b) a strongly anharmonic spectra from a nominal scale length value, and (c) a highly modulated spectra from a long scale length.	122
6.2	Schematic diagram of the HHG experiment. The source is imaged to the detector plane via a cylindrically focusing variable-line-space grating. The detector is a direct detection x-ray CCD.	123
6.3	Raw, single shot EUV spectrometer images (left) and response corrected lineouts (right) for ultra-sharp density profile (a), nominal c/ω_p scale length (b), and λ scale lengths (c). The Al x-ray filter causes a sharp drop in transmission at 172 angstroms.	125
6.4	EUV Spectrometer data displaying features of half-harmonics (a), sidebands (b), and split harmonics (c) while is the transitional region of scale length. These are indicative of parametric harmonic generation from mechanisms such as SRS and TPD.	126
6.5	PIC Simulations of the reflected spectra for Scale Length of (a) $\lambda_0/160$, (b) $\lambda_0/5$, (c) $\lambda_0/2$, (d) and c/ω_p	128

6.6	The conversion of fundamental laser frequency into other frequencies as a function of scale length from 1D simulations of a circular polarized pulse are shown in (a). The rapid rise due to parametric instabilities can be observed. The total conversion efficiency into high harmonic generation from the 2D simulations is shown in (b). The optimal scale length occurs close to the plasma wavelength.	129
6.7	2D PIC simulations of the attosecond pulse train generated in the interaction taken along the specular direction for scale lengths of $\lambda/(2\pi)$ and (b) λ	130

LIST OF NOMENCLATURE

Fundamental Constants

c	Speed of Light in Vacuum $\simeq 2.99 \times 10^8 \text{ms}^{-1}$
e_c	Charge of Electron $\simeq 1.60 \times 10^{-19} \text{ C}$
ϵ_0	Permittivity of Free Space $\simeq 8.85 \times 10^{-12} \text{Fm}^{-1}$
m_e	Mass of electron $\approx 9.11 \times 10^{-31} \text{ kg}$
m_p	Mass of proton $\approx 1.67 \times 10^{-27} \text{ kg}$

Greek Symbols

χ	Electric Susceptibility
γ	Lorentz Factor
$\Delta\omega_0$	Laser Bandwidth
ω_0	Laser Frequency
ω_p	Electron Plasma Frequency
Φ	Ionization Energy (Work Function)
δ	Skin Depth
τ_0	Diffraction Limited Pulse Duration

Roman Symbols

I_0 Peak Intensity

k_0 Wavenumber

n_{crit} or n_c Plasma Critical Density

$n(\omega)$ Index of Refraction

Acronyms

CCD Charged Couple Device

CPA Chirped Pulse Amplification

CUOS Center for Ultrafast Optical Science

EUV Extreme Ultraviolet

FWHM Full Width at Half Maximum

GVD Group Velocity Dispersion

HERCULES High Energy High Repetition Rate CUOS Laser System

HHG High Harmonic Generation

LWFA Laser Wakefield Acceleration

MCP Microchannel Plate

NIR Near Infrared

OAP Off-axis Parabolic Mirror

PIC Particle-in-cell

RF Radio Frequency

RPA	Radiation Pressure Acceleration
SiN	Silicon Nitride (Si_3N_4)
SPM	Self-Phase Modulation
SRS	Stimulated Raman Scattering
TP	Thomson Parabola Ion Spectrometer
TPD	Two-Plasmon Decay
TNSA	Target Normal Sheath Acceleration
VFP	Vlasov-Fokker-Planck
XPW	Cross-Polarized Wave Generation

ABSTRACT

HIGH INTENSITY, HIGH CONTRAST LASER SOLID INTERACTIONS WITH SHORT PULSES

by

Franklin Jon Dollar

Doctor of Philosophy

This thesis describes experimental discoveries related to laser-based ion acceleration from thin foils and the production of high brightness x-rays from high order harmonic generation. High power femtosecond lasers are ideally suited for use as tabletop particle accelerators since their short pulse duration enables very high intensities to be generated at high repetition rates from a compact laser. However, if laser pulse energy arrives before the main short pulse, it can interact with the target to cause ablation making high intensity investigations of laser-solid interactions difficult. In the following experiments, the laser pulse-to-pedestal contrast was improved by 15 orders of magnitude out to nanosecond timescales, allowing for excellent control over the interaction of a short pulse with solid density material. A sharply-rising laser pulse with 50 TW of power was focused to a 1.2 micron focal spot, achieving intensities over 10^{21}Wcm^{-2} . Protons accelerated due to sheath acceleration were studied in ultrathin targets. By sculpting the plasma density using shaped ultrafast pulses, control over the proton and ion spectra was also demonstrated. Finite spot effects from circular polarized laser pulses produced efficient acceleration for ultrathin foils, which resulted

from the efficient conversion of laser light into high energy electrons. Finally, as the laser pulse drives the critical electron density relativistically, harmonics of the driving laser are produced. Harmonics up to order 60th were observed. It was observed that for a plasma scale length beyond a threshold value, parametric instabilities strongly modulated the harmonic spectra. Numerical simulations were performed to support the physical interpretation.

CHAPTER I

Introduction & Motivation

The 20th century has witnessed a rapid expansion in the understanding of physics, a great part of which is due to the influence of particle accelerators. Once E. O. Lawrence demonstrated that electrons gyro-rotating in a magnetic field can be accelerated with an alternating radio frequency (RF) electric field [76], a path was developed for the eventual development of high energy particle accelerators and high brightness light sources. While RF acceleration has proven to be a very successful tool in advancing the maximum particle energy and brightest photon flux achievable in a laboratory, facilities that exist for scientific research remain fairly scarce. This is largely due to their immense size and cost.

However, recent advances in short pulse¹ laser technology have allowed for the generation of laser intensities in which the electric field of the laser exceeds hundreds of teravolts per meter. The interactions of such high fields with matter result in near instantaneous plasma formation, and the fields themselves are capable of driving electrons to velocities approaching the speed of light. The effective mass of the electron changes as the velocity increases, so the interactions become complex and are inherently nonlinear. The amount of charge separation that is able to occur in such an interaction gives rise to acceleration gradients many orders of magnitude higher

¹Throughout this thesis, the phrase “short pulse” will refer to light with a full width at half maximum duration of less than 100 femtoseconds (10^{-15} seconds)

those found in conventional particle accelerators, enabling the potential development of table top particle accelerators. Rapidly accelerating and decelerating electrons generates radiation, also opening up the possibility of a tabletop high brightness light source. The following sections will act as a short survey into these novel tabletop sources and their mechanisms, and discuss why a laser based solution can be more attractive than conventional technology, with a look at what is currently capable with conventional methods.

1.1 Laser Based Acceleration

1.1.1 Electron Acceleration

The laser has experienced rapid development and correspondingly a rapid rise in peak power since its invention just over fifty years ago. The advent of Chirped Pulse Amplification (CPA) [121] in 1985 has allowed for the construction of compact laser systems exceeding many terawatts in peak power. However, 6 years earlier in a display of incredible foresight, Tajima and Dawson from UCLA simulated the interaction of such a laser with a low density plasma and observed that the plasma waves formed in the wake of the laser were able to accelerate trapped electrons to relativistic energies². The resonant condition for this laser wakefield acceleration (LWFA) required that the driving pulse be contained within half of the plasma relativistic wavelength, necessitating the use of short pulse lasers. While some early experiments using clever schemes to emulate a short pulse driver showed some success [26, 25, 99, 95, 130], the availability of terawatt class short pulse lasers enabled the generation of monoenergetic electron beams at MeV to GeV energies [89, 47, 41, 78]. With acceleration distances of less than a few centimeters and acceleration gradients of many tens of gigavolts per meter, compact electron accelerators had been demonstrated.

²Perhaps even more amazing is that the most powerful computer at the time had only 8 MB of memory [116]!

Increasing electron energy requires increasing the acceleration length or increasing the accelerating field. One means of achieving this is to simply increase laser power, which in turn allows longer interaction lengths by simply using a slower focusing optic. This method is reliant on the progress of laser technology, although there is currently a facility under construction that is expected to exceed 10 GeV in electron energy [77]. To extend the acceleration length further, a staged approach would be needed in which an electron bunch already accelerated from a previous interaction is injected into a subsequent interaction to be accelerated further. An all laser based staged accelerator has been demonstrated [61], so further increases in maximum electron energy are physically possible.

The laser generated electron beam has some inherent characteristics that make it attractive for a variety of applications. An electron bunch accelerated from a single wake is confined to a duration shorter than the period of an electron plasma oscillation, and it has recently been shown that the duration can be shorter than the laser pulse duration [30]. The fs duration of electrons with a mono-energetic energy spectra allow for high resolution electron radiography, and recently there has been some experimental work exploiting this temporal resolution to examine the dynamics of magnetic field generation of a laser plasma interaction [117]. The radial symmetry of the wake provides forces that collimate the electron beam such that the divergence of the produced beam is on the order of mrad. Self trapping is able to confine a relatively large amount of charge; up to a nanoCoulomb per shot is typical [93].

While much progress has been made in increasing the electron maximum energy in a very short amount of time, there is still much to understand about the LWFA mechanism. When the laser is intense enough to expel all of the electrons in the focal volume, the resulting plasma wake is strongly nonlinear. This bubble of space charge can provide high acceleration gradients and produce electron beams with narrow energy spread and good emittance in a regime known as the “bubble regime” of LWFA

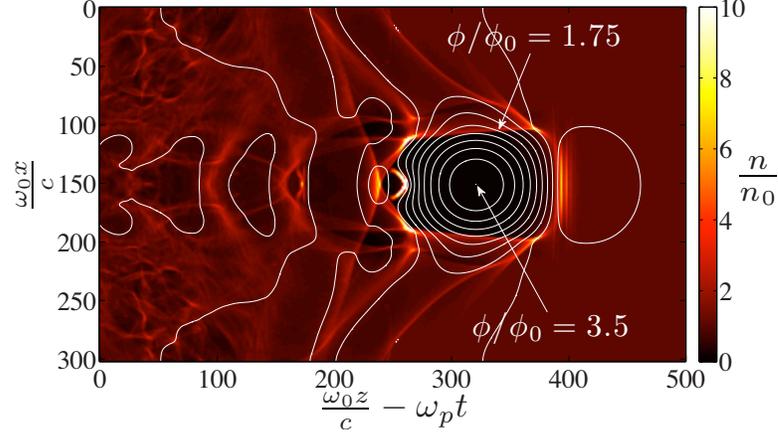


Figure 1.1: A 2 dimensional particle-in-cell simulation of the electron density of a laser wakefield acceleration interaction for a high intensity laser pulse. Due to the symmetry of the electric potential this nonlinear regime is termed the “bubble regime”. Figure courtesy of [126].

(See Fig. 1.1 for an example of a bubble). The mechanism of how electrons enter an accelerating wake, or are injected to the bubble is an area of interest to increase the total charge of the electron beam. The injection process can have significant impacts on electron beam generation, as recent experiments on the effects of ionization occurring within the wake have demonstrated [103, 94].

Thus far the discussion has been on electron acceleration from gas targets, mainly due to the success of LWFA. However, electrons are also accelerated in an interaction with any plasma density, particularly in solid density plasmas in which a variety of acceleration mechanisms are able to accelerate electrons to energies up to tens or hundreds of MeV [52]. Inside a solid density plasma extremely large currents can flow even though regions where the laser does not propagate, causing magnetic field generation to gigagauss strength [24, 123]. However, due to collisions and other effects, the properties of the produced electron beam tend to be Boltzmann in energy spectra and to have a large divergence.

1.1.2 Ion Acceleration

With their substantially higher mass³, ion motion is limited in comparison to the electron acceleration mechanisms previously described. Indeed, in many cases the assumption is made that the ion mass is infinite, so that ion motion is neglected. For even a proton, this would require a laser intensity over 6 orders of magnitude higher than what is needed for electron relativistic motion, at an intensity of $I\lambda_{\mu m}^2 \gtrsim 10^{24} W cm^{-2}$. To place this in context, the highest intensity achieved by a laser system is two orders of magnitude less, and the sharp focusing optic used is impractical for use in experiments [143]. This is not to suggest that the ponderomotive force has no influence, early on it was known that the ponderomotive force from the laser was strong enough to deform the surface, such that oblique absorption effects could take place at normal incidence [72]. In addition, the large space charge that is formed from the ponderomotive force pushing aside the electrons in a low density plasma gives rise to a Coulomb explosion [16].

The Coulomb explosion mechanism hints at how most ion acceleration mechanisms work. Since the ions are effectively immobile for the duration of the interaction, one means of accelerating ions is to set up large space charges by moving the electrons. In this manner, electrons bootstrap the ions to high energies by the strong electric fields from charge separation. With higher densities, higher charge separation can occur, so that higher energies can be achieved but this would require higher intensities as well.

A problem exists with solid density targets, however. Unless great care is taken, a layer of contaminants which is a few tens of angstroms thick exists on practically every surface. This became immediately obvious to early experimentalists who observed energetic protons from targets such as tungsten, and found through Auger measure-

³ m_p is approximately 1836 times m_e .

ments that proton rich hydrocarbons⁴ covered all of their samples [50]. While early experiments observed protons being accelerated up to MeV energies from the front surface of solid targets, it was thought that rapid plasma expansion was the source of the acceleration [7, 42]. A surprising development occurred in pioneering experiments when for thinner, foil targets protons were observed at MeV energies in a direction normal to the *rear* side of the target [86, 24, 120]. A follow up experiment using a wedged target definitively showed that the primary source of protons was from the rear side (See Fig. 1.2.) [52].

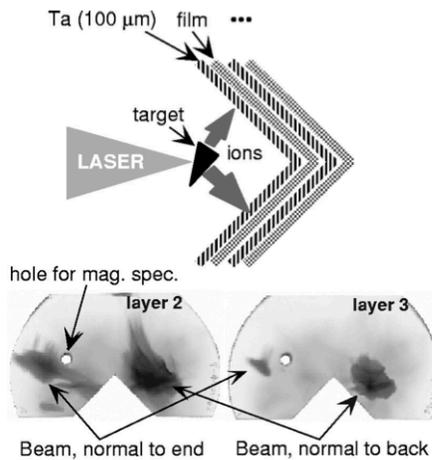


Figure 1.2: A wedged target and the radiochromic film that detected the accelerated protons. There are clearly two beams of protons generated, that come normal from the rear surfaces. Note that there is not a third beam in the laser direction. Data courtesy of [52].

The experiment also for the first time introduced the idea that the acceleration was caused by a sheath field formed by hot electrons that had originated from the interaction site. The mechanism henceforth known as target normal sheath acceleration (TNSA) describes how accelerated electrons that leave the rear of the target set up a strong, quasi-static electric field. [137]. In the initial experiments performed at the Nova Petawatt Laser at Livermore, protons with a maximum energy of 55

⁴The source of these contaminants is commonly water vapor and vacuum oil, so there exists a high number of protons, carbon and oxygen atoms on the surface.

MeV were observed implying accelerating gradients exceeding teravolts per meter. This is more than enough to cause barrier suppression ionization of protons and ions, and accelerating them to MeV energies in only a few tens of microns. The lightest particles would accelerate first, so protons would extract the most energy. In many experiments, the solid density target would be composed of atoms that were heavier than those which made up the contaminant layer, so carbon and oxygen would be the only other ions to be accelerated significantly.

TNSA is arguably the most studied laser ion acceleration mechanism, since experiments can be performed on laser systems with highly varying parameters. Since the ions originate in a well defined plane, for an unperturbed rear surface the accelerated ions all have a very well defined path. Deviations due to collisions will limit the emittance, but measurements have placed the emittance at > 0.004 mm mrad [28]. The flux from a proton beam can be high for a single shot. For a typical proton density of $\sim 10^{23} \text{ cm}^{-3}$ in a 5 nm layer with a transverse width of 100 microns, a total of 5×10^{12} protons can be accelerated ⁵.

However, there are some inherent characteristics of TNSA that make it less than ideal for applications. While the emittance is low, the energy spread is high. Although the accelerating field is quasi-static, it is far from static, and as hot electrons cool and initial ions take away energy from the sheath the field strength decreases with time. Due to this, the ion energy spectra is typically Boltzmann-like. Another major obstacle is the maximum energy. For long pulse lasers, proton energies did not surpass the initially reported Nova results until very recently [59]. For short pulse lasers, although the electron temperatures may be much higher, the maximum proton energies remain below 20 MeV as of this writing. As shall be demonstrated in the following sections, there are many potential applications that depend on higher

⁵Of course, the tangential size of the accelerating field will be dependent on the total energy deposited by the laser and the electron temperature. Kilojoule laser systems with moderate intensities can support sheath fields mm in diameter.

energy, narrow energy spread ion beams.

1.1.3 Laser Technology

CPA lasers have been the main driver for laser based accelerators, enabling a means of achieving high peak intensities without the need of many laser beams and megajoules of energy [53] In the CPA scheme, a femtosecond pulse is temporally stretched by some dispersive element, typically a grating, to several hundreds of picoseconds in duration. This drops the power, and thus the intensity, of the pulse down many orders of magnitude. Ti:sapphire amplifiers are commonly used as a gain medium to achieve many orders of magnitude amplification using multipass or regenerative amplifiers in the near-infrared part of the spectrum. For terawatt or petawatt class lasers, many stages of amplification might be used and the beam diameter has to be increased since even the stretched pulse will eventually exceed the damage threshold of the optics. Finally, the beam is typically sent through a pair of gratings in the Treacy configuration, that provides negative dispersion to recompress the pulse down to femtosecond durations [90]. A diagram of a typical CPA laser is shown in Figure 1.3.

Short pulse CPA systems are now able to deliver terawatts of laser power at repetition rates of kilohertz, making the viability of a laser based accelerator more feasible. This is achieved by using diodes to provide the high energy and high efficiency light to the pump lasers rather than flash lamps, which produce large amounts of excess heat and thus need time to thermally stabilize. A limiting factor for the growth of CPA lasers is the beam size, for as the beam size increases the optics, and in particular the compressor gratings must be larger to accommodate the beam without damaging optics; which will eventually increase costs to prohibitive levels. However, with the lowering costs and greater availability of terawatt and even petawatt lasers a tabletop source may soon become feasible for a wide array of applications.

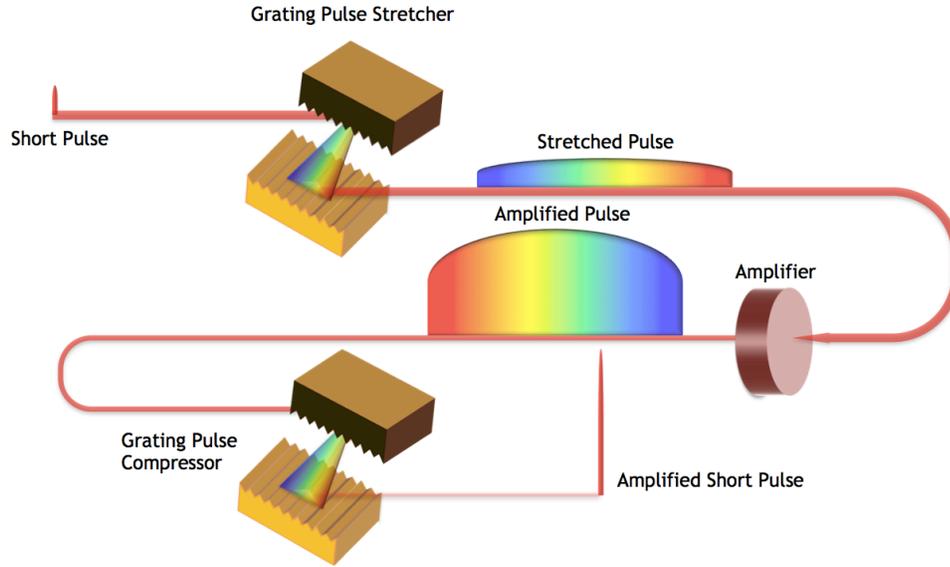


Figure 1.3: Schematic diagram of a Chirped Pulse Amplification laser system.

1.2 Laser Based Light Sources

Accelerating charges give off radiation, and high acceleration fields inherent with short pulse lasers that can accelerate electrons to nearly the speed of light in only a few laser cycles suggest that they may also be a promising source of radiation. In fact, several methods of generating x-ray light exist from such an interaction, and due to the short durations of the interaction x-rays are produced in bursts that can have significant advantages for some applications. The generation of x-rays from a plasma has been known for long pulse lasers since shortly after the discovery of the laser [37]. In fact, next generation photolithography utilizes a laser produced tin plasma as the light source [132]. However, an entirely new level of performance can be achieved with the use of short pulse lasers, utilizing relativistic and nonlinear interactions.

1.2.1 Hard X-ray Sources

1.2.1.1 X-Ray Transition Emission

When an intense laser interacts with a solid density plasma, electrons are heated to high energies through a variety of absorption mechanisms that will be discussed in depth in Chapter II. The electrons can have temperatures in the MeV range, which enable the electrons to “knock out” electrons from atoms and ions in the plasma. The atomic vacancy will quickly be filled by an electron in a higher energy level, giving off transition radiation in the process. If the electron that is removed is an inner shell electron, the resulting radiation from an electron falling in from the next orbital shell is in the x-ray regime, and is known as K_α radiation⁶. Since the photon energy emitted depends solely on the difference in electron levels, characteristic emission lines are generated from a given plasma. The intensity and location of these emission lines give useful information about the constituent atoms in the plasma, as well as the electron temperature, making plasma spectroscopy an ideal method for gaining information about the plasma. For short pulses this light source can be brief, existing for only several picoseconds [146], useful for back-lighting experiments. As we shall see in Chapter VI, the emission lines can give insightful information on plasma conditions.

1.2.1.2 Betatron Radiation

Returning to the LWFA mechanism, it was noted that the radial forces of the wake provided a means of collimation. Any tangential motion would be opposed by a strong restoring force. For a group of injected electrons with transverse momentum, oscillating in the transverse direction will give rise to betatron radiation. The radiation produced by the transverse oscillations is Lorentz transformed to the lab frame, producing radiation analogously to an undulator insertion device used on third gen-

⁶The nomenclature is due to historical reasons, in plasma spectroscopy nomenclature the actual emission is known as $k_{\alpha 1}$. K refers to the vacancy location, the alpha represents where the transitional electron originated, and the numeral is to specify the spin state

eration synchrotron light sources. Because the oscillations tend to be large compared to the forward motion, the spectra produced is synchrotron-like. Recent experiments have demonstrated a high flux of x-rays in the keV energy range [67]. The acceleration time is on the order of the pulse duration, so that the inherent duration of the x-ray beam is on the order of femtoseconds making it a very bright source.

1.2.2 Soft X-Ray Sources

1.2.2.1 Gas Harmonics

High harmonic generation (HHG) is an example of a very nonlinear process, in which coherent, few-fs, x-ray pulses are generated when an intense femtosecond laser is focused into a gaseous media. A sufficiently intense laser pulse can deform the Coulombic potential that normally binds an electron to an atom to such an extent that the electron can tunnel through the potential barrier. When the laser field reverses direction, the electron is rapidly accelerated back to its parent ion, and can recombine, liberating any excess kinetic energy as a high harmonic photon. If harmonics from many recolliding electrons are emitted in phase, then the output extreme ultraviolet (EUV) ⁷ beams are bright, spatially coherent, covering a large bandwidth, and with pulse durations in the femtosecond and even attosecond regimes [124]. Disadvantages of harmonics generated in this fashion are that great care must be made to ensure that the harmonics are phase matched, or else the harmonics will not produce an attosecond pulse train. Additionally, increasing the intensity too far beyond the ionization threshold prevents the electrons from recombining. This prohibits further increases in the harmonic production and limits conversion efficiency.

⁷Different communities refer to the wavelength range of 50 eV to 1 keV by various nomenclature, such as soft x-rays, and extreme ultraviolet. In this thesis the two phrases will be used interchangeably.

1.2.2.2 Surface Harmonics

After early results of gas harmonic generation, it was noted that harmonic generation should be achievable with an intense laser incident on a solid density plasma [135]. At solid densities, an intense laser immediately ionizes the surface and reflects off of it. At very high intensities electron motion is no longer sinusoidal, for as the electrons move closer to the speed of light their effective mass increases. The accelerated charges are rapidly decelerated in phase as the linearly polarized electric field changes signs. The rapid deceleration causes the emittance of radiation, and for an intense enough laser this can cause emission of soft x-rays. Early experiments with CO₂ lasers discovered a harmonic spectrum being reflected from a variety of targets that extended into the optical [18]. After early results of gas harmonic generation into the EUV, it was noted that harmonic generation should be achievable with a short pulse laser incident onto a solid density plasma [135], and soon after were demonstrated [69]. With higher intensities becoming available, even higher harmonic generation is able to be observed, with an experiment on the Vulcan Petawatt laser producing hundreds of harmonics with hundreds of keV in photon energy[35].

1.3 Applications of Laser Based Sources

1.3.1 Ion Applications

The generation of energetic protons and ions from a compact source is an exciting prospect for many applications with potential decreases in size and cost. In addition, there exist several advantages to a laser based accelerator over conventional means. A small subset of some of the applications will be highlighted here.

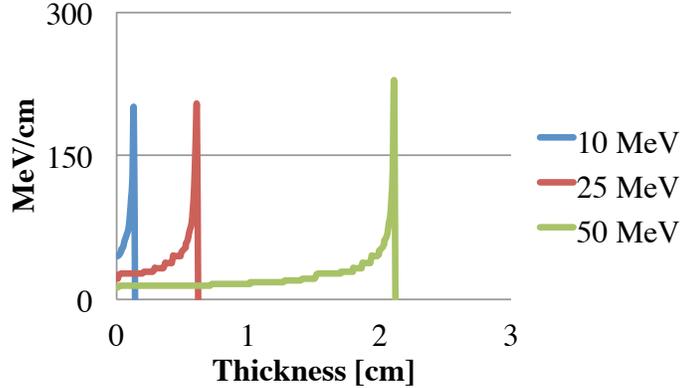


Figure 1.4: Energy loss of protons in liquid water. The sharp region where most of the energy is deposited is known as the Bragg peak.

1.3.1.1 Hadron Therapy

A heavy particle deposits its energy in a very localized region determined by its energy, which will be discussed further in chapter III. This region is known as the Bragg peak, as shown in Fig. 1.4. This is in contrast to light, which follows the Beer-Lambert law for absorption:

$$I = I_0 e^{-\alpha x} \quad (1.1)$$

where α is the absorption coefficient of the material. This difference in energy deposition is exploited in a form of therapy for cancer known as hadron therapy. In conventional radiation therapy, a specified dose of radiation is to be deposited to a localized region of the body via x-rays. Unfortunately, even with focusing a sizable dose of radiation is deposited to regions of healthy tissue surrounding the site of therapy. Since only ionizing radiation is necessary for radiation therapy, an alternative, long desired idea is to use light ions such as proton or carbon beams to dramatically reduce the damage to healthy tissue [140]. However, the use of RF accelerators has proven to be an expensive prospect, as there are only 10 proton therapy facilities in the United States [1].

The use of a laser based ion source for proton therapy was discussed shortly after the discovery of high energy protons from the first experiments [15]. A laser and target may be realigned on the fly using piezo-actuators eliminating the need for large and expensive gantries, a very expensive component of a proton therapy center. Laser based acceleration easily enables acceleration of other light ions, whereas conventional accelerators are designed for a single particle species. The use of a heavier ion such as carbon may be beneficial since the transverse scattering is reduced and the region that is damaged is increased from microns to mm. The reduced scattering allows for more energy to be deposited in the Bragg peak, and the extended damage range is more suited for complete irradiation of the tumor; however the number of clinical trials with carbon ions have been small in comparison to protons [3].

1.3.2 Nuclear Reactions

Since the extremely localized region of dose delivered via ion therapy is akin to a scalpel, the deposition of radiation can be made very precise. This also necessitates more accurate information on beam positioning. The human body is a dynamic system, and depending on the location of the tumor the tissue may change in position on timescales longer than what is needed to deliver the dose. Rather than irradiate healthy tissue, imaging is used to track the tumor in situ with a technique known as positron emission tomography. A positron emitting tracer that preferentially attaches to tumor cells can be used to flag the region of interest. The positrons will recombine to form a pair of 511 keV photons which can be reconstructed to form a 3D image. Additionally, as the ions stop in the Bragg peak, a small number of radioactive nuclei are generated, such as carbon isotopes 10 and 11 which are positron emitters. Thus, both the tumor and the interaction can be monitored in situ as the dosage is administrated.

The primary difficulty with the use of radiotracers is that the commonly used ra-

radioisotopes have half-lives on the order of tens of minutes, so they must be constantly produced near the facility to be useful. However, an intense laser interaction is also capable of producing radioisotopes through photoactivation. Electrons accelerated in an intense interaction can be sent into a solid material where bremsstrahlung occurs. Due to the giant dipole resonance, the cross-section for (γ, n) reactions reaches a maxima for photon energies around 10 MeV. Photonuclear interactions of copper have been demonstrated using a laser source by accelerating electrons from a solid foil [87] or from a beam of electrons generated by a wakefield accelerator [110] and sending the beam into a high atomic number material such as tantalum. The production of carbon-11 from boron-10 has also been demonstrated by bombardment with a beam of laser produced deuterons [101].

A particular nuclear interaction is the generation of a high brightness positron source. A high intensity laser solid interaction produces a Boltzmann temperature of electrons that scatter throughout the target. If the target is a high atomic number material such as lead or gold, the electrons undergo bremsstrahlung within the target itself producing a substantial number of ~ 1 MeV photons⁸. For a thick target, the photons can scatter off of atomic nucleus and produce an electron-positron pair⁹. If the positrons scatter out of the target, they may suddenly be in an accelerating field, the very same sheath field that accelerates ions in TNSA. The positrons can then be accelerated to many MeV with a narrow energy spread, as the positrons are produced and accelerated over timescales shorter than the temporal evolution of the sheath [21].

Nuclear reactions can also be exploited for a laser based source of high brightness, directed neutrons. With the proliferation of nuclear material in the world, it becomes a matter of national security to secure trade routes from illicit transfer of such material. A single cargo ship may contain thousands of cargo containers, and the

⁸1,022 keV being the minimum energy required for pair production; i.e., from twice the rest mass of the electron/positron, $m_e c^2 \approx 511$ keV.

⁹The nuclei is a necessary part of the interaction for conservation of momentum reasons, necessitating a thick, high atomic number material.

manpower required to examine each one is prohibitively expensive. A technique to “scan” cargo ships quickly is then the motivation of active interrogation. By actively bombarding a vessel with high energy neutrons, fission may be induced which in turn will produce a characteristic gamma ray spectra that may be observed. The need for a compact and deployable neutron source may be filled by short pulse laser interactions. Several nuclear interactions, such as (p,Li), (d,d), or (d,Li) have a maxima in the cross section for an incident energy of 1 – 10 MeV, achievable in experiments today. For a laser interacting on a target consisting of a deuterated plastic, deuterons directly accelerated by the laser can interact with other deuterons within the target, producing a source of neutrons at 2.45 MeV, which is the Q-value of that particular interaction. Much interest lies in the (d,Li) reaction, with its Q value of 14.3 MeV for production of high energy neutrons.

Short pulse lasers can accelerate particles to much higher energies by using the TNSA mechanism, and perhaps to even higher energies with other mechanisms. To exploit this, a modified experimental geometry is utilized in which the ion production and the nuclear interactions occur in separate targets. This so-called “pitcher-catcher” geometry enables high energy proton and deuterons to interact with an optimal target. The benefit of the higher energies can be observed by considering the frame of reference for the interaction. Once this frame is Lorentz transformed to the lab frame, the kinetic energy of the ion beams causes the produced neutrons to be forward directed and possess a higher energy [29]. Results using longer pulse, higher energy lasers have been published [57]. Production of neutrons with energies above 10 MeV have been achieved in experiments at HERCULES during the course of this thesis, as seen in Fig. 1.5.

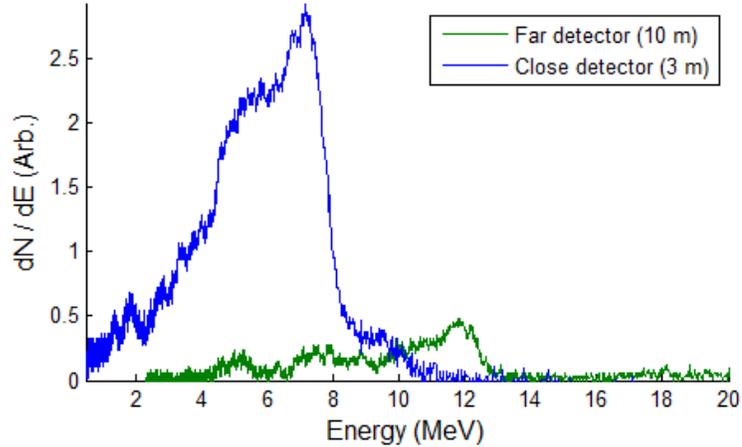


Figure 1.5: Neutron time-of-flight data from a (d,Li) interaction using the HER-CULES laser.

1.3.2.1 Fast Ignition

One of mankind's greatest dilemmas has been how to secure energy for a long term future. There has been an escalating advancement of technology and science, due in part to the abundant reserves of fossil fuels. However the non-renewable nature of these energy sources necessitates a more permanent solution. The amount of energy stored in a chemical bond pales in comparison to the amount of energy in a nuclear reaction¹⁰. Fission reactions are the basis of nuclear power plants, and there are reactor designs in which enough fissile material is available to endure the lifetime of the Earth [27]. However, a number of significant issues prevent nuclear power from being a panacea to the world's energy problems. Fission reactors produce radioactive waste which must be securely disposed while the radioactivity decays, a process that may take thousands of years. Reactors can also be used as a tool for generating nuclear weapons material. The threat of contamination from a reactor that is damaged by accident, natural disaster, or terrorism also has slowed public acceptance of nuclear fission as a power source.

The alternative form of nuclear power is fusion. The reaction of deuterium and

¹⁰Governed by $E = mc^2$

tritium generates a 3.5 MeV alpha particle and a 14.1 MeV neutron, considerably more energy than released than the ~ 5 eV from the oxidation of two protons in a chemical reaction¹¹. The difficulty of generating a sustained fusion reaction stems from the need to place the two nuclei close enough to overcome Coulombic repulsion. For the deuterium-tritium reaction, this requires a temperature of tens of keV, where the fusion cross section peaks and efficiency is maximized. However, this plasma must be confined long enough to achieve the reaction rates for net energy production to occur. One scheme involves magnetic confinement, where lower density fuel is placed in a strong magnetic trap at high temperatures until energy gain is achieved. The most ambitious project to attempt this to date is the International Thermonuclear Experimental Reactor, which is planned to demonstrate a fusion gain of 10 [119].

The other scheme of achieving fusion gain in a laboratory is with inertial confinement fusion. Rather than existing for long timescales and lower plasma densities as with the magnetic schemes, the fuel is compressed to thousands of times solid density to both heat the fuel and increase the number of reactions for only tens of picoseconds to achieve significant gain. At high enough densities, the reactions may become self-sufficient, and then gain can be achieved. Due to the significant compression of matter that can be achieved with even a relatively modest intensity laser [102], lasers are most often used in this scheme. Although this work suggested that fusion gain may be achievable relatively easily, it was soon realized that hydrodynamic instabilities such as Rayleigh-Taylor can prevent the efficient compression of a core [80]. The culmination of decades of research in this field is realized with the National Ignition Campaign [53, 36], currently in progress at the National Ignition Facility in Lawrence Livermore National Laboratories (Fig. 1.6).

The ability to generate more energy than is input, or gain, is then dependent on the driving power of the laser and the ability to compress the fuel. In the Fast

¹¹But considerably less than the ~ 200 MeV released in a typical fission reaction.



Figure 1.6: A view of one of the two laser bays at the National Ignition Facility. Credit: Lawrence Livermore National Laboratory.

Ignition scheme of inertial confinement fusion, the heating of the fuel occurs with a beam of particles generated by a short laser plasma interaction rather than through compression itself [122, 115, 17]. The benefit of separating the heating and compression is because the fuel can be compressed much more at a lower temperature than at a higher temperature, and then the particle beam can start a series of reactions that will begin sustained fusion. In other words, the cooler compressed plasma will have a lower density and pressure, decreasing tolerances required due to instabilities and other temperature dependent effects. A much higher gain may be achieved with fast ignition in comparison to “hot spot” ignition for a given laser, or conversely a desired gain may be achieved with a lower power laser.

The fast ignition concept is still in early stages of research, with many problems to address. For instance, the delivery of the igniter beam to the core requires that great care must be taken to ensure that the symmetry of the fuel is not perturbed to drive further instabilities. The choice of the igniter particle is an area of active study, with electrons perhaps being the most studied [68], although protons have been

considered as well [106]. The interactions of high power short pulse lasers is a field not as mature as long pulse interactions, and the work presented in this thesis along with numerous other studies occurring today provide important physical understanding of such interactions.

1.4 Comparison with Existing Facilities

Currently, laser based sources are lacking in several key areas when compared to conventional technology. Conventional RF accelerator technology is at a very mature state, for example a 100 MeV proton accelerator can be purchased for about the cost of a petawatt class laser [81]. For use in applications, considerable advancements in repetition rate, charge per shot, maximum energy, and spectral control need to be demonstrated; however, the field is still very much in its infancy and much of the physics is not well understood. The work performed in this thesis is an attempt to address some of these issues.

An application that shows great promise is for the generation of x-rays. In terms of brightness¹², the x-ray source from the laser wakefield experiments on HERCULES is comparable to third generation facilities and already shows properties of spatial coherence [67, 66]. The x-rays produced also have a very short temporal duration compared to third generation facilities. Fourth generation x-ray facilities, or free electron lasers, have demonstrated brightnesses nearly ten orders of magnitude brighter than third generation facilities, also with femtosecond pulse durations [141]. The cost of such a facility is extreme, costing several billion dollars and often requiring international participation, such that the total number of facilities will likely remain small. There is also a great interest in the generation of isolated attosecond pulses, where no conventional source currently exists.

¹²Brightness in the synchrotron community is typically given as photons per second per mm²mrاد² per 0.1% bandwidth.

1.5 Thesis Organization

This thesis mainly describes the experimental work performed in the solid target experimental area at the HERCULES laser facility. It will be demonstrated that only through very careful control over the laser contrast can such high intensities be used, and that the availability of short pulses enables significant advantages in ion acceleration and radiation generation. After a brief history and overview of the pertinent physics necessary for high intensity laser plasma interactions with solid density plasmas in chapter II, a description of the capabilities developed for the experiments used in this thesis will be described in chapter III, including characterization of plasma mirrors for use as laser contrast improvement. Then, a series of experiments on ion acceleration techniques will be presented. Chapter IV will examine the exploitation of HERCULES' high contrast capabilities to shape ion energy spectra, while chapter V will present investigations into the radiation pressure acceleration mechanism. Radiation generation by means of HHG will be presented in chapter VI. An outlook on the future of laser based accelerators and light sources will serve to conclude this thesis.

CHAPTER II

Theoretical Background

The following chapter provides a development of the pertinent theory necessary for the understanding of the described physics. It assumes a rudimentary knowledge of electrodynamics and plasma physics, good reference books for each can be found in the following references [20, 58].

2.1 Laser Physics

2.1.1 Dispersion

The HERCULES laser system produces a peak power of 300 TW, a number nearly 700 times the United States power consumption; of course, this is only achieved for a mere 30 femtoseconds so the amount of energy in a single shot is only one hundredth of that found in a camera flash [134]. A laser pulse is a well-behaved square integrable function, and so it follows a time-bandwidth product such that

$$\tau_0 \cdot \Delta\omega_0 = 2\pi c_B. \tag{2.1}$$

where we have that τ_0 is the diffraction limited pulse duration, $\Delta\omega_0$ is the laser bandwidth taken around the laser frequency ω_0 , and c_B is a constant on the order of

unity that depends on the pulse shape¹. Then for a femtosecond pulse, a bandwidth on the order of 10^{15} Hz is required, so short pulses are more spectrally broad than longer pulses.

Note that the equation depends on the *diffraction limited* pulse duration. This is a nontrivial statement, as the large bandwidth of short pulse lasers has important implications. When a pulse travels through a material that is not vacuum, the propagation of the pulse is defined by $n(\omega)$, the material's index of refraction. Consider a diffraction limited Gaussian pulse with duration described by $\vec{E}(z, t) = \exp(-\alpha t^2 + i\omega_0 t)$. Using the Helmholtz equation for a linear dielectric

$$\left[\frac{\partial^2}{\partial z^2} + \frac{n^2 \omega^2}{c^2} \right] \vec{E}(z, \omega) = 0 \quad (2.2)$$

we see the standard solution of $\vec{E}(z, \omega) = E_0 \exp(-i \frac{n(\omega)\omega}{c} z)$, with the assumption that $n(\omega)$ is a slowly varying function. There is a complicated dependence on ω . Since this is a linear function, no new frequency components are generated, however, there is a dramatic change in the temporal structure of the pulse. Since the index of refraction is slowly varying across the frequency, we may make a Taylor expansion of n around the central laser frequency ω_0

$$n(\omega) \approx n(\omega_0) + \frac{\partial n}{\partial \omega} \Big|_{\omega_0} (\omega - \omega_0) + \frac{1}{2} \frac{\partial^2 n}{\partial \omega^2} \Big|_{\omega_0} (\omega - \omega_0)^2 \dots \quad (2.3)$$

This can be substituted into the Helmholtz solution and Fourier transformed back into the time domain to see the effect on the laser pulse. These effects are collectively known as dispersion. The impact of the various terms of the expansion can be best

¹For Gaussian pulses, $c_B \approx 0.44$.

understood with several definitions,

$$v_\phi = \frac{c}{n} \quad (2.4)$$

$$v_g = \frac{1}{\frac{\omega}{c} \frac{dn}{d\omega} + \frac{n}{c}} \quad (2.5)$$

$$GVD = \frac{dv_g}{d\omega} = \frac{-v_g^2}{\frac{\omega}{c} \frac{d^2n}{d\omega^2} + \frac{2}{c} \frac{dn}{d\omega}} \quad (2.6)$$

where v_ϕ is the phase velocity, v_g is the group velocity, and the GVD is the group velocity dispersion. With these definitions, the equation for a diffraction limited Gaussian laser pulse propagating through a linear media has a more apparent meaning,

$$\vec{E}(z, t) = E_0 \exp\left(i\omega_0 \left(t - \frac{z}{v_\phi(\omega_0)}\right)\right) \cdot \exp\left(\left(\frac{\alpha}{1 - 2i\alpha z \frac{GVD}{v_g^2}}\right) \left(-\frac{z}{v_g(\omega_0)}\right)^2\right). \quad (2.7)$$

Now the effects of dispersion on a short pulse can be seen clearly. The first term describes the carrier wave, while the second exponential describes the slowly varying envelope. Compared to vacuum, we see that the phase of the pulse is delayed by a time $\frac{z}{v_\phi(\omega_0)}$, in what is termed phase delay. The entire pulse is delayed by a time $\frac{z}{v_g(\omega_0)}$, the group delay. The most important change is that the envelope of the pulse has been lengthened by an amount related to the GVD. Thus a diffraction limited pulse traveling through any dispersive media will broaden temporally.

Qualitatively, the broadening due to GVD can be understood by a simple example. A diffraction limited pulse is the superposition of many wavelengths that are in perfect phase with each other. At this point all the phase velocities are the same, and the rate of phase advance, or instantaneous frequency, of the pulse given by $\omega(t) = \frac{d\phi}{dt}$ is identically zero. As it propagates through a material, the frequency components

of the laser pulse dephase with respect to each other because of the GVD. Thus one frequency may outrun another, making a nonzero instantaneous frequency. When the change in frequency is linear, it is termed a linear chirp. Positive chirp is the most common with most dielectric material in the near infrared (NIR), where the red components are at the front of the pulse and the blue are at the rear.

In the previous analysis, we neglected the effects of the higher order terms of n . These parameters are collectively known as higher order dispersion and play an important role in short pulses, having effects similar to GVD. The presence of GVD requires that short pulses propagate in vacuum, and do not enter dispersive elements such as lenses or filters. Even air may be problematic, as an NIR 30 fs pulse will double in duration after traveling through 25 meters of air. Thus, many experiments are performed in vacuum to mitigate dispersive effects. It should also be mentioned that pulse broadening can occur without the pulse traveling through any material at all. Pulse front tilt can occur for a pulse that reflects from a surface that introduces a path length delay across the pulse front, as is the case with a spherical surface.

2.1.2 Nonlinear Effects

While dispersion is a linear effect, there are nonlinear effects that play a significant role in short pulse laser interactions. High peak power lasers often are manipulated with optics close to the damage threshold, meaning that high intensities are often present. Again, the index of refraction comes into play. Linear optics depend on the response of the material being proportional to the electric field, but for very intense fields the laser field can be of the order of the interatomic electric fields, and this assumption is not necessarily valid. A simplified description is found by using another Taylor expansion, this time expanded around E . The nonlinear terms are dependent on the electric field squared, or the intensity I_0

$$n \approx n_0 + n_2 I_0 = n + \frac{\chi_{eff}^3}{4n_0^2 \epsilon_0 c} I \quad (2.8)$$

where ϵ_0 is the permittivity of free space. The nonlinear index of refraction, n_2 , is of the order of 10^{-18} to $10^{-16} \frac{\text{cm}^2}{\text{W}}$, so very intense pulses are needed for these effects to appear.

A wide variety of nonlinear effects exist, and will not be described here. One worth mentioning for short pulses in particular is Self Phase Modulation (SPM). Here, the propagation of light through a nonlinear material *can* result in the formation of new frequencies, providing a means of increasing the bandwidth of a laser pulse. Equation 2.7 described a pulse that had been altered from the index of refraction being variable with frequency. If instead dispersion is neglected and equation 2.7 is substituted into equation 2.8, the result is

$$\vec{E}(z, t) = E_0 \exp(i[\omega_0 t - \frac{\omega_0}{c}(n_0 - n_2 I(t))z]) \cdot \exp(\alpha t^2). \quad (2.9)$$

The change in the instantaneous frequency, or $\frac{d\omega}{dt}$ can be written as $\delta\omega = -\frac{n_2 \omega_0}{c} z \frac{dI(t)}{dt}$. The immediate consequence of the nonlinearity is that the rising edge of the pulse is blue shifted and the falling edge of the pulse is red shifted, resulting in a negative chirp of the pulse. The nonlinearity also caused new frequency components to be generated, dependent on the amount of nonlinear material that is present. This process describes SPM, and is present in not only dielectric material but in plasmas as well [133].

The previous derivation altered only the carrier profile. The envelope function, and thus the pulse duration remain the same. The SPM process adds bandwidth to the pulse without increasing the pulse duration, which is achievable since the pulse becomes negatively chirped. However, when dispersion is included, the positive GVD

of the material counteracts this negative chirp, so the chirp is decreased and the pulse can be compressed. If the parameters are controlled effectively, SPM and dispersion can be balanced and a diffraction limited pulse can be produced [22].

The presence of SPM can be problematic as well, particularly in the case when the pulse has a Gaussian transverse profile. In this case, the index is spatially varying across the wavefront and can act as a lens. This is a form of self-focusing, and can cause a pulse to converge in a material. As the beam is focused, the effect becomes stronger until it is intense enough to break down the material. This can happen even for flat top beam profiles with hot spots in the beam.

To ensure that an optical system is not plagued by the problems that can happen from undesired nonlinearity, a simple parameter is used to describe the system. The B-integral is a sum of all of the nonlinearity a pulse acquires as it propagates through a system, given by

$$B = \frac{2\pi}{\lambda_0} \int_0^T n_2 I(z) dz. \quad (2.10)$$

In general, when the B-integral of a system is less than $\sim \pi$, one can expect that the wavefront aberrations introduced by the nonlinearities will be sufficiently low.

2.1.3 Laser Contrast

In short pulse lasers, a critical parameter is the laser contrast. State of the art short pulse lasers such as the HERCULES facility have a quoted contrast of 10^{-11} [23], however it is not immediately clear what that number means. A review of the physical definition of the laser contrast will be presented, and then the role it plays will be critically examined.

As we shall see in the upcoming sections, the presence of plasma can have a drastic effect on the propagation of a laser pulse. The interaction of the laser pulse with a plasma is the very subject of this thesis, however it is important to have knowledge

of the density profile of the plasma to properly interpret results. Unfortunately, this is very difficult in practice. A third order autocorrelation of the HERCULES laser pulse is presented in Fig 2.1. The gain lifetime in Ti:Sapphire is $3.2 \mu\text{s}$, considerably longer than the duration of the stretched NIR pulse for CPA lasers. Prior to the pulse arriving, spontaneous emission can occur along the beam path, introducing light to the optical system far earlier than desired. This is known as amplified spontaneous emission, or ASE. Typically, an electro-optical switch such as a Pockels cell can reduce this to a window of a few ns.

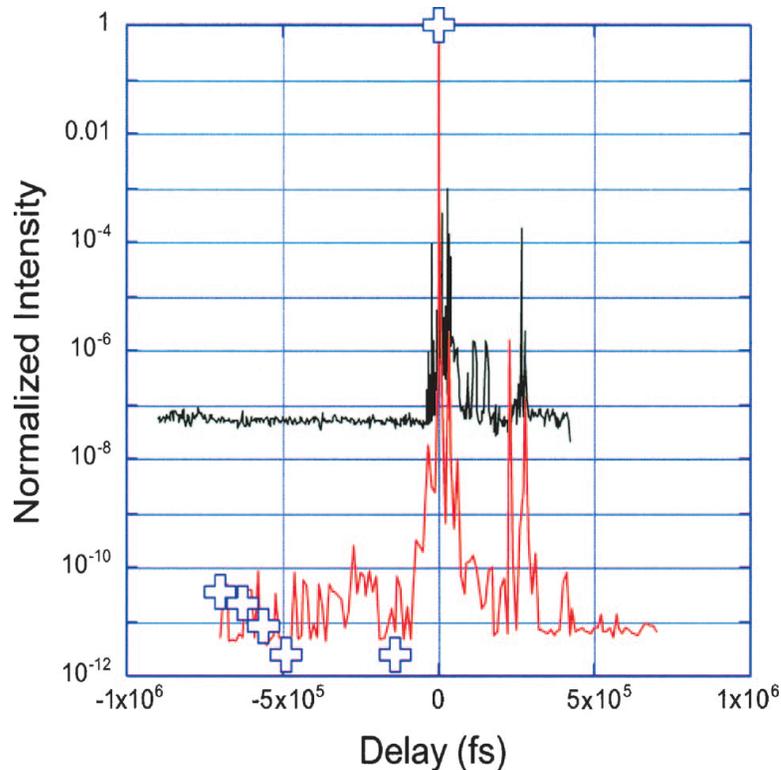


Figure 2.1: 3rd order autocorrelation of the HERCULES laser pulse without cleaning (black) and with cleaning (red). The measurements are taken at low amplification, with several data points at full power given by the square crosses.

The ratio of the prepulse pedestal to the main pulse peak is known as the laser contrast. It is common for the contrast to be described as the ratio of intensity rather than energy, since the intensity is the important parameter for many applications.

ASE can significantly heat a solid density target and cause hydrodynamic expansion. However, it should not be assumed that this is the only parameter that matters for laser contrast. Any plasma formation on solid targets due to prepulse can alter the density profile of a solid target. As seen in Fig. 2.1, there is structure on the picosecond level that lies outside the main pulse. The presence of a picosecond prepulse can be due to a number of different sources, such as incomplete compression due to imperfections in the grating, nonlinear effects, and higher order dispersion that cannot be corrected. The structure of the picosecond prepulse is not as stable as the ASE, and can be present in short pulse prepulses as well as a rising ramp. A slowly rising picosecond ramp can cause hydrodynamic expansion as well. 1D hydrodynamic simulations of the prepulse interaction with a variety of targets to estimate preplasma levels are shown in Fig. 2.2. The temporal profile used for the simulations was a logarithmic fit of the autocorrellator trace given in Fig. 2.1.

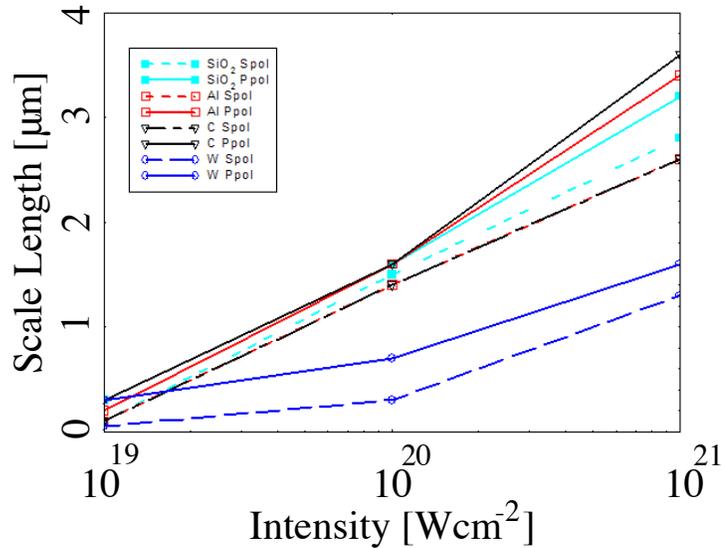


Figure 2.2: 1D Hydrodynamic simulations of intensity v. preplasma scale length of the main pulse for a variety of targets at the time that the main pulse arrives.

The effects of the damage threshold of the target and the fine structure of the

picosecond prepulse both have a strong influence on preplasma formation, which is not readily apparent from the often quoted laser contrast. Short pulse prepulses may expand the plasma through other mechanisms such as TNSA, further complicating the estimation of prepulse. It is thus apparent that even the term “high contrast” lacks quantitative meaning if it is given by a single number, as the entire temporal history of the laser pulse is important. However, the laser contrast is a good first order estimate as to whether a certain experiment may be performed at a certain intensity.

2.2 Single Electron Dynamics

To properly understand the complicated dynamics of an intense laser plasma interaction, a solid foundation of understanding can be attained by considering what happens to a single electron. While the single electron model may provide powerful insight into the dynamics of a laser plasma interaction, it is critical to remember the assumptions taken here. For instance, the wavefunction of an electron is modified in a dense plasma, which may shift energy states².

2.2.1 Ionization

In order to have a plasma, the bound electron must become unbound. This can be achieved in a variety of ways, most of which depend on the laser to achieve plasma formation. The simplest manner of ionization is photoionization [39]. For metals this occurs for any energy gain greater than ~ 5 eV. For NIR and optical lasers, the photon energy is not enough to cause ionization and thus does not occur in the interactions of interest in this thesis.

Ionization can occur for photon energies below the electron binding energy, in

²A matter complicated if there is an electric field present as well, which will lift the degeneracies in an atom.

the event that multiple photons arrive at the same time ³. This event requires high intensities so that there can be enough photons at the atom simultaneously to cause ionization. The rate of ionization for n photons for a perturbative process is given by

$$\Gamma_n = \sigma_n I_0^n \quad (2.11)$$

where the cross section for the interaction is given by σ . The higher the value of n , the smaller the cross section, and thus the higher the intensity needed. This qualitatively makes sense, requiring more photons incident at the same atom will be harder to achieve, and to maintain a high rate a higher photon flux is needed, thus the higher intensity.

At a high enough intensity, there is no longer a need for multiphoton ionization as another mechanism is available. At some point the laser electric field becomes comparable to the interatomic Coulomb field. When this occurs, the electric field alters the potential well of the electron. When this occurs, the electric potential becomes highly asymmetric and the electron is able to tunnel out of the potential well. The hydrogen atom has a Coulombic electric field of 5 GV per meter. If we consider what laser intensity is required to generate a similar field, we see with intensity defined as the time average of the Poynting vector,

$$I_0 = \langle S \rangle = \frac{\epsilon_0 c}{2} E^2 \quad (2.12)$$

and thus an intensity of $\approx 3.5 \times 10^{16} \text{Wcm}^{-2}$. This process is called tunneling ionization. In tunneling ionization, there is a nonzero probability that the electron will tunnel through the partially suppressed potential well (See Fig. 2.3).

The point at which the intensity is high enough such that tunneling ionization

³Note that this is very qualitative description. Since we are talking about photons, the physics is inherently in the quantum realm, and there is no exact meaning of “arriving” since time is not an observable and there may not be an available energy state to transition to. The actual description involves using virtual states and solving Fermi’s golden rule, as described in [10].

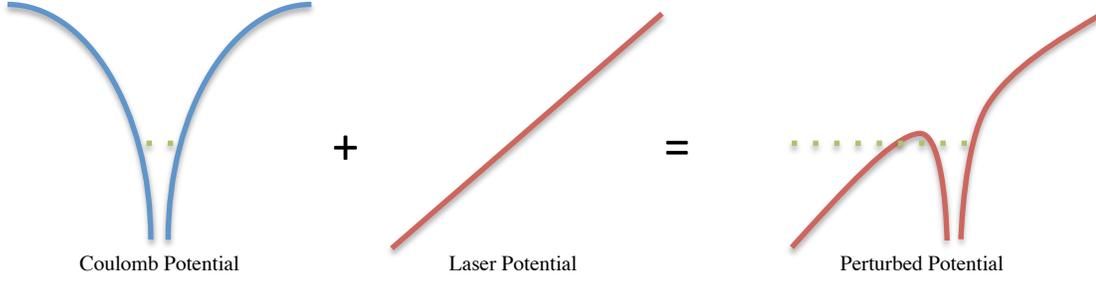


Figure 2.3: Diagram of tunneling ionization. The superposition of the standard Coulomb potential (a) and the intense laser potential (b) produce a situation where a narrow barrier traps the electron (c). When the laser potential is sufficiently large the electron can freely escape in barrier suppression ionization.

becomes important is known as the Keldysh parameter [63], and is given by

$$\gamma = \omega \frac{\sqrt{2m_e\Phi}}{e_c E_0} \quad (2.13)$$

where Φ is the ionization energy and E_0 is the laser field. When the Keldysh parameter much greater than unity means that tunneling ionization is dominant rather than multiphoton. Eventually, such a strong laser field is applied such that the entire Coulomb barrier is below the energy of the electron state, and the electron is no longer bound. This barrier suppression ionization occurs at very particular intensities, when the electric field induced is equal to the ionization level of the electronic state. This intensity is given by

$$I_{appearance} = \frac{c\Phi}{128\pi Z^2 e_c^6} \quad (2.14)$$

and is known as the Appearance Intensity. This intensity is where ionization occurs without any probability, i.e., the tunneling rate turns to unity. The appearance intensities for several common elements in this thesis is shown in Fig. 2.4. The presence of a particular charge state can indicate that a certain level of intensity is

reached. Of course, an atom may also be ionized simply by being in the presence of a strong electric field that can suppress the barrier even without the laser.

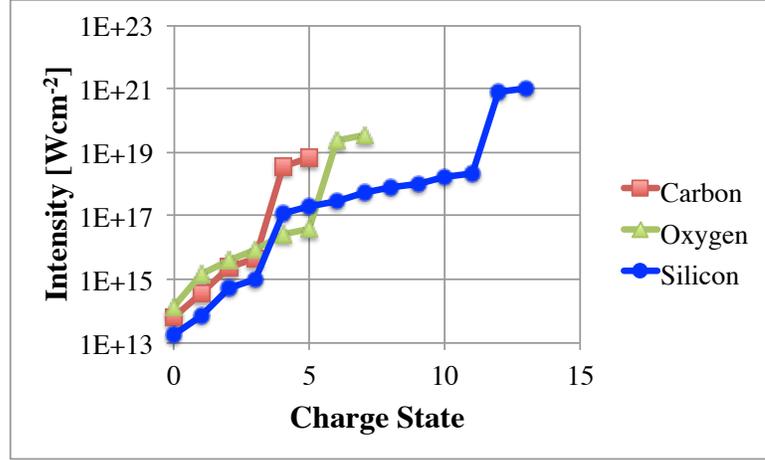


Figure 2.4: Appearance intensities for various elements. Note that the presence of Si^{13+} indicates an intensity greater than 10^{21}Wcm^{-2}

Other forms of ionization exist as well, such as collisional ionization, which allows for ionization outside of a laser focus for lower laser intensity. In collisional ionization, hot electrons inelastically collide with an atom. If the energy absorbed by the collision is higher than the ionization energy, an electron may be ionized. One fast electron can spawn many daughter electrons, which in turn increases plasma density so that there are more electrons in the laser field in a process known as avalanche ionization. A high temperature plasma can also cause ionization. To characterize the ionization in such a complicated situation is difficult, and numerical modeling is needed. If the plasma is in a local thermodynamic equilibrium then a good approximation of the ionization may be made using the Saha equation. The Saha equation related the number of ions in state N_j to those in state N_k by

$$\frac{N_j}{N_k} n_e = \frac{g_j}{4g_k a_{Bohr}^3} \left(\frac{k_B T_e}{\pi \Phi} \right)^{\frac{3}{2}} \exp\left(\frac{-E_{jk}}{k_B T_e} \right) \quad (2.15)$$

where a_{Bohr} is the atomic Bohr radius, E_{jk} is the difference in energy between the

two states, and g is the statistical weights of the states.

2.2.2 Relativistic Motion

A free electron in an intense laser field has some interesting dynamics, although first it is important to describe precisely an intense laser field. A charged particle experiences a force from an electric field, and if the particle is moving from a magnetic field as well. The equations of motion can be derived from

$$F = \frac{d\vec{p}}{dt} = q[\vec{E} + \vec{v} \times \vec{B}] \quad (2.16)$$

which is known as the Lorentz Force equation. In the relativistic version, the momentum now refers to the relativistic momentum $p = \gamma m_e \vec{v}$. In the context of a laser interacting with an electron, it is often a good assumption to assume a plane wave solution of wave equation in vacuum for the electric and magnetic fields, which is much like the interaction at a laser focus. For a linear polarized beam, they are

$$\vec{E}(\vec{x}, t) = E_0 \exp(i[k_0 x - \omega_0 t]) \hat{x} \quad (2.17)$$

$$\vec{B}(\vec{x}, t) = B_0 \exp(i[k_0 x - \omega_0 t]) \hat{y} \quad (2.18)$$

for a wave propagating in the \hat{z} direction and with a wave number $k_0 = \frac{\omega_0}{c}$. Since the amplitude is what is commonly measured, it is often useful to consider $Re\{E\}$ where the exponential becomes a cosine due to Euler's equation. The convention that will be used throughout this thesis to define linear polarization on an oblique surface will be S to signify that the electric field component is perpendicular to the surface⁴, and P for when it is parallel⁵.

⁴From *senkrecht*, the German word for perpendicular.

⁵From *parallel*, the German word for parallel.

An electron that is at rest will begin motion in a laser field dictated by the Lorentz Force. For our electric field given by equation 2.17, it is clear that the equation of motion for the electron will be an oscillatory function in the \hat{x} direction. The velocity induced from the electric field then causes a force from the $\vec{v} \times \vec{B}$ component of the Lorentz Force, which lies in the laser propagation direction \vec{z} . However, if we substitute equation 2.17 into the Maxwell's equation $\nabla \times \vec{B} = \mu_0 \epsilon_0 \frac{\partial \vec{E}}{\partial t}$, we see that $B_0 = \frac{E_0}{c}$. Clearly, the magnetic field contribution can be ignored in this linear approximation.

This assumption is no longer valid for higher laser fields, where the velocity gained from the electric field causes the electron to move relativistically. When we consider an electric field of the form in equation 2.17, integrating equation 2.16 over time allows us to write the electron velocity amplitude as

$$v_{osc} = \frac{e_c E_0}{\gamma m_e \omega_0} \quad (2.19)$$

in what is known as the quiver velocity. At relativistic velocities, the quiver velocity is approximately equal to c . The magnitude of $\vec{v} \times \vec{B}$ is now on the order of E_0 , and it can no longer be neglected.

It is often convenient to consider a dimensionless parameter to consider the relative strength of the laser field. The relativistic region is defined when the electron momentum equals the rest mass of the electron, or when $\vec{p} = m_e c$. Both the electric and magnetic field may be expressed by the vector potential, which we will normalize with

$$a_0 = -\frac{e_c A_0}{m_e c} = \frac{e_c E_0}{m_e c \omega_0}. \quad (2.20)$$

The laser field is then relativistic once $a_0 \geq 1$. The conversion between practical and normalized units is found through

$$I\lambda_\mu^2 = a_0^2 \cdot 1.387 \times 10^{18} \frac{W\lambda_\mu^2}{cm^2} \quad (2.21)$$

showing that short pulse laser systems can achieve very relativistic interactions. Equation 2.16 can be written in terms of the normalized vector potential and the equation of motion can be solved⁶, revealing that

$$x = \frac{a_0}{k_0} \sin(\omega_0 t - k_0 x) \quad (2.22)$$

$$z = \frac{a_0^2}{4k_0} [(\omega_0 t - k_0 x) + \frac{1}{2} \sin(2(\omega_0 t - k_0 x))] \quad (2.23)$$

which results in a time average motion along the laser propagation given by

$$\beta_{Drift} = \frac{a_0^2}{4 + a_0^2}. \quad (2.24)$$

Thus that we see for low intensities the electron oscillates transverse to the laser propagation, while at high intensities it actually moves along with the laser. Note that for the high intensities, the motion in the transverse direction still occurs at the fundamental laser frequency. This is beautifully demonstrated in the drift frame, where the electron undergoes so-called “figure eight” motion (Fig. 2.5). This motion along the laser direction occurs with a frequency of $2\omega_0$.

2.2.3 Ponderomotive Force

The ponderomotive force is a force due to the spatial gradient of a high frequency electric field, such as is the case for a Gaussian focus. A rudimentary understanding may be found with the following argument⁷. An electron initially at the position of peak intensity will move laterally towards the outer diameter of the focus. There,

⁶For a derivation, see [48].

⁷A more mathematical derivation may be found in the appendix of [127].

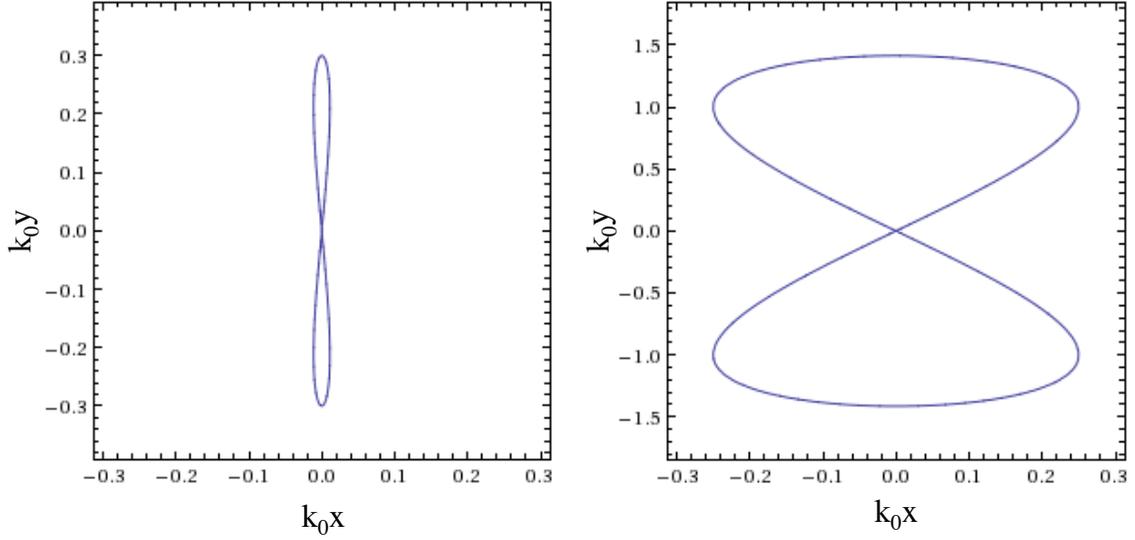


Figure 2.5: Electron motion in a linear plane wave at the electron rest frame. The left figure is for a small a_0 (0.3) and the right is for a large a_0 (100).

the electric field strength is lower, and the electron does not return to its starting point. Initially, let us consider an electric field that increases in a single transverse dimension, e.g., equation 2.17 where E_0 is replaced with $E(x) = E_0 x \hat{x}$. Substituting this electric field into the Lorentz Force equation (2.16) and neglecting the magnetic component, the equation becomes more difficult to solve. To simplify, we separate the electron motion $x(t)$ into a stationary, fast (due to the laser frequency) and slow varying component, such that $x(t) = x_0 + x_{fast}(t) + x_{slow}(t)$, with the assumption that $x_{fast} \gg x_{slow}$. We can now solve the Lorentz force equation through perturbation theory. Taylor expanding the electric field reveals

$$E(x) = E(x_0) + x_{fast} \frac{dE(x_0)}{dx} + x_{slow} \frac{dE(x_0)}{dx} + \dots \quad (2.25)$$

The force law to first order is then

$$\frac{d^2 x_{fast}}{dt^2} = \frac{-e_c}{m_e} E(x) \cos(k_0 z - \omega_0 t) \quad (2.26)$$

$$\frac{d^2 x_{fast}}{dt^2} \approx \frac{-e_c}{m_e} \left[E(x_0) + x_{fast} \frac{dE(x_0)}{dx} + x_{slow} \frac{dE(x_0)}{dx} \right] \cos(k_0 z - \omega_0 t) \quad (2.27)$$

where we can neglect the terms with partial derivatives since for high frequencies $E(x_0) \gg x_{fast} \frac{dE(x_0)}{dx}$. Then the first order solution can then be solved to

$$x_{fast} = -\frac{e_c E(x_0)}{m_e \omega_0^2} \cos(k_0 z - \omega_0 t) \quad (2.28)$$

We can now consider the Lorentz force equation with the second order perturbation term,

$$\frac{d^2 x_{fast}}{dt^2} + \frac{d^2 x_{slow}}{dt^2} = \frac{-e_c}{m_e} \left[E(x_0) + x_{fast} \frac{dE(x_0)}{dx} + x_{slow} \frac{dE(x_0)}{dx} \dots \right] \cos(k_0 z - \omega_0 t). \quad (2.29)$$

Subtracting out the first order motion from equations 2.26 and 2.28 we then see

$$m \frac{dx_{slow}^2}{dt^2} = e_c \left\langle x_{fast} \frac{dE(x_0)}{dx} \cos(k_0 z - \omega_0 t) \right\rangle \quad (2.30)$$

$$m \frac{dx_{slow}^2}{dt^2} = e_c \left\langle -\frac{e_c E(x_0)}{m_e \omega_0^2} \frac{dE(x_0)}{dx} \cos^2(k_0 z - \omega_0 t) \right\rangle. \quad (2.31)$$

Using the chain rule, the term $E(x_0) \frac{dE(x_0)}{dx}$ may be written as $\frac{1}{2} \frac{dE^2(x_0)}{dx}$. The time average of the cosine squared is $\frac{1}{2}$, and then combining terms

$$F_{Pond} = m \frac{dx_{slow}^2}{dt^2} = -\frac{1}{4} \frac{e_c^2}{m_e \omega_0^2} \nabla \|E\|^2 \quad (2.32)$$

which shows a slow motion in the direction away from the strongest electric field. A more general derivation allows for the ponderomotive force to be caused by other

components such as the magnetic field and circular polarization as well, so that this effect is seen for a number of situations. In terms of the Lorentz factor we can write the relativistic generalization of ponderomotive force as

$$F_{Pond} = m_e c^2 \nabla(\langle \gamma \rangle - 1). \quad (2.33)$$

Finally, the ponderomotive force can also act on ions as well, but it is much smaller due to the difference in mass (and thus difference in gamma). However, the dependence on charge falls out of the derivation, so although the charge of the particle is opposite the force is still in the same direction. Then the ponderomotive force will move ions much as they would electrons, albeit with smaller amplitudes.

2.2.4 Circular Polarization

All the previous analyses have been with regard to linear polarization. Consider the equation for a circularly polarized plane wave

$$\vec{E}(\vec{x}, t) = E_0 \left[\frac{1}{2} \cos(k_0 x - \omega_0 t) \hat{x} + \frac{1}{2} \sin(k_0 x - \omega_0 t) \hat{y} \right] \quad (2.34)$$

$$\vec{B}(\vec{x}, t) = E_0 \left[-\frac{1}{2} \sin(k_0 x - \omega_0 t) \hat{x} - \frac{1}{2} \cos(k_0 x - \omega_0 t) \hat{y} \right]. \quad (2.35)$$

In this case, the magnitude of the electric field is constant. Here, at low intensities electron motion is entirely circular. If we consider cylindrical coordinates, electron motion and velocity is entirely in the θ direction. Thus, the $\vec{v} \times \vec{B}$ term is zero. There will be no oscillatory figure 8 motion as there was in the linear case, just the slow drift that was presented in equation 2.24. When we consider the time average of a_0 , the cosine squared term for linear polarization yields $\frac{1}{2}$, while for the circular pulse it is 1. For two pulses with the same energy, we can relate the intensities by

$$\sqrt{\langle a_0^2 \rangle} = \frac{1}{\sqrt{2}} a_0 \quad (2.36)$$

implying that a circular pulse will have an a_0 that is roughly 0.7 times that of linear, since a_0 is the peak field strength.

2.3 Laser Plasma Interactions

The interaction of an intense laser pulse with a plasma is highly dependent upon the plasma density. The dispersion relation for an electromagnetic wave traveling through a plasma is given by

$$\omega_0^2 = \omega_p^2 + k_0^2 c^2 \quad (2.37)$$

where the plasma frequency is $\omega_p = \sqrt{\frac{n_e e^2}{\gamma \epsilon_0 m_e}}$. If the laser frequency exceeds the plasma frequency, the wavenumber becomes imaginary, and the light wave becomes evanescent. The point at which the laser frequency exactly equals the plasma frequency occurs at the critical density, and is the point where the plasma becomes opaque and reflective. The critical density can be found simply by solving the plasma frequency with $\omega_0 = \omega_p$, and in practical units it is

$$n_c = \frac{m_e \epsilon_0 \gamma \omega^2}{e^2} = 1.12 \times 10^{21} \frac{\gamma}{\lambda^2} [cm^{-3}]. \quad (2.38)$$

When the plasma is below the critical density it is referred to as underdense, and overdense when it is above.

2.3.1 Relativistic Effects

The common definitions of plasma parameters need to be refined for a relativistic pulse. The electron follows the relativistic energy momentum equation, so as it gains

velocity the momentum increases without bound. In the lab frame, this corresponds to a perceived increase in the electron mass. Then for the purposes of understanding the interaction the mass may be substituted with the relativistic effective mass γm_e , where we use the well known Lorentz Factor $\gamma = \sqrt{\frac{1}{1-\beta^2}}$. The normalized vector potential is related to the Lorentz factor by

$$\gamma = \sqrt{1 + a^2} \tag{2.39}$$

and in the limiting case that $a_0 \gg 1$, the two parameters are nearly identical (i.e., $\gamma \sim a_0$).

Relativistic mass has profound implications. The plasma frequency, for instance, decreases as the electrons larger inertia prevents the electrons from oscillating fast enough to re-radiate the incident laser. Thus it is possible for an opaque plasma to become transparent, in what is known as relativistically induced transparency. The concept of a skin depth needs to be revisited as well, as the classical plasma skin depth $\delta = \frac{c}{\omega_p}$. A laser can have a substantially larger penetration depth into an overdense plasma due to this effect.

Unfortunately, the practical realization of these parameters is much more complicated than simply quoting a number. A laser pulse propagates with a transverse profile that is not uniform⁸, resulting in a critical density surface that has a variable electron density. Further complicating the matter is that the density profile rarely is a step function, but rather an exponential ramp. Because of the nonuniform density, as the laser pulse simultaneously is lowered in intensity while the density increases the skin depth must be carefully considered. These considerations are critical for understanding the physics of an interaction at solid densities.

The intensity profile for any propagating electromagnetic wave through an under-

⁸It can come close as a super-Gaussian, but a discontinuity would require infinite spatial frequencies - an impossibility for finite energy pulses.

dense plasma faces a similar phenomena. Since the intense laser pulse will have a spatially varying intensity profile, traveling through a uniform plasma means a spatially varying plasma frequency. The index of refraction of a plasma is $n = \sqrt{1 - \frac{\omega_p^2}{\omega_0^2}}$, the index of a Gaussian pulse increases radially outward, acting as a lens. This causes relativistic self-focusing, which negates the effects of diffraction for a focus and can confine a pulse to a long channel [9]. This can be beneficial for LWFA, which can take advantage of the extended interaction region [47]. However, when undesired self-focusing occurs due to hot spots in the laser profile, the laser can filament into several smaller beams and the wavefront is lost. This is a critical consideration for plasma mirrors, as we shall see in chapter III.

2.3.2 Absorption

Laser energy can couple into the plasma through several various methods, dependent on intensity, density, polarization and incidence angle. Physically, this is because the absorption depends on whether the plasma is collisional, whether the laser can generate plasma waves, and whether relativistic effects come into play. In a laser produced plasma with solid densities, the number of electrons in a Debye sphere is large, and the electron temperature is sufficiently high so that the collisions are negligible. In this approximation, the plasma is called collisionless. In all of the absorption mechanisms discussed in this thesis the plasma may be considered collisionless, so the focus is on the collisionless processes.

2.3.2.1 Resonance Absorption

Resonance absorption is a moderate intensity process ($\sim 10^{15} \text{Wcm}^{-2}$) in which a P polarized wave reflecting at an oblique incidence angle on a plasma with a long scale length couples into the generated plasma wave. While there are many requirements for this process, it is a dominant mechanism in a wide variety of interactions including

reflection off a plasma mirror (See chapter III). The laser pulse experiences a varying index of refraction as the density rises, causing the laser to refract away from the critical surface. The laser never reaches the critical density itself, instead the index becomes evanescent at the density $n_e = \cos^2\theta n_c$ with θ being the angle of incidence.

For P polarization, the electric field has a component that is parallel to the surface normal. At the reflection point, Gauss's Law states that $\nabla \cdot (\epsilon \vec{E}) = 0$, and since $n = \sqrt{\epsilon}$ we have for a plasma that

$$\nabla \cdot \left[\left(1 - \frac{\omega_p^2}{\omega^2}\right) \vec{E} \right] = \nabla \cdot \left[\left(1 - \frac{n_e}{n_c}\right) \vec{E} \right] = 0 \quad (2.40)$$

with a clear resonance condition at the critical density. Although the laser reflection point is not at the critical density, the evanescent component may reach the critical density surface to drive this wave. Hence, the limit of grazing incidence or normal incidence, where the evanescent wave does not penetrate very deeply or there is no longitudinal component of the electric field ($\theta = 0$), a minimal amount of resonance absorption occurs. The optimal angle is dependent on the scale length of the exponential density profile. The absorbed fraction can reach up to 60%, an amount similar to collisional absorption [44]. The resulting electrons have a distribution function that is a Maxwellian determined by Landau damping of plasma waves driven at the critical surface.

2.3.2.2 Brunel Heating

For high-contrast experiments, the extremely sharp density profiles remove the potential for resonance absorption. This is physically because plasma waves cannot have wavelengths less than the Debye wavelength or else they would be damped by Landau damping in a single laser cycle. If we consider a step function density profile as an approximation, then we needn't bother with the evanescent wave at all as the critical density surface electrons can directly interact with the laser. In a

relativistically intense pulse, the electrons move in the laser field a distance of $\frac{v_{osc}}{\omega_0}$. For an oblique incidence angle with P polarization, the electrons will move in and out of the plasma by a distance of $\sin\theta\frac{v_{osc}}{\omega_0}$.

The practical implications of this motion are clear if an example is considered. A solid density plasma would have a skin depth on the order of 10 nm for an intense pulse, but the electron excursion distance will be $\approx 0.7\frac{c}{\omega_0}$, or on the order of 100 nm. Electrons will be pulled into the empty vacuum, and then plunge into the dense plasma. However, the laser is rapidly attenuated before the electron can come to a stop, so the electron does not experience a returning force and continues into the target as an energetic particle. This insight was first described as what is now termed Brunel heating, or vacuum heating[12]. For high intensity pulses, the absorption is given by

$$\eta = \frac{4\pi \frac{\sin^2\theta}{\cos\theta}}{(\pi + \frac{\sin^2\theta}{\cos\theta})^2} \quad (2.41)$$

showing a maximum for incidence angles near 75 degrees.

2.3.2.3 jxB Heating

Normal incidence would then appear to be the regime to limit absorption, however, there is yet another mechanism that prevents absorption from being eliminated. For a single electron, it was discussed that the $\vec{v} \times \vec{B}$ component led to a drift velocity given by equation 2.24, regardless of polarization. At a surface of a steep density gradient plasma, the electrons will move forward into the overdense plasma where the laser can no longer propagate. This is known as relativistic $\vec{j} \times \vec{B}$ heating [71].

The electrons accelerated will have a Maxwellian distribution function with a temperature that is given by

$$U_P = mc^2(\gamma - 1) \quad (2.42)$$

with U_p being the ponderomotive potential. The ponderomotive potential is related to the ponderomotive force via

$$F_{Pond} = -\nabla U_p \quad (2.43)$$

For a circularly polarized pulse with an a_0 of 20, the electron temperature will be ≈ 9.7 MeV. For linear pulses, the $2\omega_0$ driving force causes the electrons to be generated in bursts at $2\omega_0$ [136].

2.3.3 Parametric Instabilities

To understand parametric instabilities in plasmas it helps to understand physically what a parametric instability is. A classic example is a pendulum with a time varying parameter, such as the damping parameter or the location of the origin. In the latter case, if the origin oscillates harmonically then the solution of the pendulum angle can be given by $\theta \sim t \sin(Ct)$ with the addition of the oscillatory terms assuming the oscillations at the origin are small [73]. The solution includes an amplitude that increases with time. A practical example of such a system is a child on a swing.

In the case of a plasma, we can replace the pendulum with the plasma itself. Plasma waves will oscillate at ω_p , and the perturbation is the laser. Many parametric instabilities exist for a variety of plasma conditions and laser parameters [70], two of the most important for solid density, short pulse interactions are Stimulated Raman Scattering (SRS) and Two-Plasmon Decay (TPD).

In SRS, a relativistically intense laser pulse with frequency ω_0 can scatter off of a plasma wave of frequency ω_p . When the scattered light beats with the laser pulse, energy is coupled into the plasma wave and the amplitude grows, creating a positive feedback loop where more laser energy is coupled into the scattered pulse. This can manifest in light being scattered in the forward direction, backscattered, or in between. In TPD, the laser can couple into two plasmons, quantized units of the

plasma wave at the quarter critical density surface, and amplify the plasma wave.

From an argument of conservation of energy ($\hbar\nu$ is constant) and conservation of momentum ($\hbar\vec{k}$ is constant), it may be expected that

$$\omega_0 = \omega_p \pm \omega_{SRS} \quad (2.44)$$

$$\vec{k}_0 = \vec{k}_p \pm \vec{k}_{SRS} \quad (2.45)$$

the phase matching conditions for these instabilities. The conditions for SRS and TPD depend on the electron density. The limiting case of SRS is when the scattered wave cannot propagate because it exceeds the plasma frequency. At this maximum $\omega_{SRS} = \omega_p$, and from equation 2.44 it must be true that $\omega_0 \geq 2\omega_p$, i.e., that the plasma density must remain below $\frac{n_c}{4}$. This is a weaker condition than for TPD, which can only occur for $n_e = \frac{n_c}{4}$.

2.3.4 Radiation Generation

Another route of energy loss for the laser is the conversion of light into other frequencies. During a laser cycle, the electron's velocity varies between rest and $\sim c$, and due to relativistic effects the motion is no longer harmonic. The model most often used to describe HHG from a solid surface is the relativistic oscillating mirror model [79]. In this model, the electrons at the surface are driven by the laser, and for linear polarization the surface is driven to first order by the $2\omega_0$ frequency from the $\vec{v} \times \vec{B}$ force. If we only consider this motion, then the motion of the surface of the plasma can be approximated as $\sim \sin(2\omega_0 t)$. Since the source of the radiation is now from a moving source, we can describe it with a retarded time $t' = t - \frac{R - R_0 \sin(2\omega_0 t)}{c}$. Then a plane wave that is reflected from this surface will have a field given by

$$E_{ref} = E_0 \cos(\omega_0 t + 2R_0 \frac{\omega_0}{c} \sin(2\omega_0 t)). \quad (2.46)$$

The electric field becomes strongly distorted, as seen in Fig. 2.6. The Fourier transform of such a field will no longer yield a single frequency, as the square profile requires higher frequency components, and the result is a harmonic spectra. Here the electron motion is oversimplified, but serves to act as a demonstration that harmonics should be expected. A more rigorous description of the analytical theory is given in [79, 51], although some general trends may be extracted from this simple model. For example, the maximum harmonic exists due to the finite motion of the surface oscillation. The time dilation from the mirror moving a half cycle is $4\gamma^2$, and the maximum harmonic is $4\gamma^2\omega_0$ after which the spectra decays off exponentially.

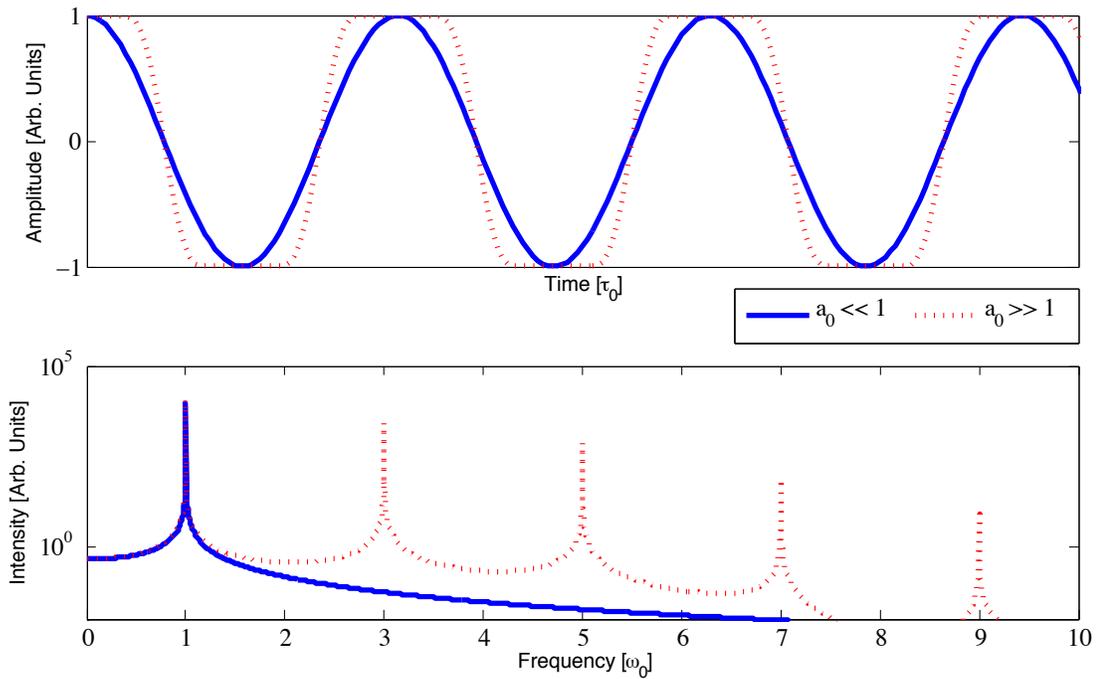


Figure 2.6: Electric field solution for a reflected beam of a $2\omega_0$ driver for low amplitudes (blue) and high amplitudes (red). The bottom graph shows the Fourier transform of the produced spectra, and the harmonics are clearly visible.

In the previous derivation, only odd harmonics were generated. Even harmonics must be generated as well, resulting from interactions at oblique incident angles. For oblique incidence angles, the electrons are also accelerated by the electric field whether into the vacuum or along the laser axis. This coupling occurring at ω_0 provides the means for generating even harmonics. At normal incidence this cannot occur and only odd harmonics are produced. In the case of normal incidence circular polarization, no harmonics should be produced since the $2\omega_0$ driving force is no longer present.

2.4 Ion Acceleration Mechanisms

Ions are much more massive than electrons, and for many experimental situations with short pulses it is common to assume the ions stationary. However, control of the electron motion allows for control of powerful electric fields, which in turn can control ion motion. While a number of acceleration mechanisms exist for a wide variety of plasmas, this section is restricted to the realm of thin solid density targets. A good review of underdense and near critical density ion acceleration schemes is discussed in [138]. All of the following interactions are described generally by a laser pulse focused to high intensities on a solid planar target. Electrons are manipulated in the manner desired, and the resultant fields move the ions. The least complicated of these schemes is TNSA, and as more and more restrictions are placed on the interaction the parameters of the ions accelerated may be controlled further.

2.4.1 Target Normal Sheath Acceleration

The TNSA process is one of the most widely studied mechanisms. At the most fundamental level, hot electrons generated by the laser pulse that scatter to the surface of the target invariably form a sheath. Conversely, it is the most studied since it is very difficult in practice to do anything else. Any other method requires the suppression of hot electrons or very strict control over hot electron motion, and even

then a TNSA presence is still likely. Thus, it is the most important mechanism to understand.

Previously, a number of absorption mechanisms were described that generated hot electrons. The intensities are high enough such that everything at the focal area will be immediately ionized. The electrons have a Maxwellian distribution function, and will rapidly travel to the rear of the target. The large current produces a large magnetic field. A small portion of the hottest electrons will simply leave the target, while the rest of the electrons will scatter around the target. The electrons that leave the plasma are confined to a layer on the order of the Debye length $\lambda_d = \sqrt{\frac{\epsilon_0 k_B T_e}{n_e e^2}}$, where they can form an extremely strong space charge field. At the rear of the target, the electrons have a distribution of $n_e = n_{e0} \exp(-e_c \Phi / k_B T_e)$ where k_B is the Boltzmann constant and Φ is an electrostatic potential that satisfies the Poisson equation. The ions on the surface will begin to be accelerated; protons, with their large charge to mass ratio, are accelerated first followed by the other light ions. An ion front forms, between the quasi-neutral plasma and the electron sheath. This ion front leads to a sharp cutoff in ion energy, giving rise to the measurable maximum ion energy.

The sheath does not exist permanently, rather, it dies off on the order of the pulse duration. Because of this, there is a finite acceleration time and the ions attain a finite energy. The initial electric field is given by

$$E_{sheath} = \sqrt{\frac{2}{\exp(1)} \frac{T_e}{e_c \lambda_d}} \quad (2.47)$$

which has an approximate solution [96] for the maximum ion energy at time t of

$$\xi = 2Z_{ion} T_e \left[\ln \left(\frac{\omega_p t}{\sqrt{2\exp(1)}} + \sqrt{\frac{\omega_p t}{\sqrt{2\exp(1)}^2 + 1}} \right) \right]^2 \quad (2.48)$$

which is found by the kinetic energy of the ion front.

A number of assumptions have already been made in these 1D treatments. Many studies assume that the electron temperature follows the ponderomotive potential, however, another scaling has been shown experimentally in the case of short pulses with high contrast. The Beg scaling follows

$$T_{Beg} \approx 0.47m_e c^2 a_0^{\frac{2}{3}} \quad (2.49)$$

implying that the maximum ion energy will be diminished. Effects of the pre-plasma on the maximum ion energy have been performed [62], suggesting that there is a strong dependence on the plasma initial conditions.

2.4.2 Radiation Pressure Acceleration

The presence of hot electrons in the target gives rise to TNSA, however, other novel acceleration mechanisms exist. A promising approach on accelerating the foil comes from the notion of radiation pressure, that light itself carries momentum and upon reflection transfers that momentum [38]. This is called radiation pressure acceleration (RPA) of ions. Two approaches are made, one in which the momentum is directly transferred to an infinite target and the resultant piston of plasma drives the ions to high energies. This model has been described as the laser-piston regime [40] or the hole-boring mode of RPA [83]. The amount of momentum necessary to bore a semi-infinite layer requires either extremely high laser intensities ($> 10^{23} \text{Wcm}^{-2}$) or densities near n_c [104]. The difficulty of making a suitable near critical density target for a NIR laser as well as the lack of suitably high intensity lasers prevents experimental study using the HERCULES laser.

The other regime of RPA is the light sail regime [114], in which the target is thin enough for the laser to rip out the focal area. The laser then transfers momentum to the small focal area plasma rather than the bulk and efficient acceleration can be achieved, analogous to the concept of a light sail for space travel [91]. Because the

entire foil is accelerated, the ions will all have the same velocity. To consider the amount of energy that can be delivered to the foil, we consider the radiation pressure $F_{rad} = \frac{\langle S \rangle}{c}$. Considering the intensity in the rest frame of the foil $\frac{I'}{I_0} = \frac{1-\beta}{1+\beta}$, with β being the relativistic velocity of the foil, the radiation force can be expressed in terms of momentum as

$$F_{rad} = \frac{dp}{dt} = \frac{2I_0}{c} \frac{\sqrt{p^2 \sigma_{Area}^2 c^2 - p}}{\sqrt{p^2 \sigma_{Area}^2 c^2 + p}} \quad (2.50)$$

where the surface area of the target is σ_{Area} . Hyperbolic functions are useful for handling nonlinear differential equations such as the above, since $\cosh^2(x) - \sinh^2(x) = 1$. Equation 2.50 can then be solved [114] with a solution of the form

$$p = \sigma_{Area} c (\sinh(\chi) + \frac{1}{4} \sinh(\chi)) \quad (2.51)$$

with

$$\chi = \frac{1}{3} \sinh^{-1} \left[\frac{6I_0 t}{m_{Ion} c^2 n_{Ion} l} + 2 \right] \quad (2.52)$$

and l as the foil thickness.

Control of the hot electron population is achieved by circular polarization. Since there is no longer any $\vec{j} \times \vec{B}$ heating, at normal incidence the electrons will only move slowly through the ponderomotive force. There is an optimal thickness for the target that is determined by considering pressure balance. In the light sail model, electrons are pushed forward by the ponderomotive force, while the ions are initially still. The space charge developed will pull the electrons back if it gets too large, and if it is too small the electrons will simply leave the target. If electrons exist outside the target, then those fields will accelerate the target ions via TNSA and the RPA effect is lost.

The electrostatic field from electron displacement is given by Gauss' Law as $E = \frac{e c n_0}{\epsilon_0} \Delta x$, where the displacement of the electrons is given by Δx . Equating

this displacement force with the equation 2.50 and writing in terms of a_0 it can be shown [142] that

$$a_0 \approx \frac{n_0}{n_c} \frac{l}{\lambda_0} \quad (2.53)$$

for a hydrogen foil.

The requirements for RPA are strict. There must be no hot electron generation, and while this is entirely achievable in a one dimensional geometry it will be shown in chapter V that there are significant experimental difficulties due to finite spot effects. The foil must be thin enough to satisfy equation 2.53. For a HERCULES-type laser with an a_0 of 30, a solid density foil of $n_e = 300n_c$ would need to be 80 nm. The previous models assume only one ion species, problematic since the contaminant layer alone consists of 3 separate species⁹ in significant number.

2.4.3 Breakout Afterburner

The RPA mechanism requires ultrathin targets in order to achieve efficient acceleration. However, efficient reflection occurs when the target is thick enough so that the light is able to reflect and transfer momentum. If the target is too thin, relativistic transparency may allow the laser to leak through. However, if the light is able to penetrate throughout the focal volume while it is relativistically transparent, then the entire focal volume will experience electron heating. The heated electrons are able to form strong electric fields that can accelerate ions in a process known as Break-out Afterburner [145].

The Break-out Afterburner actually describes the late time acceleration phase that occurs for a thin target interaction. Initially, the laser interacts with an overdense plasma via TNSA and ions are only lightly accelerated. As the electrons are accelerated to relativistic velocities, they leave the interaction area. Thus the plasma

⁹Hydrogen, Carbon, and Oxygen.

frequency of the target decreases as the density decreases and γ increases. The implication of this dynamic is that there is a build up of a longitudinal electric field, due to the ponderomotive force and the electron displacement.

A certain point arises when the electrons become relativistically underdense. When this point occurs, the laser can freely penetrate the target and can generate a high temperature beam. The presence of such an electron beam gives rise to the resonant Buneman instability, a type of two-stream instability where ions are accelerated in the electron direction. The acceleration is very strong, and will proceed until the target becomes classically underdense. Target thickness must be carefully chosen such that the target becomes relativistically underdense just before the peak of the pulse, otherwise the target simply is at too high or low an intensity.

However, although it provides a greater conversion efficiency and higher energies, the ion spectra is still exponential as it is in TNSA. In contrast to the RPA mechanism, the breakout afterburner has successfully been shown to generate high energy ions in experiment [55], although there is difficulty in determining a particular signature to differentiate this mechanism from other mechanisms.

2.4.4 Directed Coulomb Explosion

In the case that the target never becomes underdense, the Break-out Afterburner can never be realized. The ions will still be accelerated forward due to charge separation and the ponderomotive force. For a sufficiently intense laser pulse the build up of space charge in the interaction region will begin to undergo a Coulomb explosion. For a high and low atomic number plasma¹⁰, the hot electron sheath will separate the plasma into two distinct regions, giving rise to an enhanced longitudinal field. When the Coulomb explosion occurs, the low atomic number species is preferentially accelerated in the forward direction. This mechanism is known as the Directed Coulomb

¹⁰Such as a proton carbon plasma.

Explosion regime [13], and occurs for intensities of $> 10^{22} \text{Wcm}^{-2}$. The Directed Coulomb Explosion mechanism is a combination of a Coulomb explosion and RPA, however, does not have the requirement that circular polarization be used. Linear polarization is a requirement, as the electrons must be heated in order to evacuate the focal volume.

2.4.5 Ion Acceleration Challenges

Compared to TNSA, the other ion acceleration mechanisms offer substantial improvements in either energy, energy spread, or both; however they have far more stringent demands experimentally. While these novel mechanisms have been successfully simulated in PIC codes, there are major assumptions that are made to produce the desired ion spectra. There is a very good reason for this to be the case. The interactions are inherently very complex, and developing analytical models is prohibitively complicated in most cases. The use of a one dimensional model can provide a useful interpretation of the physics, and allow some models to be rigorously developed.

Without experiments, the only method of validating new models is to use numerical simulation. To approximate the one dimensional models, it is a common practice to use a flat top spatial profile. Wide focal diameters are also used, with extremely high intensities. Density profiles are commonly step functions as well, and the laser pulse duration is generally either a perfect Gaussian or a flat top function. The results of the simulations then agree perfectly with the models, since they collapse the multi-dimensional case to the one dimensional model. Although this verifies the physics of the model, it under-utilizes the simulation in that realistic parameters are not introduced.

CHAPTER III

Methods & Capabilities

The results discussed in this thesis were conducted primarily at the HERCULES Laser facility at the University of Michigan, which is the flagship laser of the high field science group at the Center for Ultrafast Optical Science (CUOS). As part of this thesis research in the experimental area for solid target interactions, high contrast and high intensity capabilities were designed, implemented and characterized. A battery of diagnostics was employed to obtain as much information about the interaction as possible, under the experimental limitations due to the use of using sharp focusing optics. However, there are many experimental parameters that are difficult and impractical to measure making numerical simulations of the experiment critical for gaining insight into the interaction and interpreting data correctly.

3.1 HERCULES Laser Facility

The high energy, high repetition-rate CUOS laser system (HERCULES), is a CPA laser with a peak output power of 300 TW [143]. The laser consists of several major components consisting of the front end, including the oscillator, pre-amplifier, stretcher, and pulse cleaner; the power amplifiers which include regenerative amplifier, and several multipass amplifiers; and finally the compressor (See Fig. 3.1 for particular details.). The oscillator produces seed pulses at 12 fs with a spectral band-

width of ≈ 50 nm at a central wavelength of 790 nm. A pre-amplifier consisting of a double pass Ti:sapphire crystal amplifies this seed pulse so that the intensity is high enough to allow for the nonlinear interactions required for the pulse cleaning technique known as cross-polarized wave generation, or XPW [107]. This technique exploits the four wave mixing nonlinearity that is intensity dependent such that the polarization of the output pulse is shifted when the nonlinearity is present. The particular design of the system has been discussed previously [111, 23].

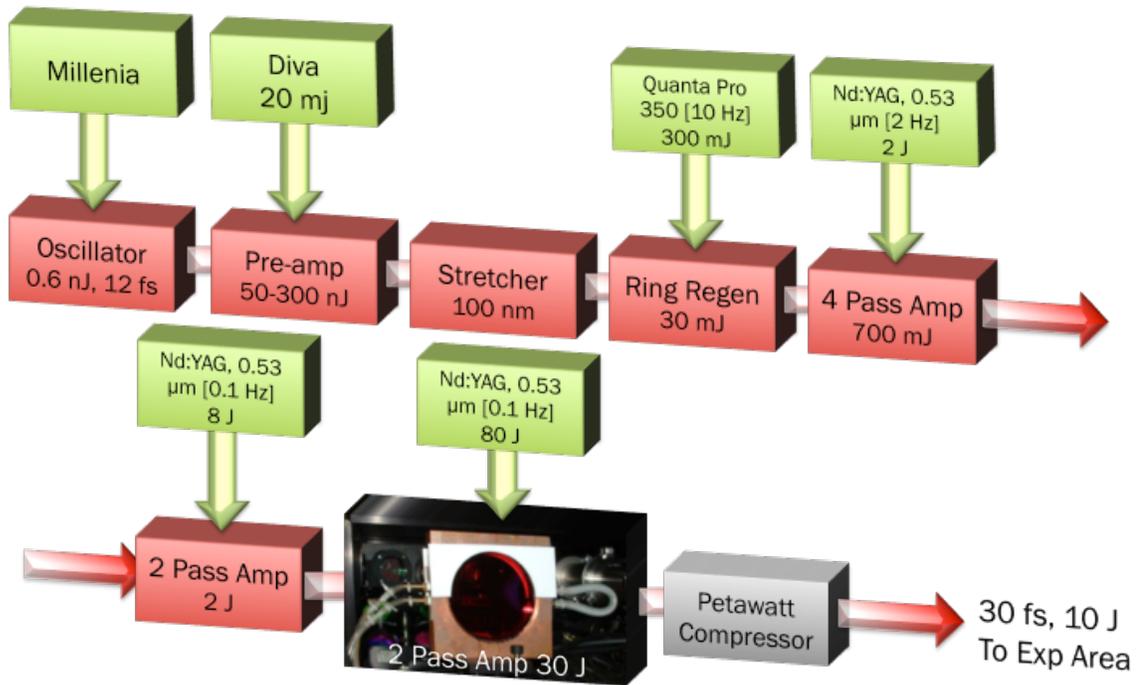


Figure 3.1: Schematic diagram of the HERCULES laser system.

After the preamplifier, the pulse is stretched to 350 ps for amplification below the damage threshold of the optics. A regenerative amplifier amplifies the beam to nearly 1 mJ of energy, at a repetition rate of 10 Hz. Afterwards, the pulse enters the 3 power amplifiers that are multipass Ti:Sapphire amplifiers that increase the laser energy to 0.6 Joules, 2 Joules, and finally to 18 Joules respectively. This stretched pulse then enters a vacuum chamber where compression occurs. Here the beam is reflected from a series of 4 gold-coated, holographic gratings aligned in the “Treacy” configuration

[129, 11] (Fig. 3.2). By geometrically varying the path length of each wavelength, the linear chirp introduced by from the matched stretched grating can be compensated. Unfortunately, orders of dispersion higher than the fourth order are not compensated, and misalignment of the gratings as well as spatially varying dispersive effects mean that the pulse is unable to be compressed to its original duration. In addition, gain narrowing can decrease the available bandwidth so that the minimum pulse duration is ultimately limited by the time-bandwidth product (See 2.1). For a 800 nm pulse with a spectral bandwidth of 30 nm, this corresponds to a 32 fs pulse duration. The experiments performed in this thesis were performed with pulse durations in the range of 32 fs to 41 fs. The diffraction gratings each have a diffraction efficiency of $\sim 90\%$ of the incident pulse so that after 4 reflections there is significant energy loss from the compression. Although the compression throughput measured via calorimeter was $63\% \pm 2\%$, experiments are conducted with the assumption of 50% of the laser output energy measured prior to the compressor to account for all other optical losses in the system.

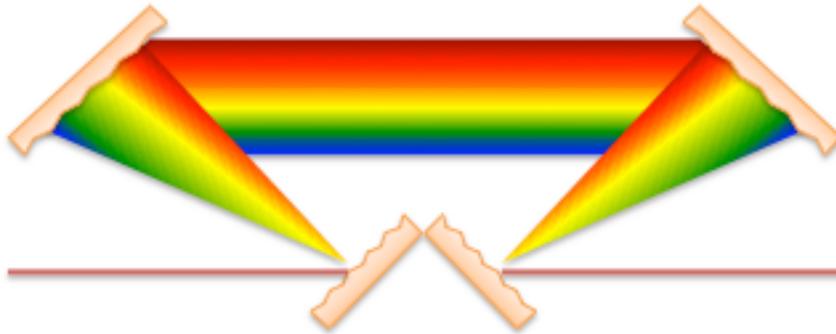


Figure 3.2: Schematic diagram of a Treacy double pair grating compressor. Negative Group Velocity dispersion occurs since the optical path length of blue light is shorter than that of red, compensating for dispersion elsewhere in the laser system. The separation of each pair controls the amount of dispersion added.

3.1.1 Solid Target Experimental Area

The HERCULES laser facility has an experimental area dedicated to the investigation of solid target interactions. Due to the increased radiation generated at the interaction site, shielding must enclose the vacuum chambers for high power shots. In addition, the necessity for high throughput plasma mirrors requires secondary chambers suited for long focal length focusing optics. The experimental chamber is cylindrical to allow optical ports equal solid angle to the interaction site of the target chamber center. A typical experimental setup is shown in figure 3.3. A key feature of this setup are the removable mirrors in the plasma mirror chamber, which can redirect the incident laser pulse to a cascading set of plasma mirrors. All of the optics employed for main beam manipulation are reflective optics, as any refractive optics for this beam diameter would produce undesirable effects such as pulse broadening due to dispersion or wavefront degradation due to B integral (2.10). All sharp focusing optics are aspheric, and ray tracing has been performed for the few long focusing spherical mirrors to show that pulse broadening from the spherical aberration is limited to less than 3 fs.

3.2 High Contrast Capabilities

3.2.1 Pre-compression Cleaning

It is possible to improve temporal contrast of the laser pulse through a variety of techniques. To minimize ASE production, most of the gain in the laser system occurs in the regenerative amplifier [144]. Although the extraction efficiency is not as high as multipass amplifiers, many passes are able to be performed so that overall gain can be very high. In the system employed at HERCULES, the cavity for the regenerative amplifier is relatively long, meaning that the solid angle required for ASE to enter the system is small. This results in an energy contrast of greater than 10,000 on

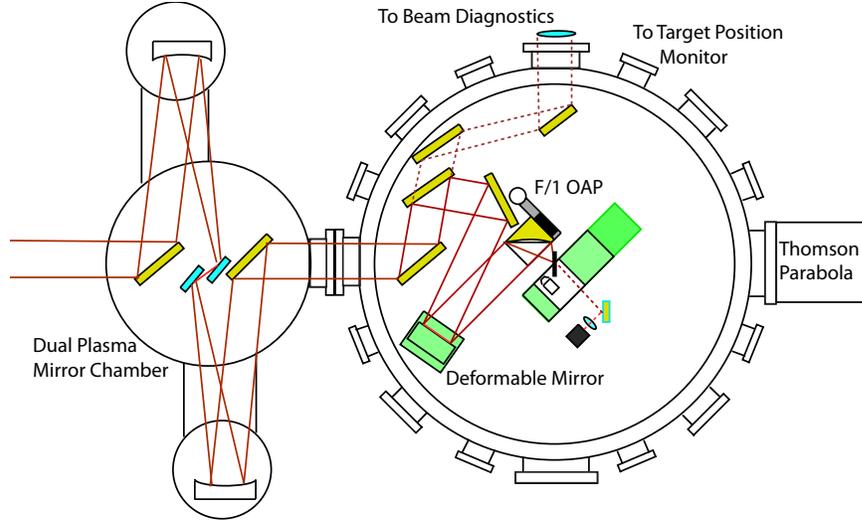


Figure 3.3: Typical experimental setup of the solid target experimental area. Drawing not to scale.

the nanosecond level. The XPW is capable of increasing the nanosecond intensity contrast to 10^{-11} [23]. The contrast improvement occurs because the weaker ASE will not be intense enough to exhibit significant nonlinearity, increasing the contrast prior to pulse stretching.

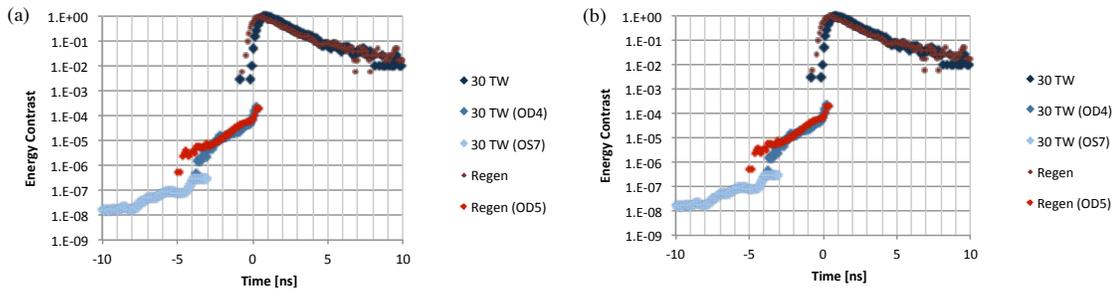


Figure 3.4: (a) Full regen shown with XPW engaged (red) and without (blue). (b) Comparison between 30 TW shots (blue) and the full regen with XPW engaged (red). This shows that there is no significant increase in contrast for full power shots.

An active pulse cleaner is employed using the XPW technique ¹. In a medium with an anisotropy with third order susceptibility χ , a wave can be generated in the

¹The use of this technique throughout this thesis will be referred to as simply XPW.

four wave mixing process such that two frequencies are generated. For the case of XPW, the particular wave mixing process of interest is a degenerate form with $\omega_{\perp} = \omega_{\parallel} + (\omega_{\parallel} - \omega_{\parallel})$ when the initial wave is linearly polarized along the axis of anisotropy. A crystal with very little birefringence, such as BaF₂, allows phase matching between the orthogonal frequencies. Saturation of this mechanism places an upper limit of efficiency at $\sim 10\%$, so it is common practice to use two crystals, the second crystal rotated with respect to the first. By placing a polarizer in orthogonal directions on both sides of the crystal pair, we select the output to be the beam rotated by the nonlinearity. As a third order non-linear process, XPW is dependent on the electric field cubed, allowing significant discrimination with respect to the ASE. Due to the high fluence in the HERCULES beam it is only practical to perform XPW at the front end where the beam size is small and high quality crystals may be purchased. The two crystal BaF₂ scheme has been employed at the HERCULES front end as a pulse cleaner, that allows the nanosecond contrast to be improved to a level of 10^{-11} [23].

The HERCULES XPW has an additional advantage beyond increasing the temporal contrast of the seed laser. The pre-amplifier also introduces substantial gain (1,000) to the pulse, meaning that the regen may be pumped at a lower power so that less ASE is generated, further enhancing the contrast. The effects of the XPW on the nanosecond level can be compared by using a fast response (≤ 1 ns) photodiode. Once the diode is saturated it can no longer provide meaningful data, so to increase the dynamic range of the diode a series of neutral density filters are placed in front of the diode to observe the response over a larger range of intensities. The measurement can be taken prior to compression where the pulse will have a lower damage threshold since the rise time of the diode is still long compared to the pulse duration. An increase of several orders of magnitude can be seen with the XPW in Fig. 3.4. The comparison was made at the regen amplification level for safety reasons, however, a

comparison between full power shots (30 TW) shows that the power amplifiers do not add any discernible ASE contrast. This can be attributed to the fact that although the 30 TW and 300 TW amplifiers add significant amounts of energy to the pulse, the overall gain in these amplifiers is still small compared to the regen.

3.2.2 Staged Plasma Mirrors

While the HERCULES setup provides a high inherent contrast rivaling even optical parametric CPA lasers [65, 4], there is little that can be done for contrast improvement on the picosecond time scale with respect to the laser design. This necessitates the need for a cleaning technique that operates beyond the compressor. By no means is this an easy task, since the fluence of the laser post compression is nearly at the damage threshold of the optics used to manipulate the beam. However, although the main pulse is near to damage threshold, the prepulse remains several orders of magnitude below, precipitating the scheme for contrast improvement for short pulses.

By focusing the main pulse onto an optic such that the main pulse will form a plasma on the rising edge of the pulse, the reflective properties of the optic can be exploited for pulse cleaning. This shuttering is commonly known as plasma mirrors (a photograph of one in operation can be seen in Fig. 3.5 (a)), and extensive characterizations of the use of plasma mirrors has been performed on a variety of laser systems [34, 33]. The reflectivity of the prepulse, which is designed to be below the damage threshold, is dictated by the optic used while the main pulse will have a reflectivity based on the intensity alone. If plasma expansion is limited to picoseconds within the main pulse, so that overall expansion is much less than the wavelength, optical quality is maintained. For short pulses, the ion motion is negligible during the pulse duration so the effect on the pulse duration is also negligible. The contrast improvement can be characterized by the ratio of the reflectivity of the prepulse compared to the main.

Further increases in contrast improvement can come at a cost of laser energy. For

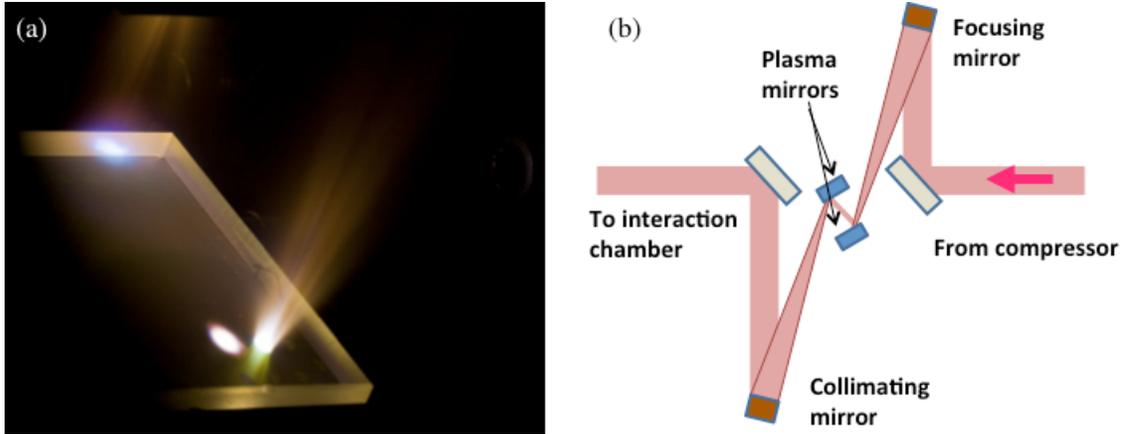


Figure 3.5: (a) Photograph of plasma mirror during the experiment. The plasma expands after the interaction into a jet near normal to the surface. (b) Schematic drawing of the dual plasma mirror configuration.

the experiments presented here, a dual plasma mirror setup was used in a manner laid out in Fig. 3.5. The benefits of such a scheme are that the experiment can very quickly deploy plasma mirrors without significant realignment since the laser exits the plasma mirror telescope with the same divergence as it would had it not entered. The plasma mirrors are coupled and on an in-plane positioning system so that they may be rastered for each shot. The plasma mirrors for use at the HERCULES facility were fully characterized for use in experiments.

3.2.2.1 Plasma Mirror Characterization

To ensure that the introduction of the plasma mirrors increased contrast without disturbing the pulse wavefront, a series of characterization measurements were conducted. A single plasma mirror was measured first. The laser was focused onto the plasma mirror at a 50 degree angle with an $f/15$ off-axis parabolic mirror (OAP). The mirror was placed on a translation stage in the laser axis direction so that the mirror could be positioned on either side of the focus to measure the reflectivity versus intensity. The near field intensity profile of the OAP is not symmetric on either side of focus, so average intensity (and thus reflectivity) may not have been the same on

either side of focus. A wedged fused silica optic reflected the beam to lower intensity and prevent damage. This beam was recollimated with a lens and sent into the experimental chamber where it was sent into a large area calorimeter to measure energy throughput. A dielectric mirror transmits $< 0.1\%$ of the incident beam, which is sent into a fast rise time diode to measure contrast; and into a lens which focused the beam onto a pair of CCD's to examine wavefront quality. A single mirror was found to reduce the contrast on the nanosecond level in accordance with the reflectivity of the coating of the plasma mirror. 2 types of coatings were used, one from an “off the shelf” anti-reflective glass plate which had an oblique reflectivity of 2% ² and a custom made high damage threshold coating with a peak reflectivity of 0.15% across the laser bandwidth ³. A small strip of gold was coated along an edge of each plasma mirror for alignment.

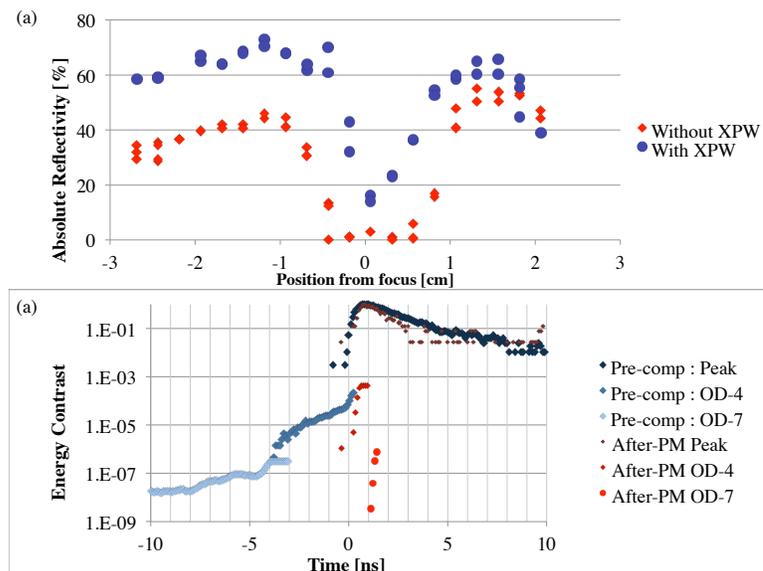


Figure 3.6: (a) The reflectivity of a single plasma mirror as a function of position relative to the focus of the OAP for the case of without XPW (red) and with XPW (blue). (b) The measured contrast improvement with a pair of plasma mirrors. With two plasma mirrors the nanosecond prepulse is below the detection threshold of the diode, indicating contrast improvement of better than 3 orders.

²Edmund Optics part number NT83-478

³Coating produced by Alpine Research Optics

The reflectivity of the main pulse was found to vary from 52% at $9.5 \times 10^{14} \text{Wcm}^{-2}$ to a maximum of 73% at $4 \times 10^{15} \text{Wcm}^{-2}$, which is in excellent agreement with previous experimental results [33]. When the intensity is increased, the reflectivity begins to decrease due to preplasma formation, as shown in Fig. 3.6 (a). Dual plasma mirror operation was setup in the manner previously described, in which the temporally cleaned pulse enters the experimental chamber with the same divergence as the uncleaned beam. After reflecting off of an uncoated surface and having neutral density filters placed in the beam to reduce intensity, the beam was imaged with both a $F/12$ and a $F/1$ imaging optic to measure the spot size, showing no significant deviation from the uncleaned beam of comparable power. The dual plasma mirror configuration utilizes S polarization to minimize resonance absorption. The dual plasma mirrors are aligned to be parallel to one another to prevent deviations in alignment when the plasma mirrors are restored. The separation of the plasma mirrors are chosen to have slightly higher intensity on the second mirror. With the laser partially cleaned a higher intensity may be placed on the second mirror before preplasma forms. In the experimental setup, the plasma mirror separations are fixed with the focus in between both mirrors, however the mirror pair may be translated along the laser axis to vary the intensities on each mirror. With a separation of 4.8 cm, the reflectivity from both mirrors was between 48 and 52 %, and if the fluence on either mirror was too high the reflectivity suffers and the wavefront displays signs of filamentation. The contrast improvement from both mirrors produces a nanosecond energy contrast beyond the dynamic range of the photodiode. The leading edge of the laser pulse was very sharp, limited by the diode response (Fig. 3.6 (b)). The expected contrast improvement is then 3 or 5 orders of magnitude, depending on which plasma mirrors were used.

When the plasma mirror was placed at the focus of the telescope, where the intensity was at its maximum of 10^{17}Wcm^{-2} , the reflectivity was on the order of several percent. Without the XPW, there was minimal reflectivity at plasma mirror

positions up to a cm away from focus, with the XPW the range of minimum reflectivity was reduced to within microns of the focus. In addition, the maximum reflectivities observed were higher with the XPW engaged. To understand why this may be the case, a series of 1 dimensional hydrodynamic simulations using the code HYADES were conducted [74]. A third order autocorrelator measurement of the HERCULES laser with and without XPW was used to provide a temporal intensity profile to use for the simulations. For various order of magnitude intensities, a piecewise fit of the autocorrelator trace normalized to the intensity on the plasma mirror was used to see hydrodynamic expansion of the target, which is assumed to be the dominant expansion at these intensities with these pulse lengths. As expected the scale length produced varies with intensity, as seen in Fig. 3.7. When we consider the differences between the effects of the prepulse with and without XPW, we see that for the optimal conditions of plasma mirror operation, the scale lengths from the two cases are identical but for higher intensities they are significantly different, with the plasma expanding beyond the laser wavelength without XPW.

Reality differs from 1D in the sense that the laser profile on the plasma mirror is not uniform, so while we can estimate the average intensity, local intensities may vary dramatically. These intense hotspots may form a significant preformed plasma locally, causing a disturbance in the wavefront and scattering away light. In addition, a larger preplasma will have a larger volume to absorb laser energy, decreasing reflectivity. This provides an explanation for the differences observed in the reflectivity versus intensity for the different contrast cases. It is important to note that the simulated temporal profile averaged out high frequency modulations, which may further enhance preplasma formation on the plasma mirrors. While one would be tempted to believe that even a laser with a contrast of 10^{-7} should experience adequate cleaning with plasma mirrors, this may not always be the case. It is critical to remember that while it is convenient to describe the laser contrast with a single number, the temporal

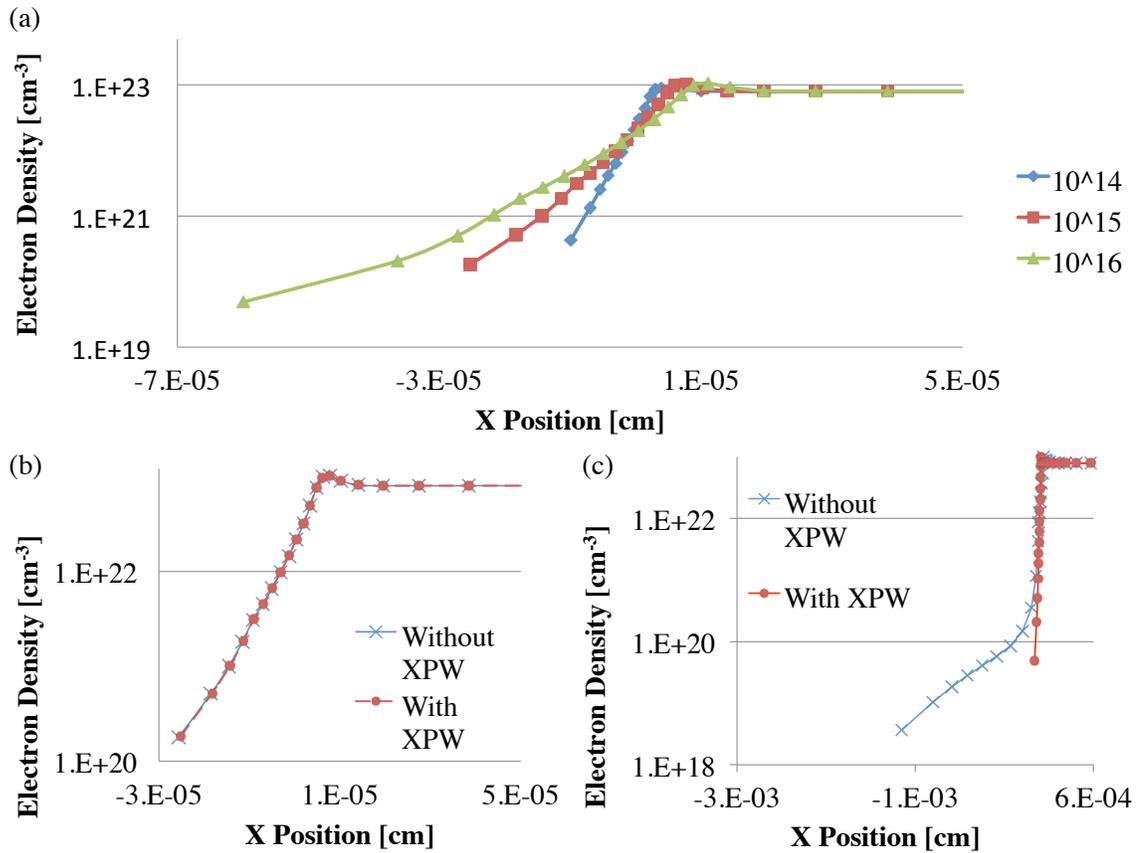


Figure 3.7: 1D Hydrodynamic simulations of the HERCULES prepulse at plasma mirror intensities. (a) The electron density profile for various intensities in Wcm^{-2} . Also shown is the comparison between the XPW and non XPW prepulse at (b) $4 \times 10^{15} \text{Wcm}^{-2}$ and (c) $4 \times 10^{16} \text{Wcm}^{-2}$

profile tells the complete story.

3.3 High Intensity Capabilities

One of the unique aspects of the HERCULES solid target experimental area is the high intensity at which experiments are conducted. The author is unaware of any publications as of this writing that are performed at intensities comparable to the HERCULES facility. Utilizing such a high intensity is no easy task, however. Two paths are available towards high intensity, one is simply increasing power, which linearly increases intensity; and the other is to decrease the focal diameter, which increases intensity quadratically. Aside from the differences in efficiency, increasing laser power often means an additional amplification stage which in turn requires substantial capital investment⁴. Reducing the focal diameter, however, can be a much more practical method of increasing intensity.

The focal spot, from Fraunhofer diffraction theory, is the Fourier transform of the input image, so a finite slit produces an intensity pattern that is a sinc function at the focal plane. Similarly, the fourier transform of a circular aperture (in this case, the finite diameter of the beam and the lens) is the Airy disk at the focal plane. The full width at half maximum (FWHM) of a diffraction limited spot size of a lens focusing a collimated beam is given by the 50% intensity point for the function of the Airy disk, or when $I_0(2\frac{J_1(ka \sin \theta)}{ka \sin \theta}) = 0.5I_0$, where k is the wave number, a is the collimated beam diameter, and θ is the angle of the incoming ray. This occurs when $ka \sin \theta \approx 1.162\dots$, so the equation for a FWHM spot in practical units is given by

$$d_{spot} \approx 2\frac{1.162\lambda F\#}{\pi} \approx 1.029\lambda N \quad (3.1)$$

⁴This is due to the fact that further amplification will mean increasing the beam diameter to avoid optical damage.

where $F_{\#}$ is the f-number, or the beam diameter divided by the focal length⁵. Thus, diffraction limited optics produce a focal diameter on the order of the f number over the wavelength. For the HERCULES system, 3.1 corresponds to $\sim 0.823F_{\#}$, so an F/1 optic should produce a spot with a 0.8 micron diameter while an F/3 optic will have a 2.4 micron focus FWHM⁶. These numbers are larger in practice, due to imperfections in the optics causing deviations from the diffraction limit.

A trade-off exists for utilizing smaller diameter foci. As the laser diameter is fixed, decreasing the f number requires a significantly sharper focus. This places a limit on the minimum f number for a variety of reasons. One is that the solid angle that the optic occupies increases as f number decreases, so that at some point it is impractical to position a target without obstructing the incoming beam. An additional complication is that such optics become prohibitively expensive. With the target closer to the focusing optic, irreparable damage can quickly occur, reducing reflectivity and focal quality. Perhaps the most difficult obstacle to overcome is target alignment. It is necessary to place the target at focus so that we maximize intensity and minimize transverse fields. The longitudinal extent that the beam is in focus is given by the Rayleigh Length,

$$L_{Rayleigh} = \frac{\pi(w_0/2)^2}{\lambda} \quad (3.2)$$

which is the length that the laser diameter increases from its minimum to $\sqrt{2}$ times the minimum, with w_0 being the beam waist. The confocal parameter is defined to be double this length. Due to the quadratic dependence on the focal diameter, the tolerances for positioning a target decrease significantly for longer focal lengths.

⁵This is a metric that defines how sharp or long a focal optic is. It is related to the numerical aperture of an optical system, where both define the amount of spatial frequencies available to the focusing optic. F number is used extensively in this thesis.

⁶There is a beautiful analogy with the time bandwidth product. As we increase the spatial frequencies (analogous to bandwidth), we decrease the spatial extent (analogous to the temporal width)

An F/1 optic will have a Rayleigh length of ~ 4 microns, while an F/3 will have a Rayleigh length of ~ 36 microns, making it much easier to place a target at focus.

These problems are not insurmountable, and great effort was made to utilize a sharp focusing optic. The lowest F number that still allowed for practical target motion was an F/1 OAP (Janos Technologies). Since plasma damage inevitably destroys the optical coating, relatively inexpensive diamond turned OAP optics were used. These were coated with a protected layer to maximize lifetime, and were replaced roughly every 300 shots. The quality of these optics could be as poor as several λ peak to valley. To compensate for these wavefront aberrations, a deformable mirror is placed directly before the OAP (Xinetics, 177 actuators). In situ monitoring of the focal spot is achieved by imaging the focal spot with an infinite corrected, achromatic microscope objective and the imaged focal spot was input to a Shack-Hartmann wavefront sensor (Imagine Optics HASO). The deformable mirror is a series of piezo-actuators fused to a thin, flexible optical plate. Adjacent actuators may lie at different places, introducing a path difference that compensates the surface wavefront aberrations in the OAP. To correct the wavefront, each actuator is moved in and out and the change in the wavefront as measured by the wavefront sensor is recorded. A computer program then solves the response necessary to flatten the wavefront. This forms a voltage matrix, which is gradually applied until the wavefront converges to a flat profile. The Strehl ratio, or the ratio of peak diffraction intensity of the measured beam compared to a perfect wavefront, is corrected to a value of > 0.9 , however beam pointing instabilities mean that the mean Strehl ratio is closer to 0.75.

The measured spot size after optimization is $1.20\mu m \pm 0.11$ FWHM. The excellent quality of the focal spot is demonstrated by Fig. 3.8, which shows little energy outside of the focal spot. The limiting factor for energy deposited in the focal spot is the roughness of the gold coating of the OAP, which can scatter a significant amount of light into large angles. A combination of a pinhole and a fast diode allows a

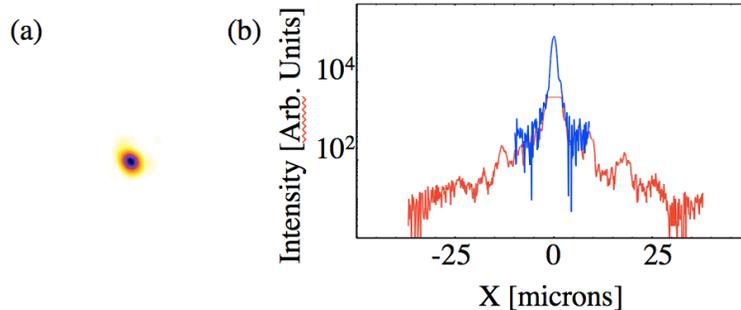


Figure 3.8: (a) CCD image of the focal spot. (b) Logarithmic line-out of the focal spot.

measurement of the scatter, so that there is 55 – 65% of the laser energy that is in the focal spot, depending on the quality of the OAP surface.

Positioning the target within the confocal parameter requires a target alignment system that is accurate on the micron scale. The large solid angle of the OAP does not allow for any specular light to be collected by a secondary imaging system, so a triangulation system was designed and installed enabling an accuracy along the laser axis of $> 2\mu m$. The triangulation beam was also imaged so that transverse positioning of microfabricated targets could be aligned with an accuracy of $\sim 10\mu m$.

3.4 Diagnostics

In order to capture as much information as possible about the interaction, many types of diagnostics are fielded on every experiment. Due to the vacuum environment, much of the experimental data collection takes place outside of the experimental chamber, so that the use of relay optics becomes extremely important. An invaluable tool is the charged couple device array (CCD). The high quantum efficiency and single shot readout allow for experiments to immediately obtain information and adapt the experiment as it progresses.

3.4.1 Optical Diagnostics

The generation of such intense, high contrast femtosecond laser pulses relies on many nonlinear processes, which require careful monitoring. For every shot several diagnostics were deployed to ensure that laser parameters were as expected. The diagnostics are positioned at various locations throughout the laser system. High reflectivity dielectric mirrors (reflectivity $> 99.95\%$) are used. The reflectivity curve is nearly constant across the bandwidth of the laser, so a low intensity diagnostic beam is able to be obtained simply from the transmission of the mirror. This “leak-through” beam preserves the laser wavefront and spectra, since the transmitted intensity is much lower⁷. Before the compressor, while the laser pulse is still propagating in air, the leak-through beam is sent into an optical spectrometer, as well as a pair of photodiodes. The optical spectrometer ensures that the central wavelength has not shifted as an experiment progresses, as well as recording the spectra from full power shots. The photodiodes consist of a large area integrating diode which is used to measure laser energy and a fast rise time diode to measure laser contrast before the plasma mirrors.

There is a second set of diodes positioned in the experimental area. A leak-through beam from the first mirror in the experimental chamber sends the beam out of the chamber where it is incident onto a similar pair of photodiodes that measure laser energy as well as the laser contrast in the chamber. This allows for a single shot measurement of both the reflectivity and the contrast improvement of the plasma mirror pair⁸. This leak-through pulse is also sent through an imaging system to take a measurement of the near field, far field, or both simultaneously, giving a measure of the wavefront for a full power shot after the plasma mirrors.

⁷The B integral for the transmission of a four inch diameter, 100 TW pulse at 45 degrees through 1 cm of glass is only ~ 0.16 .

⁸As the plasma mirror pair normally does not show a detected prepulse, it exists as a warning for plasma mirror malfunction.

As we have seen in Chapter II, the laser interaction can substantially alter the spectrum of the laser. To characterize the reflected pulse, a scatter screen is placed in the specular direction of the beam when the target is placed at 45 degree incident angle. The scattered light from this screen is imaged into several diagnostics. One of which is an optical spectrometer to measure the laser spectra after reflection, while the other is a CCD to image the screen. The CCD is often used with a band pass interference filter in place to focus on a particular wavelength range.

3.4.2 Particle Diagnostics

Electrons and ions are accelerated to high energies during the interactions. When a charged particle enters a magnetic field, it experiences the Lorentz force. For a uniform field that is perpendicular to the direction of particle motion, the motion is circular with a radius of gyration given by $\frac{\gamma m v_0}{q B_0}$. The velocity, and thus the energy of the charged particle can then be determined if a measurement of this gyroradius is made. Electrons are measured with a such a simple magnetic energy spectrometer. A pair of permanent magnets provides the magnetic field, and the entrance to the spectrometer is a lead slit with 1 mm diameter. A detector is placed along a defined plane, and the energy of the electron determines the location along the detector. Electrons with higher velocity will have an increasingly larger radius, so the dispersion is always greater for higher energies. The nonuniform dispersion increases measurement uncertainty at higher energy.

There are two types of detectors used commonly in experiments. Image plate is a detector that is highly sensitive to ionizing radiation. The image plate has embedded in it storage phosphors, where phosphor electrons are excited to a known metastable state, existing hours before decaying. The electron can be further stimulated into an even higher state having a fast decay time, through a process known as photostimulated luminescence. The image plate used here has BaFBr:Eu⁺² as a phosphor, and

has a resolution of $50\mu m$. The image plate system was Fujifilm. There is versatility with the use of image plate, since it can be cut to match a specific geometry much like film. However, the image plate must be kept away from room light to prevent any photostimulated luminescence to occur before the image plate is read, also much like film, however image plate is not as sensitive to visible light as film. For use in experiments, this limits its role as an integrated diagnostic.

For single shot experiments, a scintillating screen is often used instead (Kodak Lanex). Lanex uses Gd_2O_2S as the scintillating screen, which emits a photon at 550 nm when energetic radiation is incident on it [75]. This phosphor layer is only tens of microns thick and is bound to a polyester layer a few hundred microns thick for support. Electrons of the order of MeV energies will pass through the protective coating and plastic backing layer, and for energies higher than several MeV the response is nearly uniform [92]. The single shot nature of the detector implies that the signal will be much weaker than that of an integrating detector, but the value of an in situ electron response make it an invaluable resource.

For the experiments in this thesis, compact magnetic electron spectrometers were produced with 0.1 Tesla magnetic fields using Lanex as the detector. The Lanex was wrapped in aluminum foil (200 microns) to reduce background noise from low energy electrons and laser light. The Lanex screen was imaged to a CCD outside the chamber with dielectric mirrors that had a peak reflectivity around 532 nm, providing ample contrast between the green photons emitted by the Lanex and light from the laser or other interactions. Furthermore, a bandpass filter (Schott BG39) is used at the CCD to eliminate scattered laser light outside the chamber. Lanex can be placed at a variable distance from the slit, so that different energy ranges may be examined.

The most critical diagnostic for ion acceleration experiments is the Thomson Parabola ion spectrometer (TP). As opposed to the electron spectrometer, the existence of many different charge to mass combinations mean that to use a magnetic

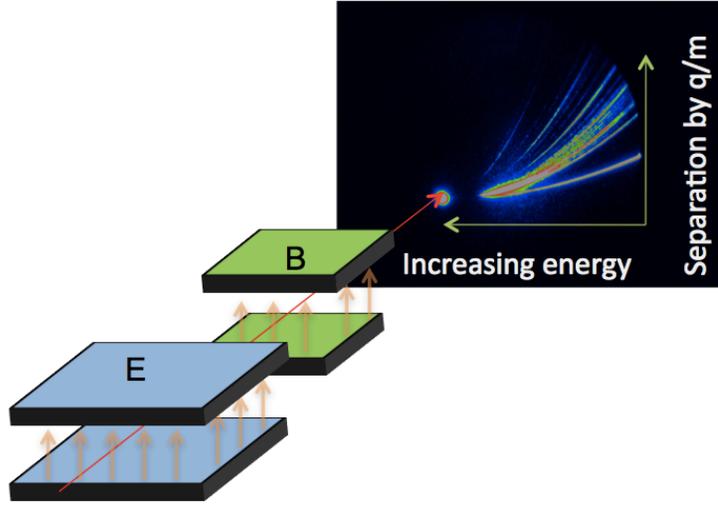


Figure 3.9: Schematic Diagram of a Thomson Parabola ion spectrometer. The particles are deflected with respect to energy due to the magnetic field, and are deflected by the charge to mass ratio by the electric field. X-rays and neutral atoms produce a zero order point for alignment.

spectrometer for ions they must be separated first. This is accomplished with an electric field, utilizing the other term in the Lorentz force ($q\vec{E}$). The electric field applies an acceleration that is dependent only on the charge to mass ratio. A small diameter pinhole is used to define the geometry, much like the slit in the electron spectrometer. Solving the Lorentz force equation for motion yields a dependence in the electric field direction with a dependence inversely proportional to velocity squared and a motion in the orthogonal direction with only a inverse velocity dependence. This means that the equipotential line for a particular charge to mass ratio will form a parabola on the detector plane. The expression for the parabola is given [138] by

$$y^2 = \frac{Ze_c B^2 L_{Mag}^2 \left(\frac{L_{Mag}}{2} + d_{Mag} \right)^2}{m_{ion} E L_{Elec} \left(\frac{L_{Elec}}{2} + d_{Elec} \right)} x \quad (3.3)$$

with Z as the charge state of the ion, L as the length of the electric (magnetic) field, and d as the drift distance between the back of the electric (magnetic) field and the detector plane. The energy of a particular parabola trace is given entirely

by the deflection orthogonal to the electric field. This is extremely useful for ions such as protons, since there is no other particle with a charge to mass ratio of 1. However, many ion species exist with nearly identical charge to mass ratios, making exact identification difficult, as is the case for silicon and nitrogen, or any fully ionized atom aside from hydrogen.

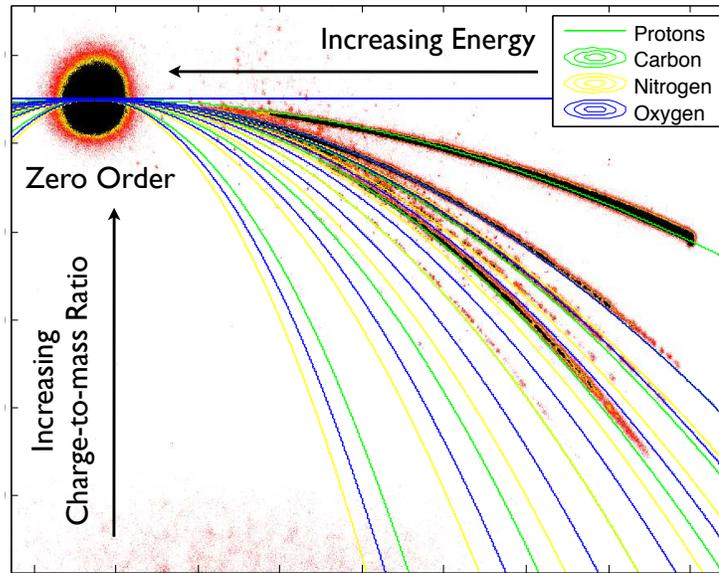


Figure 3.10: Thomson parabola trace with overlays from the analytical solution for particle motion for various atoms. The straight through is used as a reference.

For the TP used in the experiments in this experiment, a dipole magnet at either 0.32 or 0.64 Tesla was used. An electric field of 10-25 keV was applied on two parallel plates separated by 1 cm was placed afterwards. Varying the strength of the fields and the distance of the fields to the detector plane allowed for a variety of energy ranges to be detected. The uncertainty is greater for higher energies since the magnetic dispersion is less, similar to a magnetic electron spectrometer. For single shot operation the detector used is a microchannel plate (MCP). The MCP is a glass array of small diameter pores which act as electron multipliers. The array of pores are in a static electric field. Ionizing radiation impinging on one of the pores will begin an avalanche of electrons that will strike a phosphor plate upon exiting the

MCP. The radiation from the phosphor can then be imaged, giving spatially resolved information. The MCP used in the experimental setup has a pore diameter of 10 microns, and an active area of 3 inches (Photonis). Drawbacks to the MCP as a detector include limited dynamic range, and stringent vacuum requirements. The system in use is kept inside of a separate chamber and is differentially pumped. A large diameter plastic sheet with a pinhole provides the differential. The beam is then sent through a $200\ \mu\text{m}$ pinhole, and a lead collimator before entering the electric field. The trace is imaged by a CCD outside of the vacuum chamber. A typical trace can be seen in Fig. 3.10, where individual ions can be identified.

To measure an ion beam over a large area requires a different detector, since the MCP requires a stronger vacuum and image plate is covered with a protective plastic layer that blocks protons below several MeV. The nuclear track detector CR-39 provides a useful alternative [19]. Originally used as a plastic for eyewear, CR-39 has an advantage in that it is a very homogeneous plastic. When ions impact the plastic, it weakens bonds when energy is deposited. An etching solution (NaOH) is used to etch the plastic, and these damaged areas grow into macroscopic pits, allowing the impact to be observed. The high levels of homogeneity yield high resolutions with extremely high signal to noise ratios.

Part of the reason that CR-39 is able to be such an absolute reference is due to the physics of ion stopping. An ion moving at fast velocities ($\sim 100\ \text{MeV}$) is able to travel through solid matter for a distance relatively unimpeded as the stopping power is low (See Fig. 3.11 (a)). The electron cross section is low for high velocities. As the ion loses energy, the electron cross section increases dramatically, and a large rise in the stopping power occurs. The stopping power is so great the ion is fully stopped in a very small volume. The propagation of the ion experiences little scattering until then, so a very localized region exists where the majority of energy deposition occurs. This concentrated energy deposition is the advantage for radiation deposition in ion

radiotherapy discussed in Chapter I. This localized region is called the Bragg peak, and is dependent on the initial energy of the particle (Fig. 3.11 (b)).

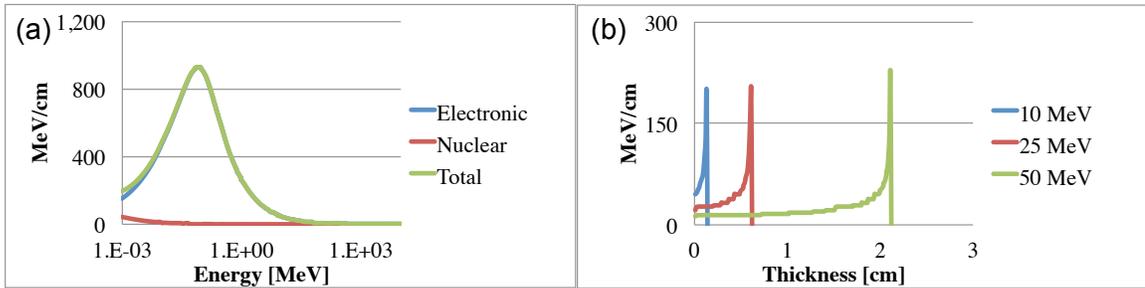


Figure 3.11: (a) Stopping power of a proton through liquid water. Note that the stopping power is almost entirely due to the electrons. (b) The energy loss of protons through water for several different initial energies. The point at which all remaining energy is abruptly lost is known as the Bragg peak.

With CR-39, a single proton can generate a track, yielding very high spatial information as well as an absolute number. This makes CR-39 extremely useful for the calibration of spectrometers such as the TP. It is also not sensitive to x-rays or electrons, making it a robust detector that can be placed in extreme environments. By exploiting the Bragg peak, energy information can be obtained as well. By layering foils of various thicknesses as shown in Fig. 3.12, the only protons able to strike the CR-39 must have a minimum energy to travel through the filter. With several energy bins a total spectra with absolute energy can be generated. Without the filters, divergence information can be found by observing the size of the beam.

3.4.3 X-Ray Diagnostics

There are a number of physical mechanisms of laser-plasma interaction capable of producing light across the entire band of x-rays. Two of the diagnostics are an integral piece of the target alignment system. While the triangulation system establishes a very precise relative position to align targets with, the very short Rayleigh length of the F/1 makes the overlap of the alignment beam to the main pulse very difficult,

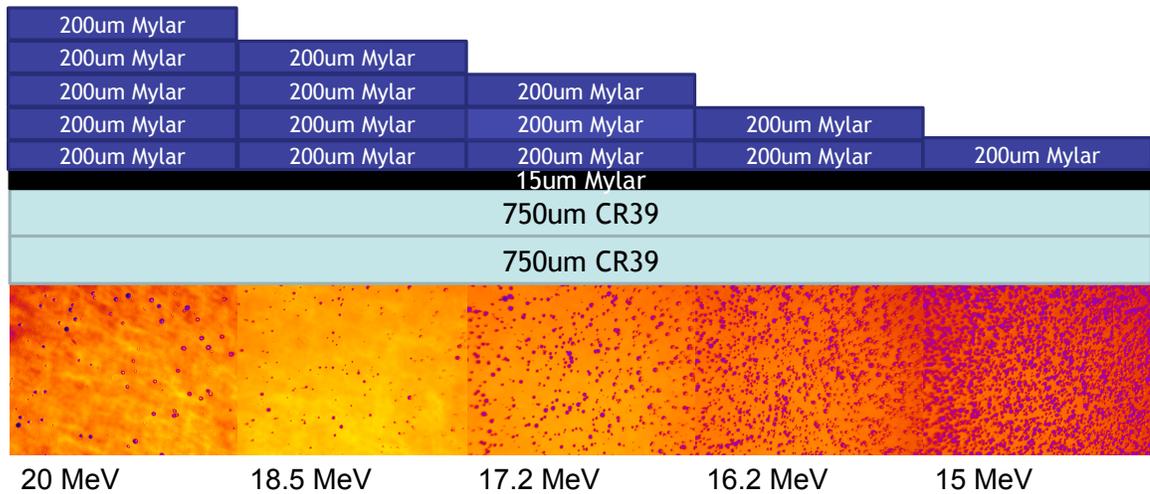


Figure 3.12: Diagram of CR-39 energy calibration. Foils are in strips along a piece of CR-39, allowing for divergence information in one axis and energy information in the other.

particularly once the chamber is under vacuum. If sufficient pulse cleaning is not present, the preplasma scale length can be large enough to shift the optimal focus position from the vacuum position. Thus, every experiment begins with a scan of the focus. As seen in Chapter II, the electron temperature is directly proportional to the intensity. The higher the electron temperature, the more Bremsstrahlung will occur in the target. Higher energy gamma rays from the interaction can be measured by a sodium iodine scintillator positioned outside of the shielding. The scintillator is attached to a photomultiplier tube (Hamamatsu) and is housed in a box of 10 cm thickness lead.

The other gamma ray detector is a PIN diode. This is a piece of semiconducting material that sandwiches a layer of intrinsic silicon between a P doped layer and an N doped layer. The diode is reversed biased and normally does not conduct electricity. When a photon is incident on the intrinsic region, it produces an electron hole pair which produces a current from the field produced by the bias. The PIN diode is set up experimentally with an unobstructed line of sight to the target, except for a 25 micron Be foil that serves to block laser light. A dipole magnet in front of the diode

sweeps high and low energy electrons to ensure that only x-rays are detected. For high contrast experiments the scanning of the target through the focus of the laser can provide a very sharp peak indicating the optimal intensity (Fig. 3.13).

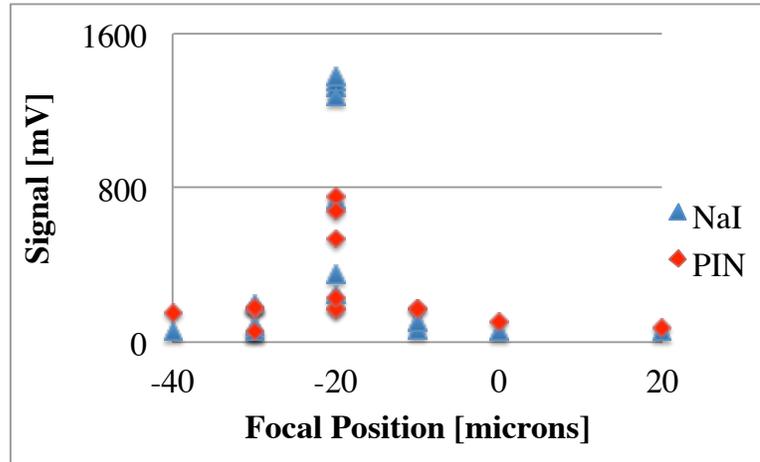


Figure 3.13: Focal scan of a 550 micron silicon target at high contrast. Signal is clearly peaked, showing the region of highest intensity.

Extreme Ultraviolet (EUV) light is much more difficult to detect. Every element has a strong absorption edge at the K or L edge throughout the entire region, and attenuation lengths are often on the order of a micron or less. Because of the strong absorption, manipulating EUV photons is very difficult. However, for a mirror that approaches a grazing incidence angle, efficient reflectivity is achievable. To characterize the EUV generated in the interaction, an imaging EUV spectrometer is used [100]. A variable line space grating (Hitachi) diffracts light onto an x-ray CCD (Andor). The grating is cylindrically curved, such that the interaction is focused onto the CCD. X-ray filters are placed to prevent laser light from striking the CCD. The detector takes a time integrated spectra of the interaction, so aside from EUV generated by HHG, light generated by longer lived processes such as plasma continuum emission and emission lines are also visible.

3.5 Computational Capabilities

Several simulation codes have been used in this thesis. In many cases, particular information of interest cannot be practically measured. To understand the underlying physics, experimentalists have relied increasingly on numerical modeling of an experiment. There are a number of models that each have their own strengths and weaknesses. The 1D hydrodynamic code HYADES is used to estimate the amount of preplasma formation due to hydrodynamic interaction of the long pulse prepulse. It does not, however, take into account multidimensional effects such as 3D plasma expansion due to small focal spots, instabilities, nor the high intensity absorption that may take place with the presence of short pulse prepulses.

Vlasov-Fokker-Planck (VFP) codes are able to solve the Vlasov equation for collisional plasmas. The VFP codes allow modeling of intense laser plasma interactions with no noise, due to the fact that it solves distribution functions rather than solving the n-body problem. Unfortunately, the high requirement to solve the Vlasov equation over the entire phase space causes extreme inefficiency, so that such codes are more suited for localized, fast time scale interactions. The VFP code IMPACTA is utilized for the study of short pulse prepulses, and is very useful for identifying the physical mechanism for the experiment presented in Chapter IV.

The workhorse for understanding the underlying physics of the short pulse laser plasma interaction is the particle-in-cell (PIC) code. With PIC, rather than model every individual ion and electron, macro-particles representing a charge density are used. The charge of the particles is mapped to a grid, with a resolution that resolves the Nyquist frequency of the dynamic of interest. The mapping in effect truncates the electric field of the particles, removing the collisions due to binary interactions. This provides a statistical solution of the Vlasov equation while requiring far less computations, making it a much more efficient calculation. However, there are still several critical limitations in the PIC code. It simulates a collisionless plasma, which

may not be accurate for electron transport through a solid target. Ionization is also not modeled⁹, and must be assumed at the beginning of the simulation. Perhaps the most distressing is the presence of numerical noise. The act of mapping particles to a grid introduces a small rounding error, and the force becomes non-conservative. As the simulation progresses, this leads to a self heating of the particles and introduces statistical noise. This can be mitigated by various methods, such as higher order mapping to the grid or the use of smoothing, as well as using a finer resolution grid. However, ultimately the noise will win out limiting the duration over which the interaction can be simulated. Short pulse interactions are thus particularly well suited for modeling with PIC codes.

The PIC code used for the work discussed in the following chapters is the OSIRIS code¹⁰ [43]. The code can be used in 1,2, or 3 spatial dimensions with all 3 dimensions of phase space. The code is parallelized for use on a computing cluster, so that a greater number of particles may be simulated. For example, a single computer may have 4 gigabytes of memory, and if a 32 bit number (single precision) is used to keep track of each of the 6 dimensions then ~ 20 million particles can be simulated, while a cluster can have significantly more memory available to it (32 GB per node are now common). To take advantage of the parallel processing capabilities, simulations are performed on the Center for Advanced Computing's Nyx cluster at University of Michigan. The high field science group has 192 nodes at the cluster, with over half a terabyte of memory and can transfer data between nodes at 10 gbit/sec, providing adequate computational power for 3D underdense interactions or 2D solid density interactions.

⁹In actuality, in the OSIRIS 2.0 framework, ionization *is* modeled, however, only for a single ionization state. This works well for low density hydrogen plasmas, but poorly for solid density multi-atomic species.

¹⁰Both OSIRIS 1.0 and 2.0 were used for this thesis work.

CHAPTER IV

Control of ion spectra

4.1 Introduction

Control of the ion spectra has been a long standing issue in laser based ion acceleration. Experimentally, proton and ion beams accelerated via TNSA have previously been observed with Boltzmann-like energy distributions [96, 2]. Spectral modification has been observed in experiments, however. The use of micro-structures on the rear surface of the target produced proton beams with an energy spread of 25 percent [118]. Another experiment used a thick, high atomic number foil that is heated to over 1,100 degrees Kelvin, such that the protons are evaporated off but the carbon remains in a state of graphite. The monolayers of carbon are accelerated in the TNSA field, and the result is a beam of carbon ions with an energy spread of 17 percent [54]. A form of energy selection is achieved by the use of a hollow cylinder that is placed in a second intense beam. The proton beam enters the cylinder as the beam is struck by the laser, and the sheath field that forms on the inside of the cylinder acts to focus the ion beam at a particular energy [128]. This has been demonstrated to produce a proton beam with an energy spread of only 3 percent. However, all of these approaches require targets or geometries that are not suitable for a high repetition rate system, and limit their usefulness in many applications.

Experimentally, radiation pressure driven shocks have also demonstrated narrow

energy spread spectra from gas targets [104], although this work was done with a CO_2 laser whose 10 micron λ_0 both reduces n_c and increases a_0 via $I_0\lambda^2$. This cannot be easily done in NIR short pulse experiments. And while recent simulation work suggests that with only modest increases of intensity, short pulse lasers may be able to accelerate protons with narrow energy spreads to several hundreds of MeV from ultra thin (~ 10 nm) targets [40, 114, 85, 13]; it will be shown in chapter V that there are significant physical limitations towards this approach.

The optimal technique for a high repetition system would not depend on complex target geometries, but rather simple foils that can be utilized on a tape drive, for instance. To fulfill this requirement, optical density shaping is an ideal solution. Previous simulation work has been done suggesting that secondary fields can strongly effect the ion acceleration mechanism. Two strong pulses arriving shortly after one another can cause electron pulses in the sheath field that can cause the formation of spectral peaks in multiple sheath target acceleration [113]. This has been demonstrated in both PIC and Vlasov code, but not in any experiments. Another method involves changing the contaminant layer composition. A 10 nm proton layer that is unperturbed is shown to produce the expected Boltzmann-like spectra, while a 100 nm proton layer that has 5 percent of its original density is shown to exhibit quasi-monoenergetic energy spectra [112].

Presented in this chapter is an experiment that lies in between the previous simulated scheme. A prepulse is used to optically shape the density profile in a manner unique to earlier work. In particular, a short pulse is used in conjunction with a cleaned interaction pulse to preferentially shape the proton density. The short pulse prepulse with low intensity and with long delay time between the main pulse cannot cause multiple sheath target acceleration, instead it allows the proton density to be shaped more along the lines of the latter mechanism. In this chapter, it will be demonstrated that if the high intensity interaction is preceded by a much less intense

short pulse prepulse 33 ps prior to the main pulse, the proton energy spectrum becomes narrowed. This is due to keV electrons generated from this prepulse that are able to collisionally ionize the rear-side contaminant layer, causing expansion and a reduction in density. From this picosecond scale window, only the ions with a high charge-to-mass ratio ($\frac{q}{m}$) are able to move significantly, so that the lightest ions in the contaminant layer preferentially expand while the target remains mostly unperturbed, in contrast to the hydrodynamic expansion that occurs from ASE prepulse interactions. Simulations are made of the interaction to demonstrate the effects of such a prepulse.

4.2 Experimental Setup

Double plasma mirrors were employed for the experiment, with an anti-reflection coating of 0.5% at 810 nm. This produces an ASE intensity contrast of less than 10^{-13} on target. The laser energy was 1.1 ± 0.1 J on the target, which corresponds to an on-target intensity of 2×10^{21} Wcm $^{-2}$ with a normalized vector-potential of $a_0 = 30$. The targets used were free standing silicon nitride (SiN) membranes from 30 to 200 nm and Mylar foils ($C_{10}H_8O_4$) from 1 to 13 μ m. Both foils are dielectrics which have a similar damage threshold. The targets were positioned at the laser focus at an angle of incidence of 45° and at normal incidence. The beam was P-polarized for the oblique incidence angle shots. The TP was placed in the target normal direction for each geometry.

4.2.1 Prepulse introduction

Deliberate introduction of a short prepulse can be achieved simply by introducing a post-pulse prior amplification. Nonlinear interactions between the post-pulse and the main pulse during amplification resulted in a prepulse after compression [82]. This nonlinearly generated prepulse will henceforth be simply referred to as the *prepulse*.

When the prepulse is not present the term *clean pulse* will be used. The prepulse arrived 33 ps prior to the main pulse as measured by a streak camera. The on-target peak intensity of this prepulse is measured to be $3(\pm 2) \times 10^{16} \text{ Wcm}^{-2}$ with a duration equal to that of the main pulse. Images of the laser beam profile after the plasma mirror indicate that this prepulse generates some plasma on the surface of the first plasma mirror, but the resulting focal spot is not measurably degraded (See Fig. 4.1). While other short pulse prepulses exist [23], the intensity of any other prepulse after the plasma mirrors is below the damage threshold of the targets used and does not result in preplasma formation.

Experiments have been done previously with a secondary laser to produce a preplasma [62]. However, in many cases the preplasma is formed by the rising pedestal of the laser pulse at the ~ 100 picosecond level or from the ASE at the nanosecond level. Long pulse interactions such as these cause preplasma formation due to heating of the focal area and a resultant hydrodynamic expansion. Because the plasma is able to achieve equilibrium during this time, the entire plasma is able to move collectively. In addition, the scale lengths from the nanosecond pulses are typically many microns in length, due to the long expansion time.

In contrast, a short pulse laser will cause a simple hydrodynamic expansion. The energy in a moderate intensity short pulse is very small, and since the pulse duration is so small the ion motion during the interaction is negligible. The result is that the electrons are accelerated to a high temperature ($\sim \text{keV}$) while the ions initially are not. The heated electrons are able to form sheath fields for a limited duration, and will preferentially accelerate the higher charge-to-mass ions. There is then a change in density dependent on the ion species, a fact that will be shown to be critical for the mechanism described.

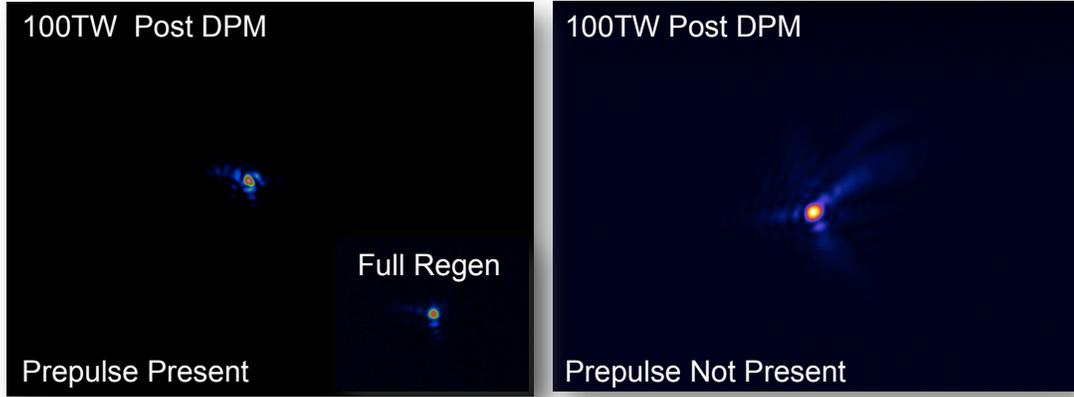


Figure 4.1: Beam diagnostic images of the laser far field after plasma mirrors. No difference in intensity is observed for prepulse being present compared to regen amplification or at full power without prepulse.

4.3 Ion Spectra Results

The data presented in the following will focus on the 45 degree data set in order to provide a proper comparison. Normal incidence ion acceleration data will be presented in the following chapter. During the experiment, many light ions were observed, including carbon, nitrogen, oxygen, and of course protons. Proton and carbon spectra are characterized in this experiment, due to their dominance in the spectra and ease of identification. The clean pulse case expectedly showed the expected Boltzmann-like spectra, however, characteristic in some shots of clean pulse spectra was a high energy peak in the otherwise Boltzmann-like energy spectrum (Fig. 4.2 (a)). As the target thickness is decreased, the maximum observed proton energy increased from $6.7 (\pm 1.3)$ MeV at $1 \mu\text{m}$ thickness to $9.5 (\pm 3.3)$ MeV at 30 nm target thickness (Fig. 4.3). A trend is observed such that thinner targets produce higher energies, as the electron density in the sheath increases and can provide stronger accelerating fields, consistent with previous results [62]. The other ions display a similar trend in their maximum energy, with an energy per nucleon that has a maximum of up to ~ 3 MeV, much less than the protons and also consistent with previously reported results.

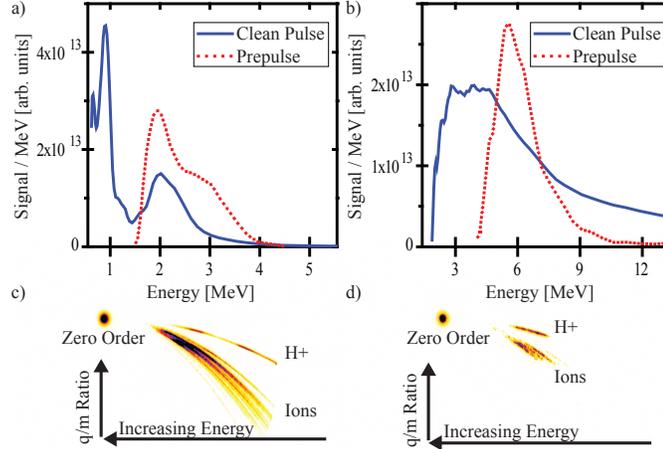


Figure 4.2: Energy spectra for prepulse (50 nm Si_3N_4) and clean pulse (30 nm Si_3N_4) for (a) Protons and (b) Carbon 4+. The sharp drop on the clean pulse case is due to the edge of the detector. The raw traces for these spectra are also shown for (c) clean pulse and (d) prepulse.

When the prepulse is introduced at the 45 degree incidence angle, a drastic change is observed in the proton energy spectra. The low energy protons are below the detection threshold of the TP (Fig. 4.2 (d)). Although an MCP detector possesses a limited dynamic range, there was not even a single detectable count above the background measured in this region. Perhaps even more interesting is that for the 50 nm Si_3N_4 targets, the light ions also exhibit the narrow energy spread feature. The minimum detectable energy for protons on the TP was 0.5 MeV. The FWHM of the proton spectral peak varies minimally, although the maximum energy of the spectra is dependent on target thickness (Fig. 4.3 (b)). It is also observed that the energy spread ($\frac{\Delta E}{E}$) varies from shot to shot between 25 and 60%. At target thickness of 1 μm both prepulse and clean pulse produce similar energy protons, but for the submicron targets peak proton energies fail to increase in the prepulse case (Fig. 4.3 (c)), indicating that the prepulse is likely causing significant deformation of the bulk target before the arrival of the main pulse. When the target is defocused or at normal incidence, a broad energy spectrum returns, suggesting that this phenomena

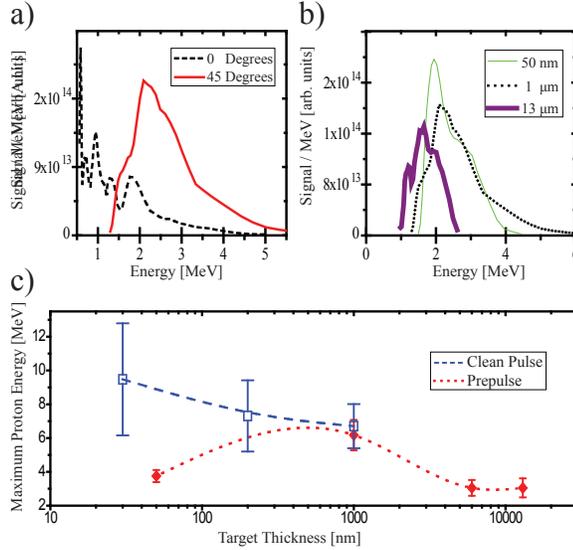


Figure 4.3: (Color online) (a) Proton spectra for prepulse case for 0 and 45 degrees incidence for 1 μm Mylar targets. (b) Prepulse proton spectra for 3 target thicknesses. (c) Maximum proton energy for prepulse and clean pulse case. Lines are shown for visual aid only.

is dependent on intensity and the target being at an oblique angle (Fig. 4.3 (a)). Laser transmission remained below background for all target thicknesses, indicating that targets were above critical density for the main pulse interaction. CR-39 track detectors were used to measure the divergence of the proton beams produced. In both cases the divergence was measured to be below 250 mrad for 1 MeV and below 75 mrad for 5 MeV protons. CR-39 with step filters was also used to measure the maximum energy, although these detectors integrated many shots and did not show a clear mono-energetic signature.

The quasi-monoenergetic feature in the proton energy spectra is highly reproducible, for example being observed in 71 out of 95 shots taken over several shot days for all target thicknesses when the prepulse is present. 6 successive shots taken at 1 micron thickness Mylar are shown in Figure 4.4. The mono-energetic feature could reproducibly be removed and reintroduced simply by defocusing the target and returning it to best focus. Since the effect is observed to be the same in both the non-

hydrogen containing Si_3N_4 targets as well as Mylar, the accelerated ions are thought to be generated entirely from contaminants on the surface of the target rather than from the bulk target itself. When the experiment is performed for normal incidence, the effect is no longer observed. This is consistent with the absorption processes being stronger at oblique incidence angles.



Figure 4.4: Raw TP traces of 6 successive shots on $1\mu\text{m}$ Mylar with prepulse present. The proton spectra is clearly displays quasi-monoenergetic features in every shot.

4.3.1 Numerical Simulations

Numerical modeling is difficult due to the 33 ps timescale between pulses, the high density, and the fact that a hydrodynamic simulation will not correctly model hot electron transport. A PIC simulation of the experimental conditions would not be able to run for the entire 33 ps duration due to numerical heating. To counteract this issue, a hybrid approach was used instead. Initially, the prepulse interaction is modeled in a PIC simulation to determine the initial electron distribution function. The electrons will then be used as an input in a VFP code which will determine

the effects of the hot electrons on the density profile. The VFP simulation has no numerical noise, so it can be run for the 33 ps necessary. Finally, the density function obtained from the VFP code will provide the initial conditions for the main interaction simulation, which will be done again in a PIC simulation.

For a prepulse with intensity I_0 of $> 10^{16}$ Wcm $^{-2}$, a combination of inverse bremsstrahlung and Brunel heating [12] will create a localized plasma and a population of hot electrons with a mean kinetic energy of $T_h = 3.6I_{16}\lambda_\mu^2 \approx 6$ keV [49], which is also validated with particle-in-cell (PIC) simulations using the OSIRIS code [43]. To estimate the field strength on the rear of the target for the 13 μ m thick Mylar case, we used an implicit 2D Vlasov-Fokker-Planck code [125, 64] modified to include a collisional Saha ionization model, and a non-relativistic Bethe collisional energy loss formula for the un-ionized material to numerically model the electron transport and ionization dynamics in the target. The anticipated electric field is expected to be too weak for field ionization to have a significant impact, so it was not included in the code. Ionization of the target at this intensity may also be affected by radiative energy transfer [31]. Suprathermal electrons from the tail of the front surface plasma propagate through the target, and set up a sheath electric field of strength $E_0 \sim 10^8$ Vm $^{-1}$ on the rear surface, indeed several orders too low to cause field ionization. These simulations were performed at the largest target thickness to show that the density modification is capable of taking place for all targets, as the weak sheath field will only increase in thickness as the target thickness decreases.

Although the electron distribution function at the rear is a two temperature distribution, rather than a single temperature commonly used in self-similar expansion models, we can use an average over the hot and cold populations to calculate the sound speed [105]. Then in a single temperature expansion model, we can estimate the plasma scale length λ_s at 33 ps via $\lambda_s \approx 2c_s t$ [96], where $c_s^2 = Zk_B\langle T_e \rangle/m_i$, and $\langle T_e \rangle = (n_{eh}T_{eh} + n_{ec}T_{ec})/n_e$ with the subscripts referring to hot and cold electrons.

This gives an exponential profile with a scale length of the order 100 nm using the temperature and density outputs from the 2D VFP simulation, although we expect this to be an upper limit. Protons will have a much longer scale length than the other ions due to their much higher $\frac{q}{m}$.

For PIC simulations of the main pulse interaction, a 1.2 μm fully ionized carbon target with density of 100 n_{crit} was used with front and rear-side proton layers. For simplicity, the scale lengths are linear ramps, with the density referring to the maximum density of the ramp with total integrated density constant and the thickness as the base of the ramp from the bulk target. A 45° p-polarized Gaussian laser pulse with 35 fs FWHM duration, 1.2 μm waist and a field strength parameter of $a_0 = 30$ was focused onto a target with a front-side proton scale length of 300 nm. The cell size was 2.55 nm by 3.8 nm, or $\lambda/315$. 128 particles per cell were used for the proton layer, with 16 particles used in all other cells. The proton layer had more particles in the acceleration direction for adequate statistics in the dimension that experiences the most motion.

4.4 Discussion

The scale length of rear surface plasma for the prepulse case is 175 nm and has a proton density of 0.3 n_{crit} , while for the clean pulse the scale length is 2 nm and the maximum density is 60 n_{crit} . In the former case, the low rear-side proton density results in minimal electric field screening due to the substantially longer Debye length. Thus the entire proton layer is accelerated as a whole, such that all protons experience the same acceleration force. The paramount difference is that the sheath field strength slowly changes strength. In the clean pulse case, the protons on the outside of the target gain the most energy, while protons deeper in the layer experience a weaker field later in time. Contrast this with the prepulse case, where the protons experience the same acceleration field until they exit the sheath. In fact, protons closest to the target

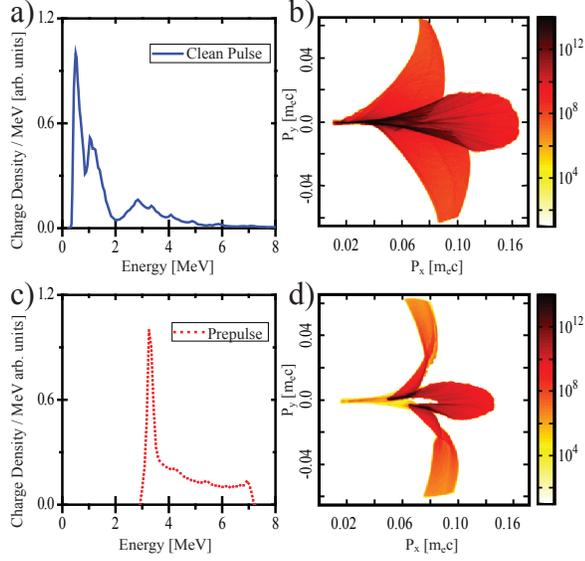


Figure 4.5: PIC simulation results at 202 fs of proton energy spectra for clean pulse (a) and prepulse (c) for 1 μm carbon target at target normal ($p_y \approx 0$) with charge density individually normalized to 1 for comparison. Proton phase space P_x v. P_y are also shown for clean pulse (b) and prepulse (d) in units of normalized momentum. *Note that the color scale is logarithmic.*

will be in the accelerating field slightly longer, thus having higher energies. This is evident in the phase space plots of the rear protons, which show a narrow momentum spread (Fig. 4.5 (c)), and also in the proton density, where protons closest to the target eventually overlap the ion front (Fig. 4.6). The density profiles of the rearside proton layer also show direct evidence of the difference in the field shielding, the protons closest to the focal region have surpassed the protons that were originally on the outside of the proton layer (Fig. 4.6). The protons possessing zero tangential velocity and thus those moving in target normal have a quasi-monoenergetic spectrum, with energies ranging from 3-7.2 MeV. When a detector is placed at this angle with a small solid angle, it will select this monoenergetic spectra. In the simulation, at angles other than directly at target normal the spectrum shows increased energy spread.

In the clean pulse PIC simulation, the rear-side protons initially move as a layer, but spread out as they travel. In this case, the sheath field is time varying due to pro-

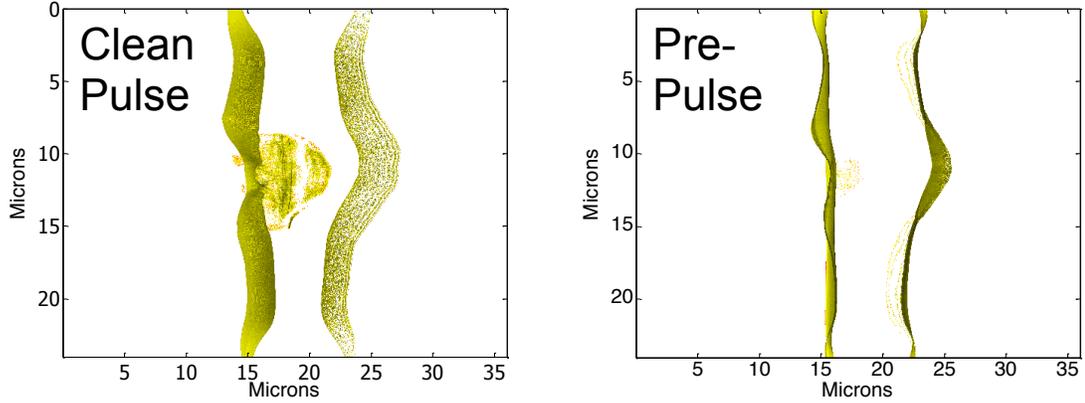


Figure 4.6: PIC simulations at 202 fs of proton density profile for clean pulse and prepulse.

ton screening, in contrast to the prepulse case. Since the contaminant layer is thicker than the cold Debye length (≈ 1 nm), protons in the layer can experience different forces. In this case the protons closest to the target experience the least acceleration, and provide the low energy component of the spectrum. The spectrum also displays a peaked structure similar to that observed experimentally (Fig. 4.5 (a)) and also shows higher maximum energy than the prepulse case. As the simulated target is $1.2 \mu\text{m}$ in thickness, this peak is likely is an artifact of a thin proton layer undergoing rapid acceleration, making it an experimental cue for short pulse experiments that high contrast has been achieved.

4.4.1 Implications for Ion Acceleration

The experiment performed provides a means of generating proton beams with energies similar to and energy spreads on par with the previous experiments involving complex targets or complicated target manipulation. While the energy spreads and maximum energies still are not high enough for many applications, the method drastically reduces the technical requirements for generating a proton beam with desirable qualities. The targets used are thick enough to be employed in a tape drive. A

system involving a high-repetition rate ion accelerator may be used as a front end to an RF linear accelerator to provide a low emittance proton accelerator. It should also be pointed out that the parameters of the prepulse were not in any way optimized for energy spread. The experiment used a fixed delay and fixed prepulse intensity. Additional work is necessary to understand if the prepulse can further reduce the energy spread of the proton beam.

There is a major implication of the work here that is important for experiments that are performed on ion acceleration in general. The targets used were many microns in thickness, and yet a means of generating a narrow energy spread exists. This cannot possibly be a proton beam generated by RPA. In order to be at optimal conditions for RPA for even a 1 micron target would require a laser with an a_0 of over 300, far higher of what is used for the experiment. And this effect is observed for target thicknesses an order of magnitude larger.

The clean pulse case also shows high energy bump-on-tail distributions at micron thicknesses. Clearly, the presence of a quasi-monoenergetic peak or even a peak on the spectra is *not* a sufficient signature of RPA, but rather a signature of a high contrast, high intensity experiment. This is a critical distinction in understanding the results of an experiment. In the next chapter, the experiments purpose was to generate ion beams accelerated by RPA. The results indeed showed a spectra with a high energy bump, but critical thought is needed to justify such a claim to ensure the correct acceleration mechanism.

4.4.2 Monoenergetic Ion Acceleration

An unexpected surprise in the experiment was the generation of quasi-monoenergetic ion beams in addition to the proton beams. While an exciting breakthrough, the lower charge to mass made it difficult to differentially increase the density profile of the light ions compared to the bulk. Because of this, only with the thinnest

targets where the prepulse sheath field is the strongest were we able to generate the narrow energy spread ion beams.

However, a high atomic number foil with a stronger intensity short pulse prepulse should be able to reproduce the mechanism described in this chapter. Since there was no available control over the prepulse intensity in this experiment, another approach was pursued. Rather than try to accelerate the light ions in the inherent contaminant layer, foils with a “painted” contaminant layer were used instead [139]. 13 micron Mylar targets were coated with a solution of deuterated polystyrene in a solvent on the surfaces of the foil. After the solvent evaporated, approximately 1 micron of the deuterated polystyrene remained, although significant hydrocarbon contaminants remain from the solvent, as well as the expected contaminants that are present on all targets. However, the deuterons have only a single ionization state, and therefore should expand more for the thick targets than the lower charge-to-mass ratio light ions if not fully ionized.

Unfortunately, detecting deuterons is difficult due to the fact that the charge to mass ratio is identical to practically any fully ionized light ion. Thus the TP cannot distinguish the deuteron ions from C^{6+} . CR-39 can be used to distinguish the ions based on the pit size, however, the use of a track detector limits the experiment to a single shot. A compromise is to shoot a thicker foil where there is not a significant amount of carbon accelerated, and so only 13 micron Mylar is used to observe the deuteron spectrum.

Unfortunately, the protons are still very dominant and remove much of the energy from the sheath. The resultant deuteron energy spectra is thus very weak compared to that of the protons. However, the low energies of the ions means that the traces on the TP are well isolated on the detector and the weak signal can be captured. A weak deuteron spectra is observed, with a strong quasi-monoenergetic peak as shown in figure 4.7. Although the maximum energy of the deuteron remains low, this

method may be applied to thinner targets to produce a narrow energy spread deuteron beam with higher energies. Depositing a layer of heavy water (D_2O) on the target cryogenically may allow this technique to preferentially accelerate the deuterons [97], so that a much stronger beam may be generated. The next step for this experiment is to use the deuterons to produce neutrons via a pitcher-catcher geometry [29]. This can experimentally determine if the energy spectra of the deuterons can successfully be transmitted to the neutron beam.

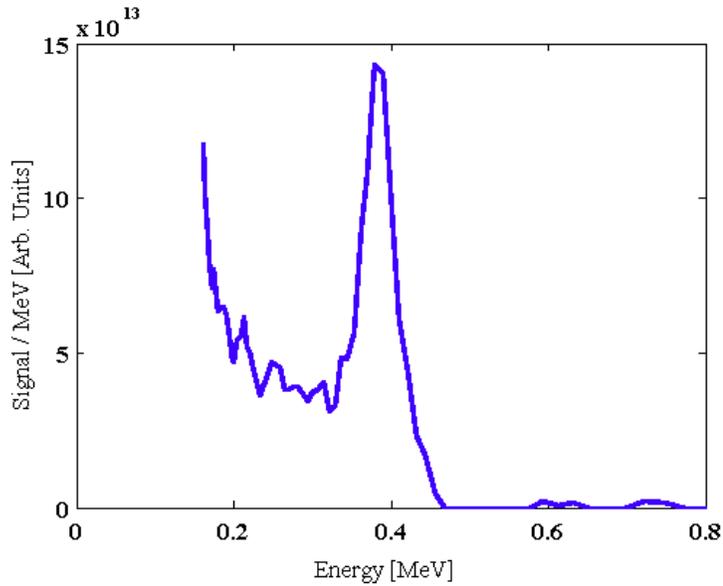


Figure 4.7: Deuteron energy spectra from $13 \mu\text{m}$ Mylar target with prepulse present.

4.5 Conclusions

In conclusion, control of the spectral shape of the proton and ion beams has been demonstrated. This was attainable due to the introduction of a high contrast short pulse prepulse 33 ps prior to a high intensity laser interaction and without prior target manipulation. As opposed to poor contrast experiments, the prepulse is able to shape the density of the contaminant layer without significantly affecting the bulk target. Proton beams with maximum energy of up to 6.2 MeV were produced

with as low as 30 % energy spread and a suppressed dark current of low energy ions. Simulations were performed at high resolution for conditions matching the experiment, reproducing the spectral shaping that is observed experimentally and providing insight into the acceleration mechanisms that produced the observed narrow spectral features. The experiment was performed with a fixed prepulse delay, which limited the target thickness, but this delay could potentially be optimized for different applications.

CHAPTER V

Polarization effects on thin targets

5.1 Introduction

Some of the most promising applications of laser driven ion accelerators, such as ion therapy [14, 45, 88], rely on proton or ion beams accelerated to several hundreds of MeV per nucleon with a narrow energy spread. As discussed, TNSA has demonstrated proton beams with energies greater than 60 MeV, yet with energy spreads of 100% [52]. At lower energies, several groups have demonstrated control over the proton energy spread by using energy selection [128], complex target preparation [54, 118], optical density shaping [32], and by driving ion soliton waves [60]. These schemes produced modest energy spreads, but do not present a practical means of increasing the maximum energy.

The use of TNSA is problematic, since the maximum energy is also where the ion number is lowest. Even if the maximum energy was increased to therapeutic levels ($\sim 200 - 300 \text{ MeV}$), the spectrum is still Boltzmann-like and the number of protons available for use is small. For example, a 10 MeV temperature proton beam accelerated from a 2 nm thick, 100 micron radius¹ produces less than 2×10^6 protons per MeV. This is far from sufficient compared to the roughly 10^{10} protons per second required for a proton therapy system [15]. Obviously, a fundamentally different

¹A total proton number of $\sim 2 \times 10^{12}$, assuming the protons are entirely from a water layer.

approach is required to make laser based ion acceleration useful for applications such as hadron therapy.

The recent simulation results of RPA [114], Directed Coulomb Explosion [13] and Breakout Afterburner [145] are thus extremely exciting for applications. In particular, RPA is ideally suited for the high repetition rate experiments since the intensities [143] and targets required are already available. Recent experimental work investigating RPA has been performed, although the success has been mixed. An experiment with a 10 micron laser was used to generate very narrow energy spread proton beams from gas jets, although the maximum proton energy was in the single digit MeV's [104]. NIR experiments were performed at intensities of $\sim 10^{19}\text{Wcm}^{-2}$, and although a peak was observed in the carbon spectra for circular polarization, other signatures of RPA were not present [56]. Specifically, the proton spectra was Boltzmann-like for both polarizations, and the optimal target thickness was thinner than the skin depth. It seemed that there was a problem in the experiment that prevented the RPA regime from being reached, and the hope was that the feature found could be stabilized by moving to intensities of 10^{21}Wcm^{-2} , a regime that the HERCULES facility is well suited to explore.

5.1.1 Light-sail Radiation Pressure Acceleration

In RPA, circular polarization may inhibit the transformation of laser energy into thermal electrons, since $\mathbf{j} \times \mathbf{B}$ heating is absent, and consequently TNSA is suppressed. Momentum is imparted by the laser to the target material, either by the laser acting as a piston on a semi-infinite target (hole-boring) [40], or by the laser accelerating the plasma as an accelerating mirror (light sail). In light-sail RPA, the entire focal volume is accelerated to the same momentum, producing narrow energy spread ions. In this model, ion energies are optimized when the foil thickness is $L \approx \frac{a_0}{\pi} \frac{n_{crit}}{n_e} \lambda$, where a_0 is the normalized field strength, λ is the laser wavelength and $\frac{n_{crit}}{n_e}$ is the ratio of

critical density to electron density. For $a_0 = 20$ at solid density the optimal thickness is calculated to be 15 nm [142]. However, many simulations have been performed in 1D, where no transverse effects exist. Those performed in 2D use parameters that minimize transverse spatial gradients [114, 84, 142].

In the RPA mechanism, suppression of electron heating will result in efficient energy transfer to the target ions. In this chapter, however, it will be shown that for current ultra-short pulse laser systems ($E_p < 10J$) RPA is not practically attainable since as the target thickness decreases, electron heating occurs rather than RPA even for circular polarization. This results in proton and carbon beams with exponential energy distributions similar to linear polarization under identical conditions. PIC simulations of the interaction demonstrate that rapid deformation of the thin target such that the laser field is not perpendicular to the surface normal results in efficient electron heating via a Brunel-like mechanism. For thicker targets where RPA is ineffective, target deformation is minimal within the pulse duration, resulting in no TNSA with the circular polarized pulse, consistent with the experimental results.

5.2 Experimental Setup

The plasma mirrors used in this experiment reflected less than 0.15% of S polarized light at 810 nm per plasma mirror, while possessing a measured reflectivity of 65%–70% at high intensity. This produces a ns-level ASE contrast of $< 10^{-15}$. This contrast improvement should prevent preplasma formation until 1 ps before the main pulse interaction, so that the density profiles remain extremely sharp. After the plasma mirrors, a mica $\frac{\lambda}{4}$ waveplate changes the polarization (between linear and circular). Beam profile monitors recorded the near and far field patterns of the beam after the waveplate to verify focal spot quality, and to confirm that the waveplate did not noticeably increase the pulse length due to dispersive effects. The laser delivered 1.5 (± 0.2) joules to the target with 55% of the energy in a 1.2 μm FWHM focal spot

via an $f/1$ off-axis parabolic mirror (OAP). This results in an on-target intensity of $2 \times 10^{21} \text{Wcm}^{-2}$ ($a_0 = 30$).

The targets used in the experiment were free standing SiN membranes with thicknesses of 30–100 nm, and 1 μm Mylar ($C_{10}H_8O_4$) foils. The targets were positioned at the laser focus at normal incidence. The experiment was performed with a linearly polarized beam, and with a right-hand circular polarized beam that possessed the same focal quality albeit with $\sim 10\%$ less total energy due to the Fresnel reflections of the waveplate. To eliminate polarization changing effects from the dielectric mirrors, the waveplate was adjusted such that the polarization at focus was circular. This adjustment, performed prior to the experiment using the regenerative amplifier, was done by using a separate quarter waveplate and a polarizer positioned in front of a photodiode that had been placed at the focus.

A transmitted light screen was also placed behind the target, but post-pulses and scattered light reduced the sensitivity of the diagnostic. Only transmitted light with total energy greater than 10% of the unobstructed beam could be detected. Experiments were also performed at a 45 degree incidence angle to measure absorption. As the reflected beam cannot be imaged well with the OAP and deformable mirror in place, an oblique incidence angle is necessary. Of course, at these non-normal incidence angles, circular polarization will absorb much more. To emulate normal incidence, S polarization is used as the absorption is minimized at oblique incidence angles.

These experiments used a half waveplate rather than a quarter waveplate so that the polarization was either S or P on target. Similarly, the S polarized beam had $\sim 10\%$ less energy due to back reflections and was aligned in a manner similar to the quarter waveplate. A screen was placed in the specular direction to image the reflected beam profile. Two additional targets were used for this experiment, a silicon wafer and an optical fused silica window to examine reflectivity changes for differing

damage thresholds. An imaging system imaged the screen to an optical spectrometer (Jobin Yvon MicroHR) and to a 12-bit CCD camera (Photometric Coolsnap). The CCD selected the fundamental by using an 800 nm interference bandpass filter with a 50 nm bandwidth. A diagram of this setup is shown in figure 5.1.

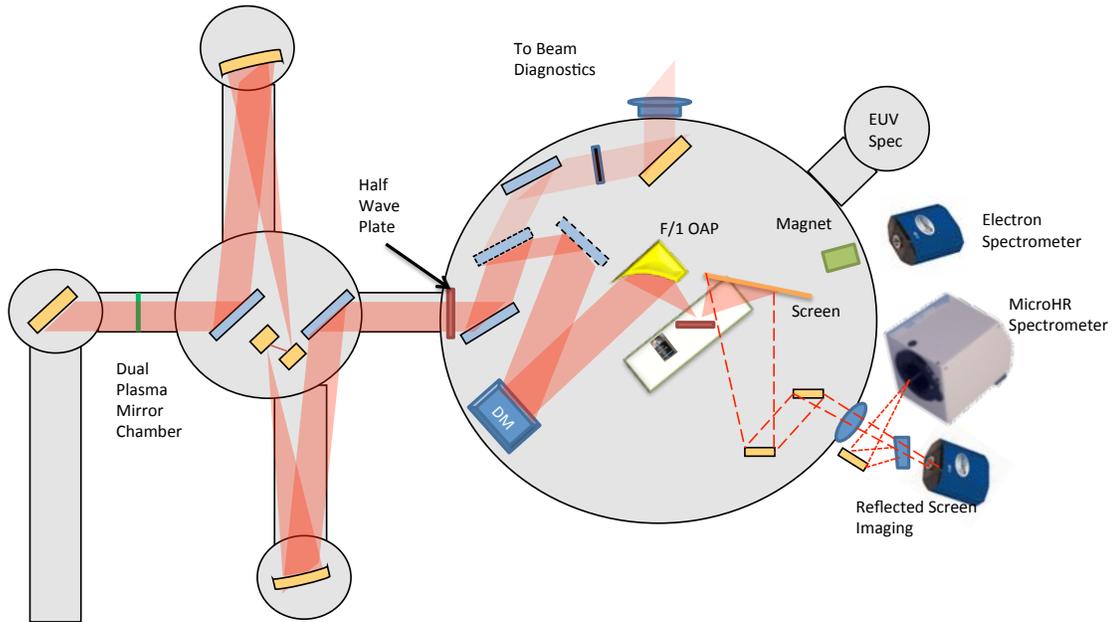


Figure 5.1: Schematic Diagram of experimental setup for absorption measurements.

5.3 Normal Incidence Results

With linear polarization, all targets produced an exponential energy distribution for both proton and carbon beams. For 30 nm SiN, linear polarization produced protons with an average maximum energy of ≈ 13 MeV (Fig. 5.2 (c)). Several shots were taken for each condition. The smaller dispersion and higher noise in the spectra at higher energies increase the error bars for these thinnest targets. In several shots the spectra displayed some modulated structure, similar to what was observed in the previous chapter and is to be expected. The average maximum energy of the protons and carbon ions increases slightly as target thickness is decreased (Fig. 5.2 (c)).

When the quarter waveplate was inserted (i.e., circular polarization), the maxi-

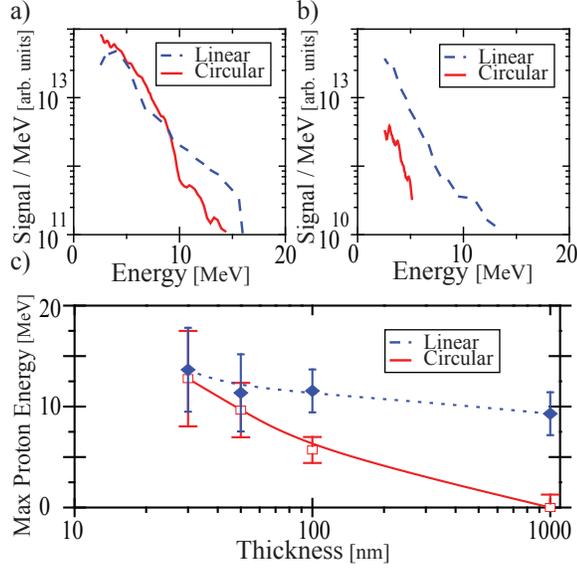


Figure 5.2: Proton energy spectra for both right-hand circular and linearly polarized laser pulse interactions for a) 30 nm and b) 100 nm thickness Si_3N_4 targets. Maximum proton energy vs. target thickness is also shown (c) with lines shown as visual aid only.

maximum proton energy was below the spectral range of the TP for the case of the $1\mu\text{m}$ Mylar targets. The ion signal consisted of single hit spectra in the low charge states of carbon. For these experiments, a stronger magnet was used in the TP as opposed to the previous experiments, and the threshold for detection was now 2.6 MeV as opposed to 0.5 MeV. There was also no detectable electron signal, significant since the magnetic spectrometer was designed for operation in the 100 keV to 3 MeV range. For the SiN targets, the proton maximum energies was low for the 100 nm target and then subsequently increased rapidly as the thickness decreases. For 100 nm targets, the maximum energy was 6 MeV, which increased to 12 MeV at 30 nm (Fig. 5.2 (c)). The energy spectra were exponential (Fig. 5.2 (a)). The electron spectrometer also showed an increase of maximum electron energy for decreasing thickness, such that for the 30 nm target thickness the spectra matches that of the linear case, but was substantially weaker for the 100 nm case (Fig. 5.4).

The x-ray diode showed an increase in signal for both linear and circular polarizations as the target thickness was decreased below 100 nm. Although the electron spectrometer did not detect any emitted electrons for circular polarization with thicker targets, the sodium iodide scintillator is a much more sensitive diagnostic for electrons in the keV range. The electrons that undergo bremsstrahlung in a thick target such as a polished silicon wafer ($550\mu\text{m}$ thickness) can in turn have the strength of the x-ray signal measured. Adjusting the focus allows for different intensities to be present on target, and thus a different electron temperature. For circular polarization, this signal is strongly peaked at the highest intensity, indicating a small amount of electron heating is occurring only at the highest intensities (see fig. 5.3). Linear polarization shows a signal that is peaked with highest intensity, but falls off slowly with decreasing laser intensity.

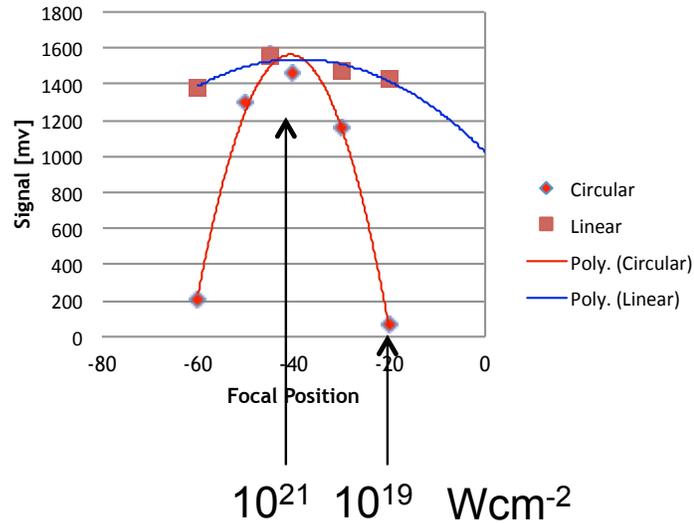


Figure 5.3: Signal on NaI scintillator for varying focal position for both linear and circular polarization at normal incidence. Target is a silicon wafer. A quadratic fit is made to the data points to identify the optimal focal position. Intensities of interest are noted. Focal positions are relative.

At energies beyond the end of the exponential tail of the energy spectra in both polarizations for the 30 nm targets, a small signal was also observed at relatively high

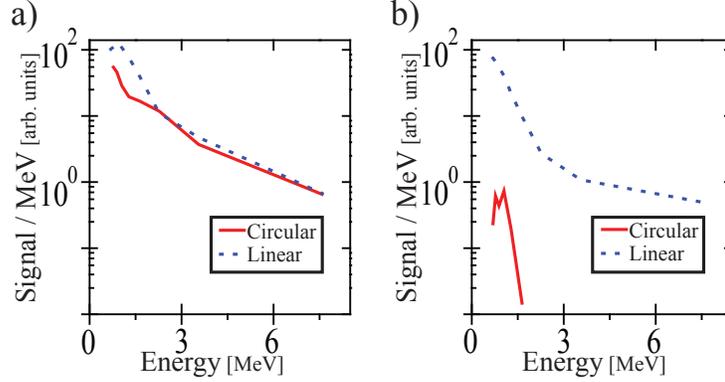


Figure 5.4: Electron energy spectra for right-hand circular (solid) and linear (dashed) polarized laser pulse interaction for a) 30 nm and b) 100 nm Si_3N_4 targets.

energies in the carbon spectra (Fig. 5.7 (a) and (b)). The quasi-monoenergetic peak was observed in the C_6^+ ion spectra that corresponded to energies between 3 and 12 MeV per nucleon. This peak had an energy spread of $\Delta E \approx 66\%$, with the maximum energy for the circular case approximately 2 MeV per nucleon higher than that of the linear case. Note that the energy resolution was rather poor at these energies in the TP such that the error is ≈ 1 MeV per nucleon. It is also possible that this is due to fully ionized bulk target ions as they possess an indistinguishable charge to mass ratio, however due to the prominence of the C_5^+ ions compared to the Si and N ions it is more likely that it is due to C_6^+ ions. It is possible that such a signal exists for the protons as well, but the response of the MCP to protons is weaker than that to carbon ions, and there consequently was not a sufficiently strong signal on the CR-39 and the MCP to distinguish from background.

5.4 High Intensity Absorption

The term absorption will refer to in the strict sense light in the fundamental frequency that is lost during the interactions. The modes of energy loss include scatter, electron and ion heating, as well as harmonic generation and SRS. The screen

was calibrated by imaging the low-power regenerative amplified laser reflecting off a defocused target as well as a calorimeter. The laser pulse was stretched to avoid damaging the optics and causing breakdown in air.

5.4.1 S Polarization

Defocusing the target by 40 microns with S polarization brings the on target intensity to $\sim 10^{17} \text{Wcm}^{-2}$. For comparison, this is an order of magnitude higher than the intensity for use in a typical plasma mirror setup [33]. When the target is positioned this far off in focus, the reflected beam profile from a silicon wafer target appears identical to the low intensity case with a reflectivity of 70%, what is to be expected from a plasma mirror with high contrast (see Fig. 5.5). When the target is placed at the focus, no change in the structure is detected, however, the reflectivity decreases to 53%. Unfortunately, due to the geometry of the chamber, a 45 degree geometry that allows space for a screen does not allow space for a TP to be placed, as the target stage and the OAP block too much of the solid angle for both detectors to be fielded simultaneously. However, an electron spectrometer was placed 10 degrees towards grazing from the specular direction (see fig. 5.1).

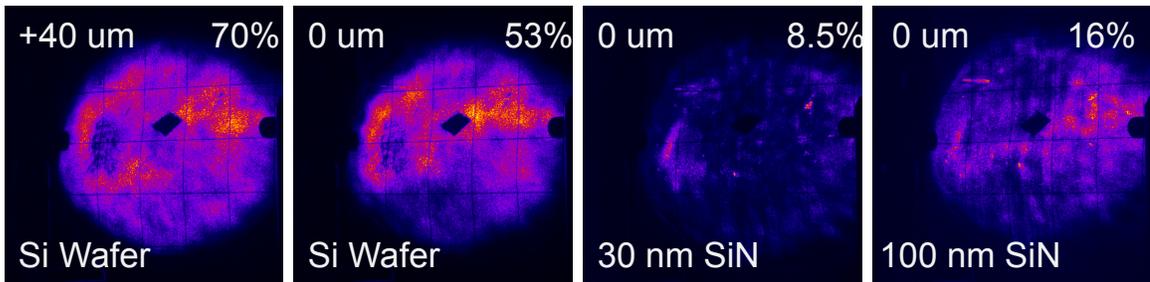


Figure 5.5: Reflection profiles for S polarization. The reflectivity at 800 nm is shown in the upper right, while the focal position is shown in the upper left.

For the submicron targets, however, the reflectivity began to fall as the target thickness decreased. The minimum reflectivity was measured to be 8.5%. The reflected beam profile showed strong modulations for the intensity profile of the laser,

however, the beam itself remained well contained. This would indicate that the absorption is not due to a large scale length plasma.

5.4.2 P Polarization

For P polarization, the presence of absorption mechanisms such as resonance absorption means that the reflectivity will be much lower when compared to the S polarization case. The reflectivity from a silicon wafer showed strong filamentation and absorption at focus, with a reflectivity of 17% as shown in figure 5.6. The reflected beam profile no longer had a well defined diameter, but rather a spread of laser energy spread over the screen. The submicron targets displayed stronger modulations, however the beam was spread over the entire screen and it is uncertain if the laser was absorbed or simple scattered. When the fused silica target was used instead of the silicon wafer, the reflected beam profile improved in quality substantially, although the reflectivity remained much smaller than that of the S polarization case (30%).

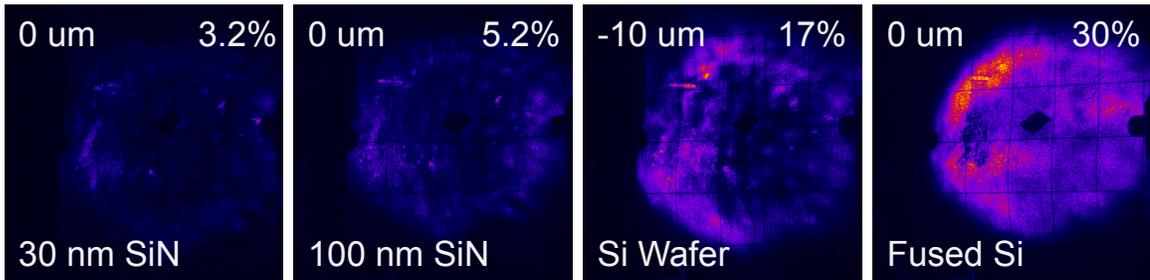


Figure 5.6: Reflection profiles for P polarization. The reflectivity at 800 nm is shown in the upper right, while the focal position is shown in the upper left.

5.5 Discussion and Simulations

Electron heating was not suppressed for thin foils with circular polarization, a critical requirement for RPA. The effect displays some intensity dependence as shown

in figure 5.3. A stronger dependence was found to be related to target thickness, where electron heating and ion acceleration dramatically rose from below detection thresholds to being indistinguishable from linear polarization. A similar phenomenon is observed with the 45 degree experiment with S and P polarization. Although ions were not measured for the absorption experiment, electrons were only detected for the 30 nm targets for S polarization, indicating that increased heating is occurring for the thinnest targets as well, which may be the source of the increased absorption.

The increased electron energy indicates that rather than achieving RPA, we are predominantly coupling laser energy to electron heating. It is unlikely that the target expanded to a non-relativistic underdense plasma, or even a relativistically underdense plasma by prepulse for the circular case, as this would suggest far more expansion when compared to the linear case. The proton energies never dropped for either polarization for decreasing thickness, which is an indicator of a target that is becoming underdense [62] and was not observed experimentally.

To observe the source of the electron heating, 2D3P simulations using the PIC code OSIRIS [43] were performed. A fully ionized carbon target ($n_e = 500n_{crit}$) with 6 nm proton layers ($n_e = 100n_{crit}$) on the front and rear surfaces was used to match the experimental conditions of contaminants on a thin foil, in contrast to the single species simulations performed prior. The input polarization and the target thickness were also varied. The target thicknesses used were 24 nm (thin) and 96 nm (thick) to give a total target thickness of 36 and 108 nm respectively, with a transverse dimension of 14 μm . The incident pulse had a pulse length of 40 fs, and a field strength parameter of $a_0 = 30$ focused to a 1.1 μm FWHM Gaussian spot. The cell size was 2.88 nm in both directions with at least 32 particles per cell (256 particles per cell for the proton layer). The particles were preferentially distributed in the longitudinal direction, so better statistics are available in the acceleration direction, similar to the approach in chapter IV.

5.6 Thin Foil Absorption at High Intensities

For thin targets, initially the target focal area is accelerated forward by RPA with minimal electron heating, but as the target becomes rapidly deformed, the electrons begin to be heated efficiently via direct laser acceleration [46] and Brunel heating [12], because the target surface normal is no longer perpendicular to the laser field. For the circular heating case, we can observe this heating due to surface deformation by considering the variance of the transverse electron momenta and the mean target displacement along the laser axis. Plotting these values versus time, we can observe a clear correlation of target deformation to electron heating for thin targets with circular polarization (Fig. 5.9 (e) and (f)). Here we use a Gaussian rather than a super-Gaussian focus, and so the curvature is across the entire focal spot rather than simply at the edges of the focus. These hot electrons form a sheath field, which is strongest near the focal area. 168 fs after the pulse interacts, TNSA has accelerated protons to appreciable energies (10–20 MeV) for the thin targets, with the focal area protons possessing not only higher energies but also a much larger divergence (Fig. 5.9 (a) and (c)). The increased divergence of the focal area protons is predominantly due to the initial curvature of the target and the subsequent acceleration from sheath fields. For both polarizations the proton energy spectra was exponential for the TNSA accelerated protons. A much smaller population with a large divergence due to RPA indicated a narrow energy spread peak between 30 and 60 MeV.

Thicker targets take longer to accelerate the focal volume and as a result will deform at much later times. Hence, for circular polarization significantly less energy can be transformed into hot electrons. The maximum proton energy decreases slightly for TNSA accelerated protons in the linear case compared with thin targets, whereas for circular polarization acceleration is almost entirely suppressed.

In the 2D simulations, protons in the focal area display a divergence of $\sim \pi$ radians. Using this to estimate the solid angle emission of 2π steradians, for a proton density

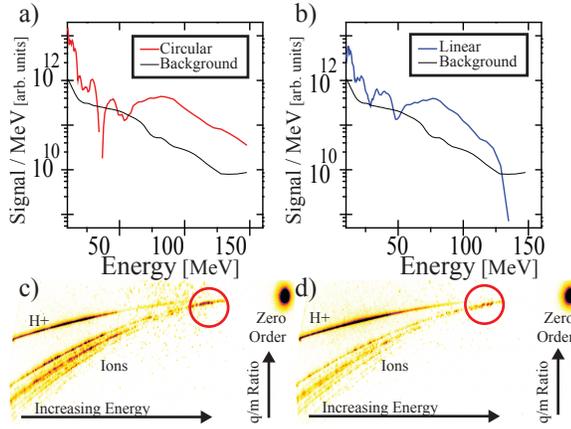


Figure 5.7: C_6^+ energy spectra for a) right-hand circular and b) linear polarized laser pulse interaction for 30 nm Si_3N_4 targets. Detector background levels are shown for comparison. Raw spectra are shown for c) circular and d) linear polarization, with the high energy carbon peak denoted by the red circle.

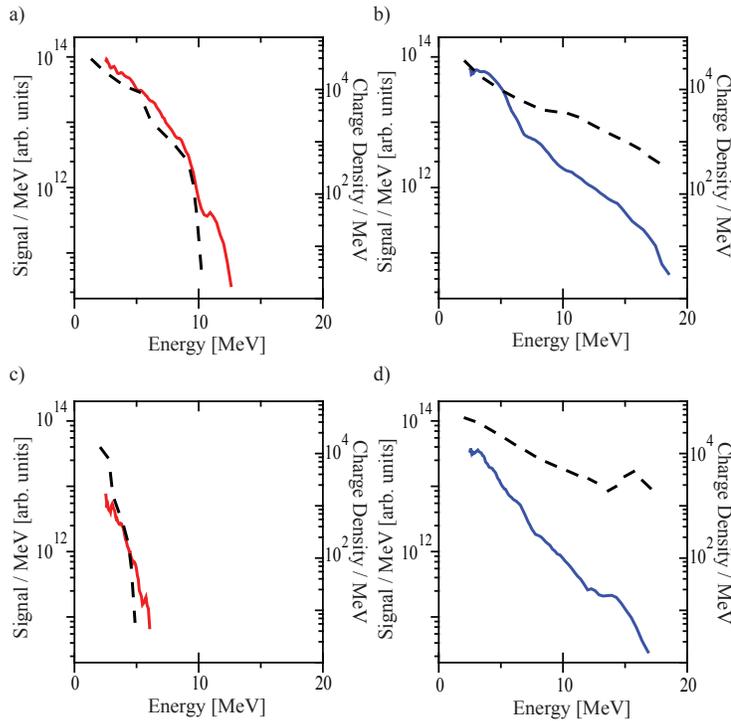


Figure 5.8: PIC simulated proton energy spectra overlaid with experimental spectra. Circular results are shown for a thin (a) and thick (c) target, while linear results are shown for thin (b) and thick (d) targets. The simulation results are shown with the dashed line.

of 10^{23}cm^{-3} and our detector solid angle, we would only expect on the order of ~ 1 protons to enter our detector. By contrast, protons from the surrounding area that undergo TNSA have a much smaller divergence; on the order of milliradians. We can estimate $\sim 10^6$ protons can reach the detector, a difference in 6 orders of magnitude, which explains the absence of RPA protons in the experimental measurement. For this reason, the protons from the focal region need not be considered at all. The dominant source available for detection is by far the sink of protons that lie surrounding the focal area that are accelerated via TNSA. When the spectra of the TNSA accelerated protons from the rear are considered, a striking agreement can be seen when compared to the experimental data (Fig. 5.8). This can be measured by imaging the source with CR-39 with a mesh in between.

However, a narrow energy spread feature in the spectra is observed for thin foil C_6^+ ions. The mechanism for the acceleration of these ions is difficult to determine. The velocity of the C^{6+} ions in this quasi-monoenergetic bump indeed match the velocities of the proton spectra, strongly suggesting that the mechanism is RPA. However, the protons appear to be accelerated via TNSA, and have an overall qualitatively different spectral shape (Boltzmann-like rather than a peak). The spectra is also identical for both linear and circular, such that the electron heating is not suppressed in either case for the thinnest targets. The fact that only the carbon ions are observed to be accelerated to high energies would suggest that a mechanism like the breakout afterburner is more appropriate. This explanation is problematic as well, however, as the carbon ions are only found in the contaminant layer for these targets, *not* in the bulk.

One last consideration to note is that the TP has a much higher sensitivity to high energy carbon ions. The MCP detector used has a 400 nm electrode on the surface that is well suited for stopping lower energy protons. However, due to the Bragg peak, higher energy protons will not deposit as much of their energy at the electrode surface

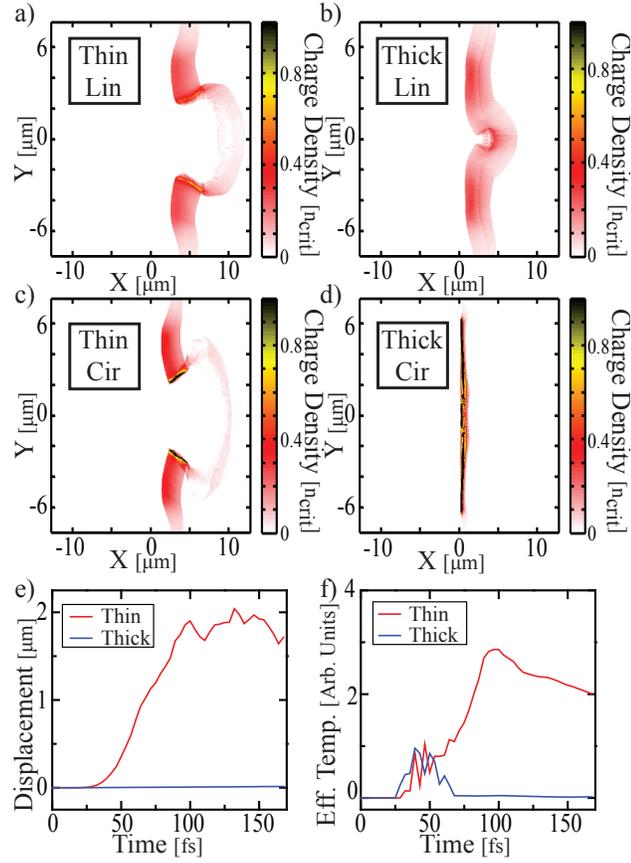


Figure 5.9: Proton density space of OSIRIS 2D PIC simulations for a) thin linear, b) thick linear, c) thin circular, and d) thick circular cases taken at 168 fs. For the circular case, the mean target displacement along the laser axis v. time is shown in e), and the effective temperature v. time is shown in f). “Thin” and “thick” correspond to a total target thickness of 36 nm and 108 nm respectively with the target left justified at an x position of 0.

(see fig. 5.10). The amount of energy deposited from a 30 MeV proton as compared to a 1 MeV is approximately an order of magnitude. Carbon ions, however, have a much stronger stopping power due to their increased mass, which allows them to be distinguished from the background (Fig. 5.7 (a) and (b)). The TP cannot distinguish any fully ionized light ion species², so there is a chance that it is a species other than carbon, however, the lack of higher charge states of the other ions makes this unlikely. The simulations suggest that the focal volume ions on the rear of the target gain some velocity from the initial interaction, but lose desirable beam qualities due to the subsequent acceleration by the sheath.

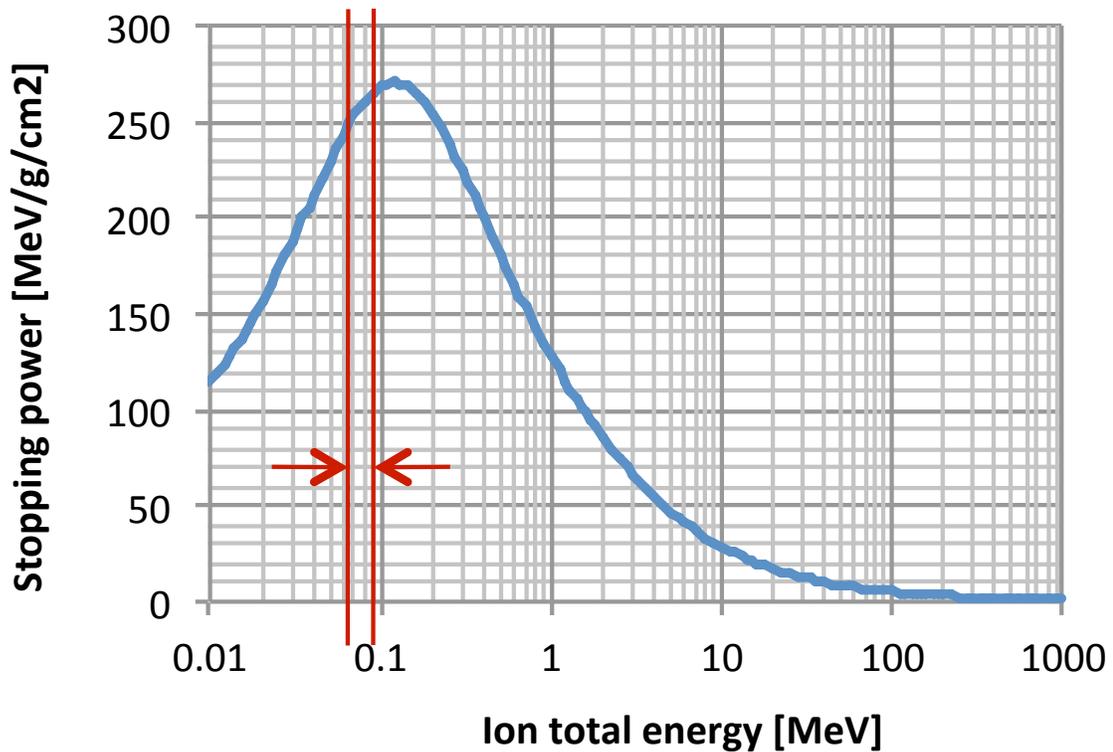


Figure 5.10: Stopping power of protons in the MCP electrode. Protons with an energy of 60-80 keV will be fully stopped in the electrode, as highlighted in red.

²Other than Hydrogen.

5.7 Simulation Validation

As it has been shown, simulations can make assumptions that have powerful implications for practical experiments. Rather than inherently trust the simulations produced, a number of tests were performed to observe the effects from the assumptions made for the preceding simulations. There are quite a number of assumptions that are inherent in any PIC simulation, let alone the simulations performed for the experiment. First, a brief discussion of the implications of using a PIC code will be discussed for the experiment, and then the implications of the assumptions made in the above simulations and the tests performed to understand the effect will be discussed.

PIC makes several assumptions that may have a role in the actual physics. The code assumes that every ion in the plasma is at a particular ionization state, which for these intensities is a good approximation at the focal area but perhaps a poor approximation outside the focal area. The electron dynamics will be dependent strongly on whether the transport is through a plasma or a dielectric. Since PIC is inherently collisionless, the electron transport far from the focal area may not be modeled as well. The contaminant and target ion fronts outside the focal area may be at an artificially higher charge state, so that the motion of the ion front in the code may be exaggerated. Although the production of high energy photons and particles is not included in the simulation, for such thin targets the energy loss is safely assumed to be negligible.

A number of assumptions are made for the simulations to be performed on the limited computing resources available. The major difference is that the simulations were performed in two spatial dimensions as opposed to three. This is likely to cause a decrease in maximum energy, as particles are no longer confined to a plane. Unfortunately, the required computing power to perform such a simulation was simply not available for this work. The capability to do 3D PIC exists, although the required

computing power is great [109]. For the experiment described above, a 3D geometry is expected to display a higher amount of electron heating due to the increased surface area of the focal spot compared to the 2D geometry. It would be interesting to see the effects of this increased absorption that occurs in 3D for a flat top focus, to see whether or not the RPA mechanism is feasible even with the flat top focal profile.

The other assumptions can be tested, with nontrivial increases in computing time. To make a rigorous study in a limited amount of time, the simulations performed were benchmarked against the circular polarization thin targets. The relatively low number of particles reduced computing requirements and allowed a number of simulation parameters to be tested. Although the resolution of the simulation is high compared to previous studies, there are only two cells per non-relativistic skin depth, a potential cause for concern. The difference between particle weighting schemes may influence the particle energy, since there will be a higher amount of numerical heating for lower particle weighting. The statistics may be poor with few particles per cell, the effects of insufficient particles per cell may include poor spectral quality or modulations in the spectra. Finally, the target may not be wide enough to mitigate the effects of a mass limited target.

Each of the previously mentioned concerns were examined via PIC simulations. Shown in figure 5.11 is a selection of some of the major differences. The high spatial resolution already used in the simulations reduces numerical heating even for the solid densities used in the simulations, as negligible effects are observed when higher order weighting is used. Increasing the resolution by a factor of two displays no quantitative change in the spectra. Increasing the particles per cell led to a smoother spectra, with fewer high frequency modulations but otherwise identical energy spectra. The use of current and field smoothing also did not present any discernible differences, likely due to the high spatial resolution.

Other runs were performed that investigated the effects of modifying the target.

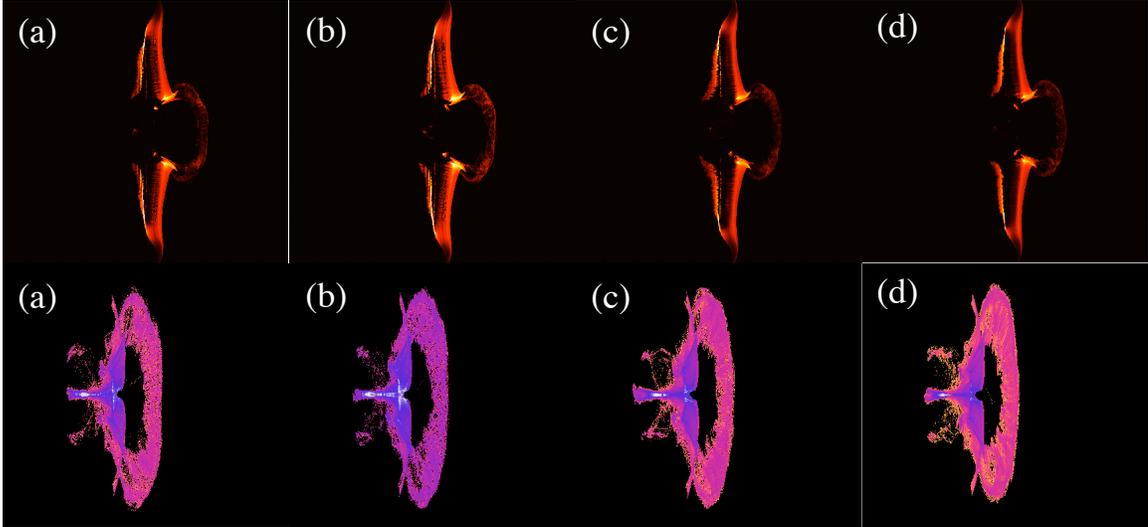


Figure 5.11: PIC simulations for circular polarization and 30 nm targets. Rear proton density (Top) and the rear proton phase space (bottom) are shown. The base case is (a), quadratic particle weighting is shown in (b), 1.5 nm resolution is shown in (c), and 8 times the particles per cell is shown in (d).

A target with double the transverse width was used, with some small effects presenting near the edge of the target, however, this only affected very low energy particles. The few number and low energy of these particles prevented them from being observed clearly in the phase space profile, and thus prevented them from affecting the ion spectra. A thinner proton layer was also investigated, with a thickness half of what is simulated for the experiment. Interestingly, the biggest qualitative change in the proton motion was the lack of protons being accelerated towards the front of the target, towards the laser. Otherwise the spectra in the rear direction displayed similar features with small differences in energy. Although there are still significant assumptions involving target composition and charge state, the performed tests indicate that without the use of a hybrid code the results should match the experimental conditions in the limitations of a PIC code.

5.8 Outlook of Radiation Pressure Acceleration

It is evident then that the experimental conditions are not matched to the RPA regime due to the finite spot effects. The focal spot used in our studies is Gaussian, which will exhibit deformation effects throughout the entire diameter of the focus. A flat-top focus would help dramatically, however, this would require a laser with a near field that is an Airy pattern, a very difficult prospect indeed. A flat top pulse duration would help as well, however, this is likely more difficult than shaping the focus. There is an added difficulty that the plasma mirrors will activate along the rising edge of the pulse, which may pose problems for a sharp rise time in the pulse duration. The simplest approach is to simply increase the focal size to a point where the finite spot effects are mitigated. This is unlikely to be a practical approach. Simply increasing the spot size to increase total flux has the implication that as the focal diameter increases, the required power increases quadratically. An increase in focal diameter to even a 5 micron spot size would increase the required power to 2.5 petawatts, just beyond current laser capabilities. Yet another approach would be to use mass limited targets, which may suppress the effects of electron heating. Of course, a nm thick target that is mass limited is very difficult not only to fabricate, but also to manipulate. More study is needed to see if the preceding suggestions would yield a desirable ion beam.

The problems presented both experimentally and through numerical simulations would seem to indicate that RPA is not a possible mechanism. This is not the intention of the chapter. Several important physical observations were made throughout this experiment. The presence of heating is strongly connected to the deformation of the target, which redefines high intensity interactions for ultrathin foils. The use of circular polarization strongly reduces the effects of the picosecond prepulse, and is a very inexpensive and convenient method of reducing preplasma formation for these targets. The use of plasma mirrors may not be necessary for the study of ultrathin

targets, allowing for substantial increases in intensity on target.

There is also the result of the high energy peak in the carbon spectra. The exact mechanism for accelerating the carbon ions in a manner that is polarization independent is difficult to determine. While there are convincing arguments for both RPA and Breakout Afterburner, it could also be a sign of an entirely different mechanism. In the event that this is a small signal of RPA, the large Poynting flux from the sharp focusing may be responsible for the large divergence. Increasing the focal spot would require a much more powerful laser, as discussed previously, though if one had access to a laser with such a large power it would also be possible to simply forget light-sail RPA and instead use a tight focus with linear polarization and explore the laser-piston regime instead [40].

5.9 Conclusions

Experiments were performed to investigate the effects of circular polarization on ion acceleration with ultra-short pulses at high intensity. We find that below a threshold thickness of 100 nm, circular polarization begins to heat electrons and accelerate the surrounding contaminant ions via TNSA. Simulations show that target deformation provides a mechanism for laser energy to efficiently couple to the electrons, and TNSA occurs as a result. To minimize electron heating and more efficiently transfer momentum to the target, one would likely require comparable intensities but with a much larger focal diameter, requiring laser energies beyond current capabilities but may be possible on future platforms [98]. RPA may not be a practically achievable for NIR lasers, although recent work with longer wavelengths shows promise [104]. It is clear that future simulation work around novel acceleration mechanisms need to make practical assumptions over laser power, intensity, and finite pulse and spot effects.

CHAPTER VI

High-order harmonic generation from solid density targets

6.1 Introduction

The use of coherent x-ray beams with attosecond ($< 10^{-15}$ seconds) pulse durations enables measurements of fundamental atomic processes to take place in a completely new temporal regime. High-order harmonic generation using short pulse infrared lasers focused to relativistic intensities on a solid density plasma have been shown to be a bright source of such x-rays [35]. The mechanism generation of such harmonics occurs when the surface electrons are oscillated by the intense laser field at relativistic speeds, and the resulting nonlinearity of the oscillations give rise to re-radiation at harmonics of the fundamental laser frequency as discussed in Chapter II.

With the advent of fourth-generation synchrotron facilities, or the X-ray Free Electron Laser, ultrafast x-ray measurements can be now made with extremely high brightness sources [141]. High intensity interactions with plasma have recently shown that high brightness x-ray production in the soft and hard x-ray regime are achievable through a variety of mechanisms, such as betatron generation from laser wakefield acceleration and high harmonic generation from underdense gas plasmas [67, 108].

In the latter, the harmonic spectra may result in a pulse train of attosecond pulses, although great care must be made to ensure that the emitted light is phase matched.

Harmonics can also be generated from a laser solid interaction, exploiting the inherent nonlinearity that arises in very relativistic interactions. Since the harmonics are generated from a single surface and are generated directly from the laser, they are inherently phase locked. And since the intensities are so high that the solid is immediately ionized, dephasing of harmonics is not a limitation of conversion efficiency. An extraordinary demonstration of this mechanism generated harmonics generated up to several hundred times the fundamental laser frequency [35]. It was noted in that experiment, however, that without taking adequate steps to steepen the temporal laser profile that harmonics could not be produced.

In this chapter the role of the scale length will be introduced. It will be demonstrated that an optimum scale length exists that balances an increase in efficiency as the scale length increases to a limiting factor due to the growth of parametric plasma wave instabilities. Increasing intensities beyond a threshold scale length results in a catastrophic failure mode for harmonic generation. For scale lengths below this threshold, a variety of x-ray properties are optimized including total conversion efficiency, x-ray divergence, and power law scaling. Particle-in-cell simulations show striking evidence of the loss mechanism through parametric instability and self phase modulation, which affect the produced spectra and conversion efficiency dramatically. This discovery reveals an optimal scale length for HOHG that is applicable for all short pulse laser systems at any relativistic intensity currently attainable.

6.2 Plasma Scale Length

A critical parameter of any laser solid interaction is the density profile. Experiments have shown that the amount of absorption and hot electron production are strongly linked to the density profile, and can have a large effect in the experiments

if not well controlled [62]. Particularly in the case of short pulse laser systems that operate at extremely high intensities, prepulses may get focused to intensities high enough to cause absorption which can alter the density profile in a manner similar to the density shaping employed in Chapter IV. How “clean” a laser pulse can be is often measured by the laser intensity contrast, a ratio of the prepulse to the main pulse. Many laser systems have a native contrast level that is inadequate to maintain steep density profiles, placing a limit on the intensity of the experiment.

The density profile will be defined by a characteristic scale length, where scale length refers to the decay constant in the assumed exponential profile (e.g., $n_e(x) \approx n_0 \exp(-x/\tau)$). The role of the scale length has been elusive so far. The density profile of the plasma must be steep enough to allow for a well defined surface to exist [147]. With sufficiently high contrast, there is a well defined reflection point that exists at the relativistic critical surface, which is modulated by the relativistic motion of the electrons. This is critical to harmonic generation to maintain phase locking and removing additional dispersive effects. If the scale length is too long, the laser can simply hole-bore into the plasma. In this situation, the apparent reflection point is constantly moving into the target in a spatially varying manner and a phase locked reflected beam cannot be generated. However, it has also been observed that the efficiency of the harmonic generation can be increased with increasing scale length [8]. This can be understood by the fact that the laser skin depth is larger for longer scale lengths, so that more emitters are available to radiate. Then an optimal scale length must exist in which for a given set of experimental parameters the production of harmonics is optimized (Fig. 6.1).

6.3 Experimental Setup

The experiments were performed to investigate the effects of the scale length with a high resolution extreme ultraviolet (EUV) spectrometer. Using a pair of plasma

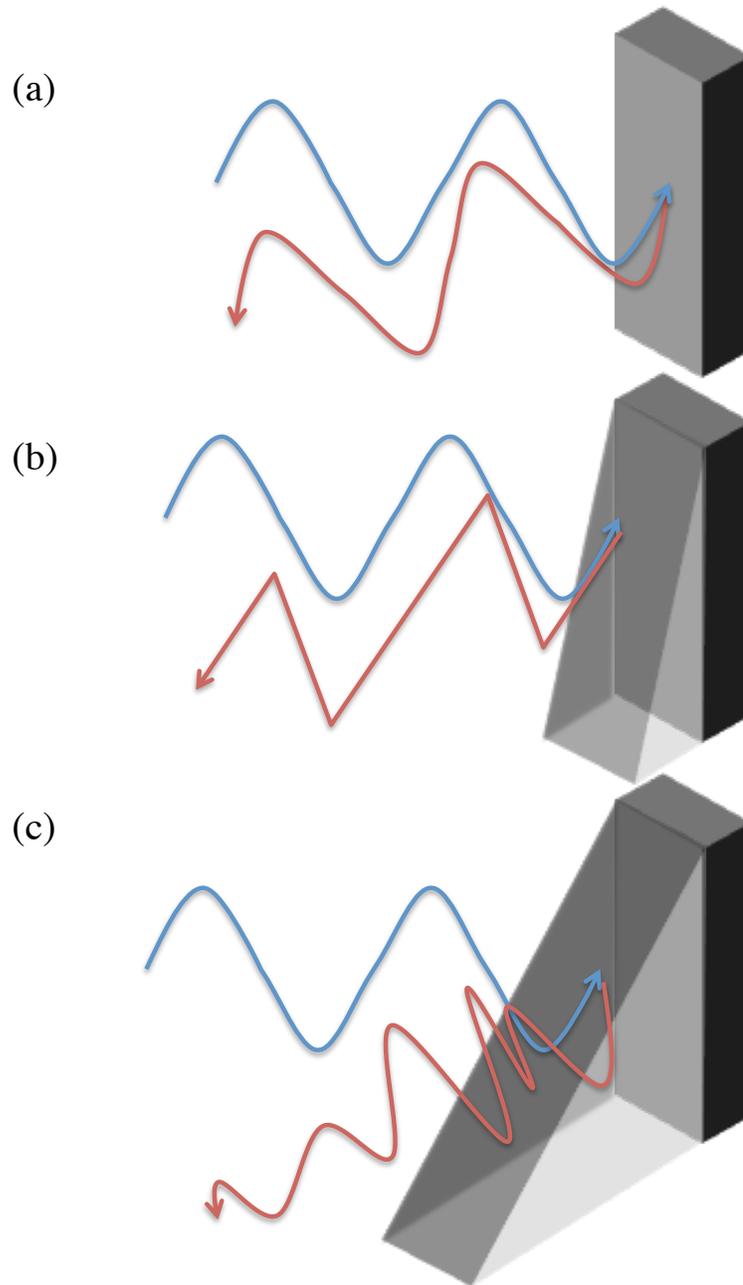


Figure 6.1: Experimental conditions for generating a slightly perturbed reflected spectra from (a) a sharp density profile, (b) a strongly anharmonic spectra from a nominal scale length value, and (c) a highly modulated spectra from a long scale length.

mirrors we were able to increase laser contrast and by varying the reflectivity of the plasma mirror a variety of scale lengths were easily accessible. With the optimal coatings for the plasma mirrors, the contrast improvement was 5 orders of magnitude, high enough so that plasma formation is limited to within a picosecond of the main pulse. Fine control of plasma scale length was achieved using a secondary beam in which an adjustable intensity ($\sim 10^{10} - 10^{17} \text{ Wcm}^{-2}$) short pulse laser pulse interacted with the target 63 ps prior to the main pulse ($2 \times 10^{21} \text{ Wcm}^{-2}$, 40 fs). The laser interacted with polished silicon wafer and fused silica, providing both a high and low damage threshold targets (and thus a longer and shorter scale length for each laser condition). The increase in scale length for the two targets can be clearly observed through the P polarization absorption measurements made in Chapter V.

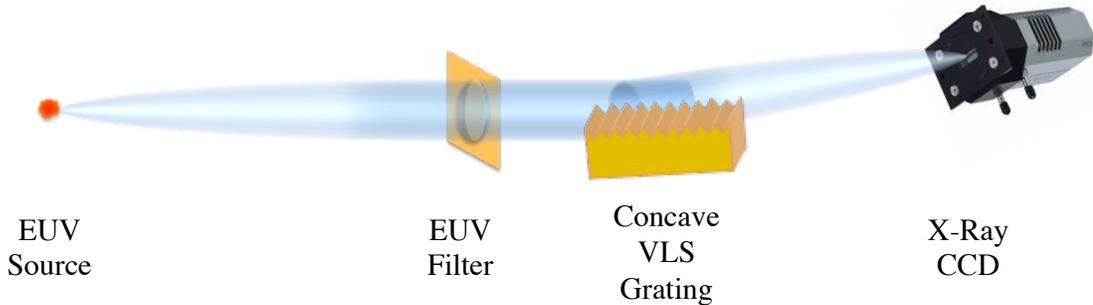


Figure 6.2: Schematic diagram of the HHG experiment. The source is imaged to the detector plane via a cylindrically focusing variable-line-space grating. The detector is a direct detection x-ray CCD.

6.3.1 EUV Spectrometer

The flat-field extreme ultraviolet spectrometer consisted of a variable line space concave grating (1,200 lines per mm) that diffracts and focuses the harmonic light onto the detector, which in our case is a charged-coupled detector (CCD). A diagram of the spectrometer is shown in figure 6.2. The spectrometer has a resolving power of 1200 for the wavelength range of 15-25 nm, and subtends an angle of 1.7×10^{-5} sr.

800 nm of aluminum is used to filter out optical light. The detector is time-averaged, so in addition to the harmonic signal continuum and line emission is also detected from the plasma, resulting in the bright noise near the absorption edge in Fig. 6.3.

6.4 Scale Length Results

What is experimentally observed with both coarse and fine control of scale length is three distinct regimes of harmonic generation (Fig. 6.3). The shortest scale length was observed with no introduced prepulse and a fused silica target, with a 9 nm scale length ($\tau \sim \lambda/100$). For this ultra-clean case, very little is detected within the spectral range of the detector although some shots showed evidence of low order HHG. The raw spectra as well as the response corrected spectra is shown in Fig. 6.3 (a). This clean case is where the density profile is too steep to efficiently produce harmonics. By switching to the silicon wafer, or by introducing the prepulse, we can achieve a scale length of 200 nm ($\tau \sim \lambda/5$). As expected, as the scale length increases we see the harmonic structure grow into a bright well arranged structure seen in Fig. 6.3 (b). However, an abrupt change occurs beyond a threshold scale length, the harmonic structure is lost completely and although emission occurs strongly and discrete lines are observed for the scale lengths between 0.5 and 1.8 μm , as shown in Fig. 6.3 (c). These lines vary randomly in frequency and amplitude from shot to shot. Generating bright harmonics such as those shown in Fig. 6.3 (b) was not as consistent as some of the other conditions, suggesting that the scale length range for this optimal HHG is very narrow. Since the expansion of the plasma is strongly linked to the start of preplasma formation, small fluctuations in laser energy can have drastic effects on the scale length.

The experimentally observed efficiency of the harmonic generation follows a power law scaling of n^p with n as the specific harmonic order, the factor p is minimized to 4.3 - 4.8 for the optimal HHG case, and has a range of 5.2 - 10 for the other scale

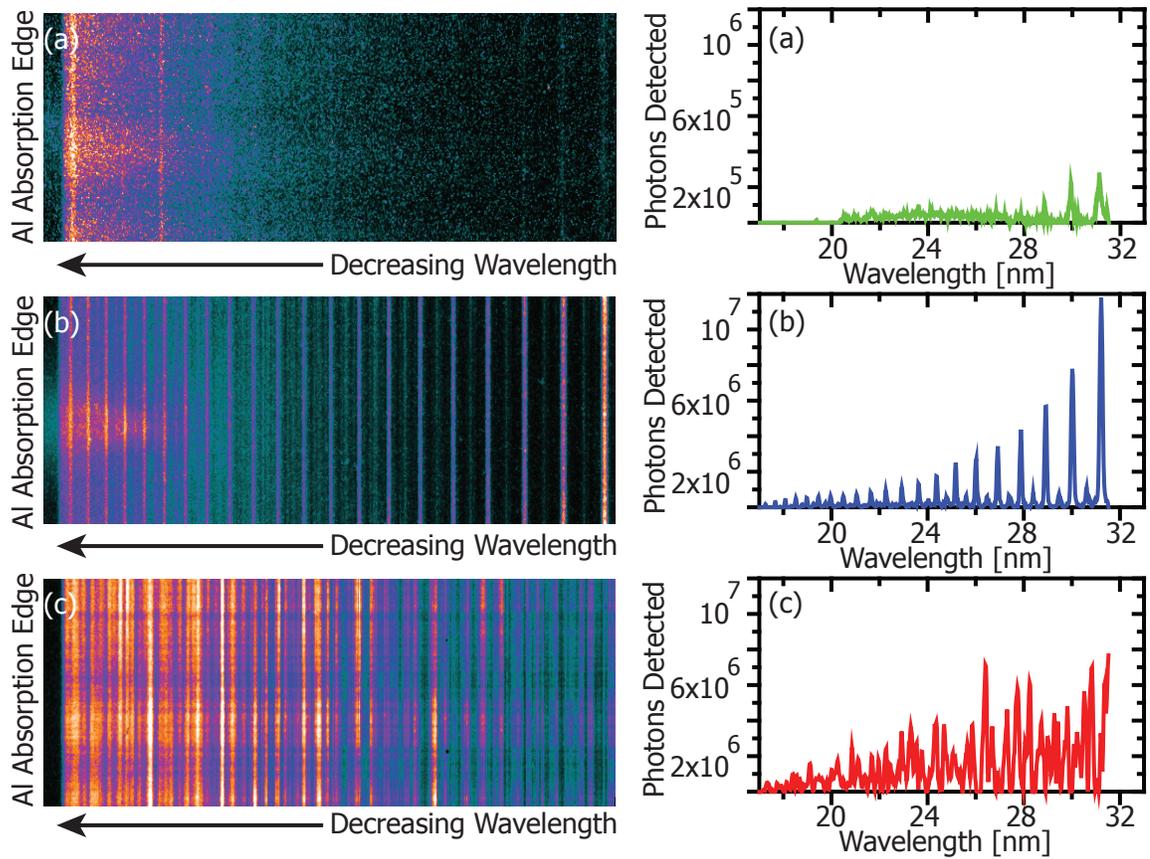


Figure 6.3: Raw, single shot EUV spectrometer images (left) and response corrected lineouts (right) for ultra-sharp density profile (a), nominal c/ω_p scale length (b), and λ scale lengths (c). The Al x-ray filter causes a sharp drop in transmission at 172 angstroms.

lengths, agreeing with other experimentally observed power law scalings [147]. The strength and spectral width of the plasma emission lines as well as the intensity of the continuum emission present in every shot provide critical information on the plasma density and temperature; for instance, the oxygen 4^+ line at 17.2 nm near the Al absorption cutoff has a much stronger flux for the long scale length shots (Fig. 6.3 (c)) than in the cleaner cases (Fig. 6.3 (a)). For no cleaning of the nanosecond laser pedestal the largest scale lengths are produced ($> 2 \mu\text{m}$) and the laser filaments, which limits the peak intensity reached so there is not a strong driver for HHG.

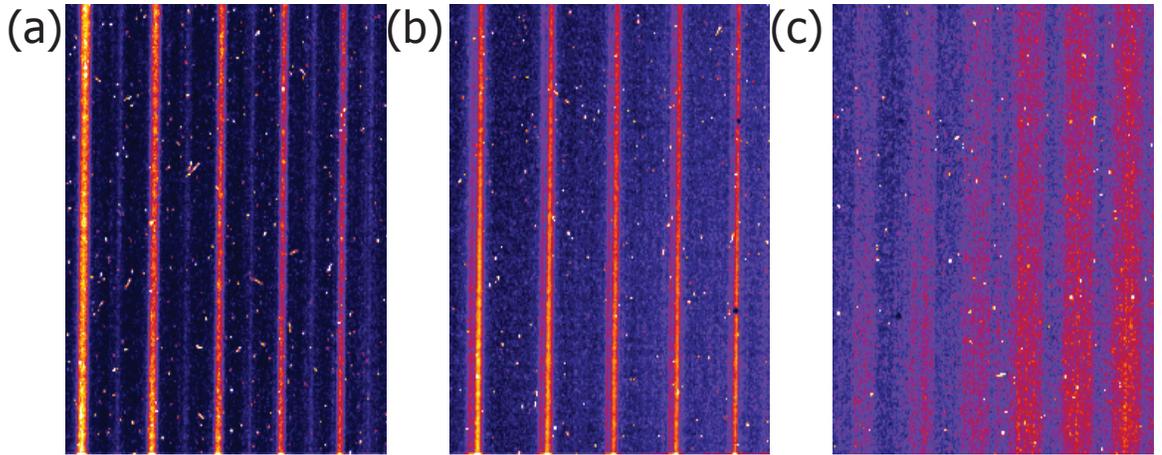


Figure 6.4: EUV Spectrometer data displaying features of half-harmonics (a), sidebands (b), and split harmonics (c) while is the transitional region of scale length. These are indicative of parametric harmonic generation from mechanisms such as SRS and TPD.

6.5 2D Simulations & Discussion

Particle-in-cell simulations provide numerical modeling of the underlying physics. A variety of 1 and 2 dimensional simulations were performed to isolate the physical processes and replicate the conditions of the experiment. The 2 dimensional simulations performed at 45 degree incidence angle show a strong correlation with the experimental results, as shown in Fig. 6.5. For these simulations, the scale length refers to the density profile along the laser direction, so that the actual scale length in

the target normal would be shorter by a factor of $1/\sqrt{2}$. The experimental detector solid angle only covers 3×10^{-5} sr, so without a measurement of the divergence of the particular harmonic, a total conversion efficiency cannot be easily made. However, this is easy to extract from the simulations. When we examine the total conversion efficiency as a function of scale length, we see in Fig. 6.6 (b) that the optimal conversion occurs near the plasma skin depth. In fact, as the intensity increases the optimal scale length appears to converge to this point, due to the fact that the growth rate of the plasma wave instabilities are intensity dependent. Physically, the plasma critical surface is able to increase curvature and increase the electric current (and thus the total number of emitters) as the scale length increases. However, once the scale length is large enough to support plasma waves, which can be coupled to the incident laser via parametric instabilities, energy is quickly lost to the instabilities. Plasma wave formation can be supported when the scale length reaches the plasma spatial wavelength, so at the critical surface where $\omega_p = \omega_0/2$, the minimum scale length necessary for instability creation is the maximum scale length that can be supported for unperturbed harmonic generation.

In addition, the modulations of the spectra may be understood by understanding the propagation of a relativistically intense pulse into the density ramp of the target. Although the laser is still free to propagate in the plasma up to the critical density, nonlinear effects such as relativistic self-phase modulation (SPM) are able to occur that can significantly broaden and modulate the laser spectra [133]. Additionally, with the scale length becoming larger than the plasma skin depth plasma waves can form that can generate parametric instabilities such as Stimulated Raman Scattering (SRS) and Two-Plasmon Decay (TPD). These instabilities convert the fundamental laser frequency to other frequencies through the matching conditions of $\omega_{SRS} = \omega_0 \pm \omega_{laser}$ for SRS or at $\frac{1}{2}\omega_{laser}$ for TPD and can occur near $\frac{1}{4}n_c$, modulating the spectra even before the pulse reflects. As shown analytically [5, 6], the TPD and SRS can

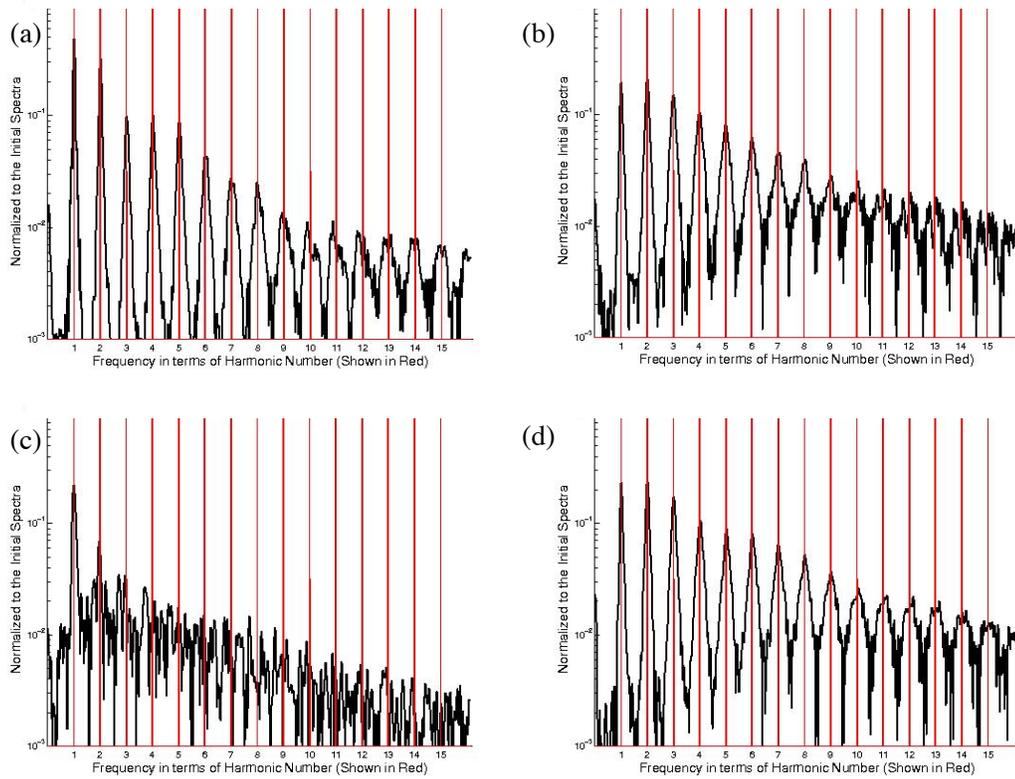


Figure 6.5: PIC Simulations of the reflected spectra for Scale Length of (a) $\lambda_0/160$, (b) $\lambda_0/5$, (c) $\lambda_0/2$, (d) and c/ω_p .

cause the formation of half-integer harmonics and splitting, since the now modulated incident spectra could generate its own harmonics. For longer scale lengths, SPM is able to further modulate the spectra and the side-bands devolve into a complicated spectral structure. Examining the harmonic generation at a scale length between the optimal harmonic generation and the highly modulated regime shows evidence of such parametric instabilities, as shown in Fig. 6.4.

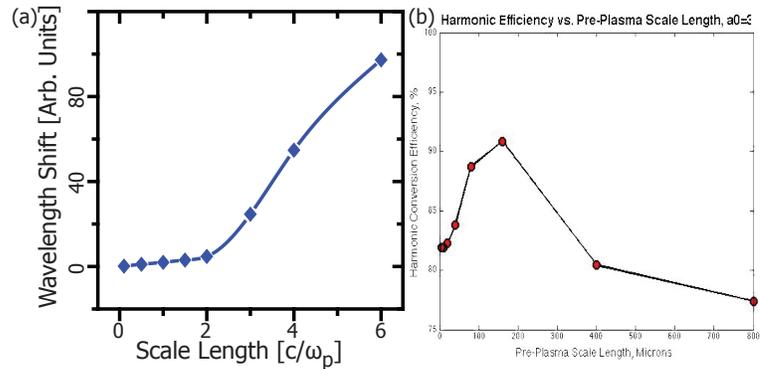


Figure 6.6: The conversion of fundamental laser frequency into other frequencies as a function of scale length from 1D simulations of a circular polarized pulse are shown in (a). The rapid rise due to parametric instabilities can be observed. The total conversion efficiency into high harmonic generation from the 2D simulations is shown in (b). The optimal scale length occurs close to the plasma wavelength.

6.6 1D Simulations

To isolate the effects of the instabilities, 1D particle in cell simulations were performed with circular polarization and normal incidence. The circular polarization removes absorption effects and harmonic generation, so that the dominant physical effects are limited to the plasma wave instabilities. Varying the scale length at a given intensity, we can compare the reflected spectra with that of the incident spectra, providing a measure of how much of the fundamental has been converted to sidebands. We see in Fig. 6.6 (a) that the change remains small until a point where the spectra rapidly increases. When we look at the absorption in the simulation (Fig. 6.6 (b)), we

also observe a similar increase above the nominal scale length as energy is absorbed from the laser pulse to produce a plasma wave, reducing the efficiency.

6.7 Attosecond Generation

Although the additional bandwidth from the longer scale lengths would suggest that perhaps isolated attosecond pulses may be generated, the necessary phase locking for attosecond pulse generation is lost. Examining the plasma wave formation for longer scale lengths in 2D simulations, it can be seen that the plasma waves themselves can reach densities high enough to strongly attenuate the incident beam if not outright reflect it. Because of this, the location where each harmonic is generated can vary during the pulse duration and the phase is no longer matched, leading to the loss of the attosecond pulse train (Fig. 6.7). Thus, particularly for the generation of attosecond pulses is it imperative that the scale length remain below the plasma wavelength.

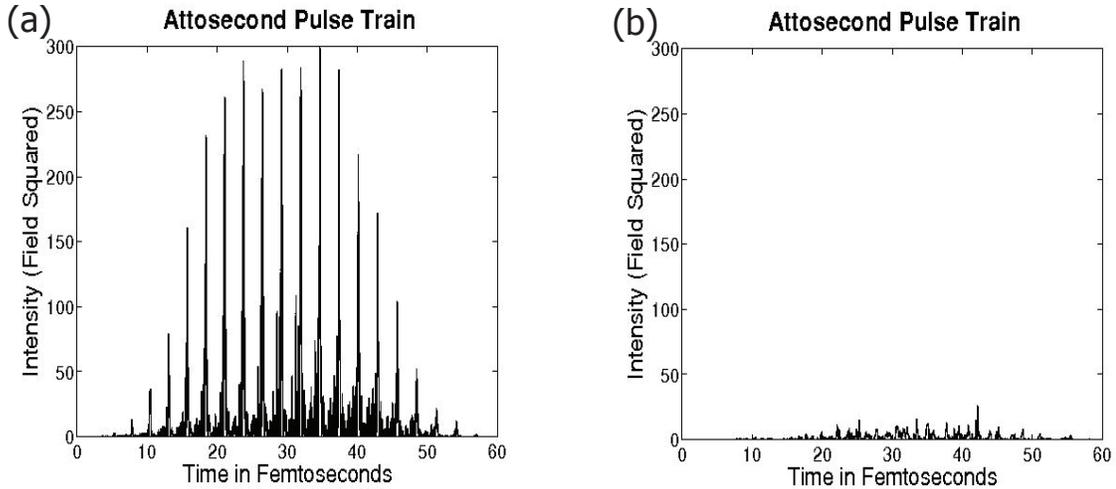


Figure 6.7: 2D PIC simulations of the attosecond pulse train generated in the interaction taken along the specular direction for scale lengths of $\lambda/(2\pi)$ and (b) λ .

6.8 Conclusions

The requirement that the scale length remain below the plasma wavelength is valid for virtually any intense laser solid HHG interaction. An upper limit in intensity may exist when profile steepening occurs within a laser cycle such that the density scale lengths are no longer a good parameter to use for characterization of the interaction. For solid density plasmas ($> 100 n_c$), this would require a temporally clean pulse with intensities greater than 10^{22}Wcm^{-2} , which has not yet been demonstrated experimentally.

CHAPTER VII

Conclusion & Future Outlooks

7.1 Thesis Discussion

This thesis marks one of the first comprehensive experimental campaign into solid density experiments with intensities exceeding 10^{21}Wcm^{-2} . This experimental regime could not properly be studied without sufficiently high laser contrast. The laser contrast was improved to allow the study of ultrathin foil experiments as well as harmonic generation. A campaign to produce high energy, monoenergetic ion beams was unable to be completed due to the failure modes of the RPA mechanism. Instead, protons were accelerated via TNSA due to the strong heating inherent in high intensity interactions with ultrathin targets. While an improvement was observed in ion energies, 20 MeV per nucleon was the highest observed energy during the experiments.

The energy spread from thin foils produced a peak in the energy spectra, but it was far from monoenergetic. Plasma density shaping technique involving a short pulse prepulse was demonstrated, in which quasi-monoenergetic protons were consistently generated. This technique was also shown to work for various other light ion species, providing a simple technique of spectral control that does not involve complex targets or target manipulation prior to the shot.

Finally, harmonic generation from high intensity laser solid interactions was studied in depth. The role of the scale length was investigated, and the loss mechanism

for long scale length interactions was discovered. Since the source of loss is due to plasma waves, the loss mechanism requires a certain length of plasma for the waves to grow. For an exponential density profile, the implication is that this scale length will be universal for a wide range of intensities. This insight allows future experiments to be performed at optimal conditions for nearly any laser system.

7.2 Future Applications & Outlook

A significant number of challenges remain for laser ion acceleration to be practical for a number of applications. However, a number of applications already exist. The use of protons for radiography is a critical diagnostic for measuring the magnetic fields generated in ps interactions. For this application, a large energy spread is actually an advantage. Different protons will have a different time-of-flight, and will therefore interact with plasma at different times. The Bragg peak is well defined for each energy, so a stack of radiochromic film or CR-39 will select various energies of protons. As a consequence, each piece of detector will show a radiograph of the plasma for a particular time. In this way, a detector stack is similar to frames of a movie, and the dynamics of the plasma can easily be measured.

In order for laser ion acceleration to be useful for various other applications, new acceleration mechanisms will need to be discovered. This will require a much deeper understanding of the electron transport in a foil for short pulses. Without a means of suppressing hot electron generation, TNSA is unavoidable in any interaction. Increasing both the charge and energy of the protons beam while decreasing the energy spread is a difficult proposition, and may involve a mixture of acceleration schemes or targets.

Perhaps the brightest application lies in x-ray generation. The harmonic generation mechanism has optimal conditions that are applicable to a wide range of laser systems. The most exciting approach may not be in terms of conversion efficiency,

but in the ease of generating attosecond pulses. The spectrum is capable of supporting attosecond pulses, which are inherently phase locked due to the solid surface. A proposed scheme utilizing the so-called “lighthouse effect” is a simple means of using such a source to generate a single isolated attosecond pulse [131]. A pulse front tilt will manifest itself in the interaction by spatially varying the specular direction of the reflected beam. For a system with a large divergence angle, the reflected attosecond pulse train will be spatially separated and a single attosecond pulse may be selected with a slit. A pulse front tilt can easily be introduced to a CPA laser system by simply tilting the compressor gratings. This may be an achievable means of generating a high-brightness, single attosecond laser pulse.

APPENDICES

APPENDIX A

Useful Relativistic Equations

For the following equations, we will use the convention that a_0 is for linear polarization.

$$a_0 = \frac{eA_0}{m_e c} = \frac{eE_0}{m_e c \omega} \quad (\text{A.1})$$

$$\sqrt{\langle a^2 \rangle} = \frac{1}{\sqrt{2}} a \quad \text{Linear Polarization} \quad (\text{A.2})$$

$$I = \frac{1}{\mu_0} |E \times B|^2 = \frac{\epsilon_0 c}{2} E_0^2 \quad (\text{A.3})$$

$$I \lambda_\mu^2 = a_0^2 \cdot 1.387 \times 10^{18} \frac{W \lambda_\mu^2}{\text{cm}^2} \quad (\text{A.4})$$

$$n_c = \frac{m_e \epsilon_0 \gamma \omega^2}{e^2} = 1.12 \times 10^{21} \frac{\gamma}{\lambda^2} [\text{cm}^{-3}] \quad (\text{A.5})$$

$$F_P = -\frac{m_e c^2}{2\gamma} \nabla |a|^2 = \frac{m_e c^2}{2\gamma} \nabla (\gamma^2 - 1) \quad (\text{A.6})$$

$$\gamma = \sqrt{1 + a^2} \quad (\text{A.7})$$

$$U_P = m c^2 (\gamma - 1) \quad (\text{A.8})$$

$$P_c = \frac{8\pi \epsilon_0 m_e^2 c^5}{e^2} \frac{\omega^2}{\omega_{pe}^2} = 17.5 \frac{n_c}{n_e} [\text{GW}] \quad (\text{A.9})$$

$$E = \frac{\text{MeV}}{c^2} \left[\sqrt{1 + \frac{p^2}{m^2 c^2}} \right] \quad (\text{A.10})$$

BIBLIOGRAPHY

BIBLIOGRAPHY

- [1] The national association for proton therapy website, June 2012.
- [2] M. Allen, P. Patel, A. Mackinnon, D. Price, S. Wilks, and E. Morse. Direct experimental evidence of back-surface ion acceleration from laser-irradiated gold foils. *Physical review letters*, 93(26):265004, 2004.
- [3] U. Amaldi and G. Kraft. Radiotherapy with beams of carbon ions. *Reports on progress in physics*, 68:1861, 2005.
- [4] V. Bagnoud, J. Zuegel, N. Forget, and C. Le Blanc. High-dynamic-range temporal measurements of short pulses amplified by OPCPA. *Optics Express*, 15(9):5504–5511, 2007.
- [5] H. Barr, P. Mason, and D. Parr. Electron parametric instabilities driven by relativistically intense laser light in plasma. *Physical review letters*, 83(8):1606–1609, 1999.
- [6] H. Barr, P. Mason, and D. Parr. Electron parametric instabilities of relativistically intense laser light in under and overdense plasma. *Physics of Plasmas*, 7:2604, 2000.
- [7] F. Beg, A. Bell, A. Dangor, C. Danson, A. Fews, M. Glinsky, B. Hammel, P. Lee, P. Norreys, and M. Tatarakis. A study of picosecond laser-solid interactions up to 10^{19} W cm⁻². *Physics of Plasmas*, 4(2):447–457, 1997.
- [8] M. Behmke, D. An der Brügge, C. Rödel, M. Cerchez, D. Hemmers, M. Heyer, O. Jäckel, M. Kübel, G. Paulus, G. Pretzler, et al. Controlling the spacing of attosecond pulse trains from relativistic surface plasmas. *Physical Review Letters*, 106(18):185002, 2011.
- [9] A. B. Borisov, A. V. Borovskiy, V. V. Korobkin, A. M. Prokhorov, O. B. Shiryaev, X. M. Shi, T. S. Luk, A. McPherson, J. C. Solem, K. Boyer, and C. K. Rhodes. Observation of relativistic and charge-displacement self-channeling of intense subpicosecond ultraviolet (248 nm) radiation in plasmas. *Phys. Rev. Lett.*, 68:2309–2312, Apr 1992.
- [10] R. Boyd. *Nonlinear optics*. Academic Pr, 2003.
- [11] S. Brorson and H. Haus. Diffraction gratings and geometrical optics. *JOSA B*, 5(2):247–248, 1988.

- [12] F. Brunel. Not-so-resonant, resonant absorption. *Physical Review Letters*, 59(1):52–55, 1987.
- [13] S. Bulanov, A. Brantov, V. Bychenkov, V. Chvykov, G. Kalinchenko, T. Matsuoka, P. Rousseau, S. Reed, V. Yanovsky, D. Litzenberg, K. Krushelnick, and A. Maksimchuk. Accelerating monoenergetic protons from ultrathin foils by flat-top laser pulses in the directed-Coulomb-explosion regime. *Physical Review E*, 78(2):1–6, Aug. 2008.
- [14] S. Bulanov, T. Esirkepov, V. Khoroshkov, A. Kuznetsov, and F. Pegoraro. Oncological hadrontherapy with laser ion accelerators. *Physics Letters A*, 299(2-3):240–247, 2002.
- [15] S. Bulanov and V. Khoroshkov. Feasibility of using laser ion accelerators in proton therapy. *Plasma Physics Reports*, 28(5):453–456, 2002.
- [16] N. Burnett and G. Enright. Population inversion in the recombination of optically-ionized plasmas. *Quantum Electronics, IEEE Journal of*, 26(10):1797–1808, oct 1990.
- [17] V. Bychenkov, W. Rozmus, A. Maksimchuk, D. Umstadter, and C. Capjack. Fast ignitor concept with light ions. *Plasma Physics Reports*, 27(12):1017–1020, 2001.
- [18] R. L. Carman, D. W. Forslund, and J. M. Kindel. Visible harmonic emission as a way of measuring profile steepening. *Phys. Rev. Lett.*, 46:29–32, Jan 1981.
- [19] R. Cassou and E. Benton. Properties and applications of cr-39 polymeric nuclear track detector. *Nuclear Track Detection*, 2(3):173–179, 1978.
- [20] F. Chen. *Introduction to plasma physics and controlled fusion: plasma physics*, volume 1. Springer, 1984.
- [21] H. Chen, S. Wilks, J. Bonlie, E. Liang, J. Myatt, D. Price, D. Meyerhofer, and P. Beiersdorfer. Relativistic positron creation using ultraintense short pulse lasers. *Physical review letters*, 102(10):105001, 2009.
- [22] V. Chvykov, C. Radier, G. Chériaux, G. Kalinchenko, V. Yanovsky, and G. Mourou. Compression of ultra-high power laser pulses. In *Conference on Lasers and Electro-Optics*. Optical Society of America, 2010.
- [23] V. Chvykov, P. Rousseau, S. Reed, G. Kalinchenko, and V. Yanovsky. Generation of 10 11 contrast 50 tw laser pulses. *Optics letters*, 31(10):1456–1458, 2006.
- [24] E. L. Clark, K. Krushelnick, J. R. Davies, M. Zepf, M. Tatarakis, F. N. Beg, A. Machacek, P. A. Norreys, M. I. K. Santala, I. Watts, and A. E. Dangor. Measurements of energetic proton transport through magnetized plasma from intense laser interactions with solids. *Phys. Rev. Lett.*, 84:670–673, Jan 2000.

- [25] C. Clayton, M. Everett, A. Lal, D. Gordon, K. Marsh, and C. Joshi. Acceleration and scattering of injected electrons in plasma beat wave accelerator experiments. *Physics of plasmas*, 1:1753, 1994.
- [26] C. E. Clayton, C. Joshi, C. Darrow, and D. Umstadter. Relativistic plasma-wave excitation by collinear optical mixing. *Phys. Rev. Lett.*, 54:2343–2346, May 1985.
- [27] B. Cohen. Breeder reactors: A renewable energy source. *Am. J. Phys.*, 51(1):78, 1983.
- [28] T. E. Cowan, J. Fuchs, H. Ruhl, A. Kemp, P. Audebert, M. Roth, R. Stephens, I. Barton, A. Blazevic, E. Brambrink, J. Cobble, J. Fernández, J.-C. Gauthier, M. Geissel, M. Hegelich, J. Kaae, S. Karsch, G. P. Le Sage, S. Letzring, M. Manclossi, S. Meyroneinc, A. Newkirk, H. Pépin, and N. Renard-LeGalloudec. Ultralow emittance, multi-mev proton beams from a laser virtual-cathode plasma accelerator. *Phys. Rev. Lett.*, 92:204801, May 2004.
- [29] J. Davis and G. Petrov. Angular distribution of neutrons from high-intensity laser–target interactions. *Plasma Physics and Controlled Fusion*, 50:065016, 2008.
- [30] A. D. Debus, M. Bussmann, U. Schramm, R. Sauerbrey, C. D. Murphy, Z. Major, R. Hörlein, L. Veisz, K. Schmid, J. Schreiber, K. Witte, S. P. Jamison, J. G. Gallacher, D. A. Jaroszynski, M. C. Kaluza, B. Hidding, S. Kiselev, R. Heathcote, P. S. Foster, D. Neely, E. J. Divall, C. J. Hooker, J. M. Smith, K. Ertel, A. J. Langley, P. Norreys, J. L. Collier, and S. Karsch. Electron bunch length measurements from laser-accelerated electrons using single-shot thz time-domain interferometry. *Phys. Rev. Lett.*, 104:084802, Feb 2010.
- [31] T. Ditmire, E. Gumbrell, R. Smith, L. Mountford, and M. Hutchinson. Supersonic ionization wave driven by radiation transport in a short-pulse laser-produced plasma. *Physical review letters*, 77(3):498–501, 1996.
- [32] F. Dollar, T. Matsuoka, G. Petrov, A. Thomas, S. Bulanov, V. Chvykov, J. Davis, G. Kalinchenko, C. McGuffey, L. Willingale, V. Yanovsky, A. Maksimchuk, and K. Krushelnick. Control of Energy Spread and Dark Current in Proton and Ion Beams Generated in High-Contrast Laser Solid Interactions. *Physical Review Letters*, 107(6):1–5, Aug. 2011.
- [33] G. Doumy, F. Quéré, O. Gobert, M. Perdrix, and P. Martin. Complete characterization of a plasma mirror for the production of high-contrast ultraintense laser pulses. *Physical Review E*, 69(2):1–12, Feb. 2004.
- [34] B. Dromey, S. Kar, M. Zepf, and P. Foster. The plasma mirror—A subpicosecond optical switch for ultrahigh power lasers. *Review of Scientific Instruments*, 75(3):645, 2004.

- [35] B. Dromey, M. Zepf, A. Gopal, K. Lancaster, M. Wei, K. Krushelnick, M. Tatarakis, N. Vakakis, S. Moustazis, R. Kodama, et al. High harmonic generation in the relativistic limit. *Nature physics*, 2(7):456–459, 2006.
- [36] M. Edwards, J. Lindl, B. Spears, S. Weber, L. Atherton, D. Bleuel, D. Bradley, D. Callahan, C. Cerjan, D. Clark, et al. The experimental plan for cryogenic layered target implosions on the national ignition facilitythe inertial confinement approach to fusion. *Physics of Plasmas*, 18:051003, 2011.
- [37] A. Ehler and G. Weissler. Vacuum ultraviolet radiation from plasmas formed by a laser on metal surfaces. *Applied Physics Letters*, 8(4):89–91, 1966.
- [38] A. Einstein. On the electrodynamics of moving bodies. *Annalen der Physik*, 17(891):50, 1905.
- [39] A. Einstein. The photoelectric effect. *Ann. Phys*, 17:132, 1905.
- [40] T. Esirkepov, M. Borghesi, S. Bulanov, G. Mourou, and T. Tajima. Highly Efficient Relativistic-Ion Generation in the Laser-Piston Regime. *Physical Review Letters*, 92(17):2–5, Apr. 2004.
- [41] J. Faure, Y. Glinec, A. Pukhov, S. Kiselev, S. Gordienko, E. Lefebvre, J. Rousseau, F. Burgy, and V. Malka. A laser–plasma accelerator producing monoenergetic electron beams. *Nature*, 431(7008):541–544, 2004.
- [42] A. P. Fews, P. A. Norreys, F. N. Beg, A. R. Bell, A. E. Dangor, C. N. Danson, P. Lee, and S. J. Rose. Plasma ion emission from high intensity picosecond laser pulse interactions with solid targets. *Phys. Rev. Lett.*, 73:1801–1804, Sep 1994.
- [43] R. Fonseca, L. Silva, F. Tsung, V. Decyk, W. Lu, C. Ren, W. Mori, S. Deng, S. Lee, T. Katsouleas, and Others. OSIRIS: a three-dimensional, fully relativistic particle in cell code for modeling plasma based accelerators. pages 342–351, 2002.
- [44] D. W. Forslund, J. M. Kindel, K. Lee, E. L. Lindman, and R. L. Morse. Theory and simulation of resonant absorption in a hot plasma. *Phys. Rev. A*, 11:679–683, Feb 1975.
- [45] E. Fourkal, B. Shahine, M. Ding, J. S. Li, T. Tajima, and C.-M. Ma. Particle in cell simulation of laser-accelerated proton beams for radiation therapy. *Medical Physics*, 29(12):2788, 2002.
- [46] C. Gahn, G. D. Tsakiris, A. Pukhov, J. Meyer-ter Vehn, G. Pretzler, P. Thirolf, D. Habs, and K. J. Witte. Multi-mev electron beam generation by direct laser acceleration in high-density plasma channels. *Phys. Rev. Lett.*, 83:4772–4775, Dec 1999.

- [47] C. Geddes, C. Toth, J. Van Tilborg, E. Esarey, C. Schroeder, D. Bruhwiler, C. Nieter, J. Cary, and W. Leemans. High-quality electron beams from a laser wakefield accelerator using plasma-channel guiding. *Nature*, 431(7008):538–541, 2004.
- [48] P. Gibbon. *Short pulse laser interactions with matter*. Imperial College Press London, 2005.
- [49] P. Gibbon and E. Förster. Short-pulse laser-plasma interactions. *Plasma Physics and Controlled Fusion*, 38:769, 1996.
- [50] S. Gitomer, R. Jones, F. Begay, A. Ehler, J. Kephart, and R. Kristal. Fast ions and hot electrons in the laser–plasma interaction. *Physics of Fluids*, 29:2679, 1986.
- [51] S. Gordienko, A. Pukhov, O. Shorokhov, and T. Baeva. Relativistic doppler effect: Universal spectra and zeptosecond pulses. *Phys. Rev. Lett.*, 93:115002, Sep 2004.
- [52] S. Hatchett, C. Brown, T. Cowan, E. Henry, J. Johnson, M. Key, J. Koch, A. Langdon, B. Lasinski, R. Lee, et al. Electron, photon, and ion beams from the relativistic interaction of petawatt laser pulses with solid targets. *Physics of Plasmas*, 7:2076, 2000.
- [53] C. Haynam, P. Wegner, J. Auerbach, M. Bowers, S. Dixit, G. Erbert, G. Heestand, M. Henesian, M. Hermann, K. Jancaitis, et al. National ignition facility laser performance status. *Applied optics*, 46(16):3276–3303, 2007.
- [54] B. Hegelich, B. Albright, J. Cobble, K. Flippo, S. Letzring, M. Paffett, H. Ruhl, J. Schreiber, R. Schulze, and J. Fernandez. Laser acceleration of quasi-monoenergetic mev ion beams. *Nature*, 439(7075):441–444, 2006.
- [55] B. Hegelich, D. Jung, B. Albright, J. Fernandez, D. Gautier, C. Huang, T. Kwan, S. Letzring, S. Palaniyappan, R. Shah, et al. Experimental demonstration of particle energy, conversion efficiency and spectral shape required for ion-based fast ignition. *Nuclear Fusion*, 51:083011, 2011.
- [56] A. Henig, S. Steinke, M. Schnürer, T. Sokollik, R. Hörlein, D. Kiefer, D. Jung, J. Schreiber, B. M. Hegelich, X. Q. Yan, J. Meyer-ter Vehn, T. Tajima, P. V. Nickles, W. Sandner, and D. Habs. Radiation-Pressure Acceleration of Ion Beams Driven by Circularly Polarized Laser Pulses. *Physical Review Letters*, 103(24):3–6, Dec. 2009.
- [57] D. Higginson, J. McNaney, D. Swift, T. Bartal, D. Hey, R. Kodama, S. Le Pape, A. Mackinnon, D. Mariscal, H. Nakamura, et al. Laser generated neutron source for neutron resonance spectroscopy. *Physics of Plasmas*, 17:100701, 2010.
- [58] J. Jackson. *Classical electrodynamics*. John Wiley and sons, 1965.

- [59] D. Jung, R. Hörlein, D. Gautier, S. Letzring, D. Kiefer, K. Allinger, B. Albright, R. Shah, S. Palaniyappan, L. Yin, et al. A novel high resolution ion wide angle spectrometer. *Review of Scientific Instruments*, 82(4):3301, 2011.
- [60] D. Jung, L. Yin, B. J. Albright, D. C. Gautier, R. Hörlein, D. Kiefer, A. Henig, R. Johnson, S. Letzring, S. Palaniyappan, R. Shah, T. Shimada, X. Q. Yan, K. J. Bowers, T. Tajima, J. C. Fernández, D. Habs, and B. M. Hegelich. Monoenergetic ion beam generation by driving ion solitary waves with circularly polarized laser light. *Phys. Rev. Lett.*, 107:115002, Sep 2011.
- [61] D. Kaganovich, A. Ting, D. Gordon, R. Hubbard, T. Jones, A. Zigler, and P. Sprangle. First demonstration of a staged all-optical laser wakefield acceleration. *Physics of plasmas*, 12:100702, 2005.
- [62] M. Kaluza, J. Schreiber, M. Santala, G. Tsakiris, K. Eidmann, J. Meyer-ter Vehn, and K. Witte. Influence of the Laser Prepulse on Proton Acceleration in Thin-Foil Experiments. *Physical Review Letters*, 93(4):17–20, July 2004.
- [63] L. Keldysh. Ionization in the field of a strong electromagnetic wave. *Soviet Physics JETP*, 20(5), 1965.
- [64] R. Kingham and A. Bell. *An implicit Vlasov–Fokker–Planck code to model non-local electron transport in 2-D with magnetic fields*, volume 194. Feb. 2004.
- [65] H. Kiriya, M. Mori, Y. Nakai, T. Shimomura, M. Tanoue, A. Akutsu, H. Okada, T. Motomura, S. Kondo, S. Kanazawa, et al. Generation of high-contrast and high-intensity laser pulses using an opcpa preamplifier in a double cpa, ti: sapphire laser system. *Optics Communications*, 282(4):625–628, 2009.
- [66] S. Kneip, C. McGuffey, F. Dollar, M. Bloom, V. Chvykov, G. Kalintchenko, K. Krushelnick, A. Maksimchuk, S. Mangles, T. Matsuoka, et al. X-ray phase contrast imaging of biological specimens with femtosecond pulses of betatron radiation from a compact laser plasma wakefield accelerator. *Applied Physics Letters*, 99(9):093701–093701, 2011.
- [67] S. Kneip, C. McGuffey, J. L. Martins, S. F. Martins, C. Bellei, V. Chvykov, F. Dollar, R. Fonseca, C. Huntington, G. Kalintchenko, A. Maksimchuk, S. P. D. Mangles, T. Matsuoka, S. R. Nagel, C. A. J. Palmer, J. Schreiber, K. T. Phuoc, A. G. R. Thomas, V. Yanovsky, L. O. Silva, K. Krushelnick, and Z. Najmudin. Bright spatially coherent synchrotron X-rays from a table-top source (vol 6, pg 980, 2010). *NATURE PHYSICS*, 7(9):737, SEP 2011.
- [68] R. Kodama, P. Norreys, K. Mima, A. Dangor, R. Evans, H. Fujita, Y. Kitagawa, K. Krushelnick, T. Miyakoshi, N. Miyanaga, et al. Fast heating of ultrahigh-density plasma as a step towards laser fusion ignition. *Nature*, 412(6849):798–802, 2001.

- [69] S. Kohlweyer, G. Tsakiris, C. Wahlström, C. Tillman, and I. Mercer. Harmonic generation from solid-vacuum interface irradiated at high laser intensities. *Optics communications*, 117(5-6):431–438, 1995.
- [70] W. Kruer. *The physics of laser plasma interactions*. Reading, MA (US); Addison-Wesley Publishing Co., 1988.
- [71] W. Kruer and K. Estabrook. J \times b heating by very intense laser light. *Physics of Fluids*, 28:430, 1985.
- [72] W. Kruer and S. Wilks. Kinetic simulations of ultra-intense laser plasma interactions. *Plasma Physics and Controlled Fusion*, 34:2061, 1992.
- [73] L. Landau and E. Lifshitz. *A Course in Theoretical Physics-Fluid Mechanics*. Pergamon Press Ltd., 1987.
- [74] J. Larsen and S. Lane. Hyades—a plasma hydrodynamics code for dense plasma studies. *Journal of Quantitative Spectroscopy and Radiative Transfer*, 51(1-2):179–186, 1994.
- [75] D. Lawrence. Kodak x-omatic and lanex screens and kodak films for medical radiography. *Radiobiologia*, 17(1):2, 1977.
- [76] E. O. Lawrence and M. S. Livingston. The production of high speed light ions without the use of high voltages. *Phys. Rev.*, 40:19–35, Apr 1932.
- [77] W. Leemans, R. Duarte, E. Esarey, S. Fournier, C. Geddes, D. Lockhart, C. Schroeder, C. Toth, J. Vay, S. Zimmermann, et al. The berkeley lab laser accelerator (bella): A 10 gev laser plasma accelerator. In *AIP Conference Proceedings*, volume 1299, page 3, 2010.
- [78] W. Leemans, B. Nagler, A. Gonsalves, C. Toth, K. Nakamura, C. Geddes, E. Esarey, C. Schroeder, and S. Hooker. Gev electron beams from a centimetre-scale accelerator. *Nature physics*, 2(10):696–699, 2006.
- [79] R. Lichters, J. Meyer-ter Vehn, and A. Pukhov. Short-pulse laser harmonics from oscillating plasma surfaces driven at relativistic intensity. *Physics of Plasmas*, 3:3425, 1996.
- [80] J. Lindl and W. Mead. Two-dimensional simulation of fluid instability in laser-fusion pellets. *Physical Review Letters*, 34(20):1273–1276, 1975.
- [81] U. Linz and J. Alonso. What will it take for laser driven proton accelerators to be applied to tumor therapy? *Physical Review Special Topics-Accelerators and Beams*, 10(9):094801, 2007.
- [82] X. Liu, R. Wagner, A. Maksimchuk, E. Goodman, J. Workman, D. Umstadter, and A. Migus. Nonlinear temporal diffraction and frequency shifts resulting from pulse shaping in chirped-pulse amplification systems. *Optics letters*, 20(10):1163–1165, 1995.

- [83] A. Macchi, F. Cattani, T. Liseykina, and F. Cornolti. Laser acceleration of ion bunches at the front surface of overdense plasmas. *Physical review letters*, 94(16):165003, 2005.
- [84] A. Macchi, S. Veghini, T. V. Liseykina, and F. Pegoraro. Radiation pressure acceleration of ultrathin foils. *New Journal of Physics*, 12(4):045013, 2010.
- [85] A. Macchi, S. Veghini, and F. Pegoraro. light sail acceleration reexamined. *Physical review letters*, 103(8):85003, 2009.
- [86] A. Maksimchuk, S. Gu, K. Flippo, D. Umstadter, and V. Y. Bychenkov. Forward ion acceleration in thin films driven by a high-intensity laser. *Phys. Rev. Lett.*, 84:4108–4111, May 2000.
- [87] G. Malka, M. Aeonard, J. Chemin, G. Claverie, M. Harston, V. Tikhonchuk, J. Scheurer, S. Fritzler, V. Malka, P. Balcou, et al. Optimizing photonuclear reactions with a high-intensity laser. In *Proceedings of SPIE*, volume 4510, page 47, 2001.
- [88] V. Malka, S. Fritzler, E. Lefebvre, E. dHumières, R. Ferrand, G. Grillon, C. Albaret, S. Meyroneinc, J. Chambaret, A. Antonetti, et al. Practicability of protontherapy using compact laser systems. *Medical physics*, 31:1587, 2004.
- [89] S. Mangles, C. Murphy, Z. Najmudin, A. Thomas, J. Collier, A. Dangor, E. Divall, P. Foster, J. Gallacher, C. Hooker, et al. Monoenergetic beams of relativistic electrons from intense laser–plasma interactions. *Nature*, 431(7008):535–538, 2004.
- [90] O. E. Martinez. Grating and prism compressors in the case of finite beam size. *J. Opt. Soc. Am. B*, 3(7):929–934, Jul 1986.
- [91] G. Marx. Interstellar vehicle propelled by terrestrial laser beam. *Nature*, 211, 1966.
- [92] S. Masuda, E. Miura, K. Koyama, and S. Kato. Absolute calibration of an electron spectrometer using high energy electrons produced by the laser-plasma interaction. *Review of Scientific Instruments*, 79(8):083301–083301, 2008.
- [93] C. McGuffey. *Studies of Laser Guiding and Electron Injection in a High Power Laser Wakefield Accelerator*. PhD thesis, University of Michigan, Ann Arbor, 2011.
- [94] C. McGuffey, A. G. R. Thomas, W. Schumaker, T. Matsuoka, V. Chvykov, F. J. Dollar, G. Kalintchenko, V. Yanovsky, A. Maksimchuk, K. Krushelnick, V. Y. Bychenkov, I. V. Glazyrin, and A. V. Karpeev. Ionization induced trapping in a laser wakefield accelerator. *Phys. Rev. Lett.*, 104:025004, Jan 2010.

- [95] A. Modena, Z. Najmudin, A. Dangor, C. Clayton, K. Marsh, C. Joshi, V. Malka, C. Darrow, C. Danson, D. Neely, et al. Electron acceleration from the breaking of relativistic plasma waves. *Nature*, 377(6550):606–608, 1995.
- [96] P. Mora. Plasma Expansion into a Vacuum. *Physical Review Letters*, 90(18):5–8, May 2003.
- [97] J. Morrison, M. Storm, E. Chowdhury, K. Akli, S. Feldman, C. Willis, R. Daskalova, T. Growden, P. Berger, T. Ditmire, et al. Selective deuteron production using target normal sheath acceleration. *Physics of Plasmas*, 19(3):030707–030707, 2012.
- [98] G. Mourou and T. Tajima. The extreme light infrastructure: Optics next horizon. *Optics and Photonics News*, 22(7):47–51, 2011.
- [99] K. Nakajima, D. Fisher, T. Kawakubo, H. Nakanishi, A. Ogata, Y. Kato, Y. Kitagawa, R. Kodama, K. Mima, H. Shiraga, K. Suzuki, K. Yamakawa, T. Zhang, Y. Sakawa, T. Shoji, Y. Nishida, N. Yugami, M. Downer, and T. Tajima. Observation of ultrahigh gradient electron acceleration by a self-modulated intense short laser pulse. *Phys. Rev. Lett.*, 74:4428–4431, May 1995.
- [100] D. Neely, D. Chambers, C. Danson, P. Norreys, S. Preston, F. Quinn, M. Roper, J. Wark, and M. Zepf. A multi-channel soft x-ray flat-field spectrometer. In *AIP Conference Proceedings*, volume 426, page 479, 1998.
- [101] K. Nemoto, A. Maksimchuk, S. Banerjee, K. Flippo, G. Mourou, D. Umstadter, and V. Bychenkov. Laser-triggered ion acceleration and table top isotope production. *Applied Physics Letters*, 78:595, 2001.
- [102] J. Nuckolls and L. Wood. Laser compression of matter to super-high densities: Thermonuclear (ctr). *Nature*, 239:139, 1972.
- [103] A. Pak, K. A. Marsh, S. F. Martins, W. Lu, W. B. Mori, and C. Joshi. Injection and trapping of tunnel-ionized electrons into laser-produced wakes. *Phys. Rev. Lett.*, 104:025003, Jan 2010.
- [104] C. Palmer, N. Dover, I. Pogorelsky, M. Babzien, G. Dudnikova, M. Ispiriyani, M. Polyanskiy, J. Schreiber, P. Shkolnikov, V. Yakimenko, and Z. Najmudin. Monoenergetic Proton Beams Accelerated by a Radiation Pressure Driven Shock. *Physical Review Letters*, 106(1):1–4, Jan. 2011.
- [105] M. Passoni, V. Tikhonchuk, M. Lontano, and V. Bychenkov. Charge separation effects in solid targets and ion acceleration with a two-temperature electron distribution. *Physical Review E*, 69(2):1–11, Feb. 2004.
- [106] P. Patel, A. Mackinnon, M. Key, T. Cowan, M. Foord, M. Allen, D. Price, H. Ruhl, P. Springer, and R. Stephens. Isochoric heating of solid-density matter with an ultrafast proton beam. *Physical review letters*, 91(12):125004, 2003.

- [107] G. Petrov, O. Albert, J. Etchepare, and S. Saltiel. Cross-polarized wave generation by effective cubic nonlinear optical interaction. *Optics Letters*, 26(6):355–357, 2001.
- [108] T. Popmintchev, M. Chen, D. Popmintchev, P. Arpin, S. Brown, S. Ališauskas, G. Andriukaitis, T. Balčiunas, O. Mücke, A. Pugzlys, et al. Bright coherent ultrahigh harmonics in the keV x-ray regime from mid-infrared femtosecond lasers. *Science*, 336(6086):1287–1291, 2012.
- [109] A. Pukhov. Three-dimensional simulations of ion acceleration from a foil irradiated by a short-pulse laser. *Physical review letters*, 86(16):3562–3565, 2001.
- [110] S. Reed, V. Chvykov, G. Kalintchenko, T. Matsuoka, P. Rousseau, V. Yanovsky, C. Vane, J. Beene, D. Stracener, D. Schultz, et al. Photonuclear fission with quasimonoenergetic electron beams from laser wakefields. *Applied physics letters*, 89:231107, 2006.
- [111] S. A. Reed. *ELECTRON AND PROTON ACCELERATION USING THE 30 TW , 30 fs HERCULES LASER*. PhD thesis, 2008.
- [112] A. Robinson, A. Bell, and R. Kingham. Effect of target composition on proton energy spectra in ultraintense laser-solid interactions. *Physical review letters*, 96(3):35005, 2006.
- [113] A. Robinson, D. Neely, P. McKenna, and R. Evans. Spectral control in proton acceleration with multiple laser pulses. *Plasma Physics and Controlled Fusion*, 49:373, 2007.
- [114] A. P. L. Robinson, M. Zepf, S. Kar, R. G. Evans, and C. Bellei. Radiation pressure acceleration of thin foils with circularly polarized laser pulses. *New Journal of Physics*, 10(1):013021, Jan. 2008.
- [115] M. Roth, T. Cowan, M. Key, S. Hatchett, C. Brown, W. Fountain, J. Johnson, D. Pennington, R. Snavely, S. Wilks, et al. Fast ignition by intense laser-accelerated proton beams. *Physical review letters*, 86(3):436–439, 2001.
- [116] R. M. Russell. The cray-1 computer system. *Commun. ACM*, 21(1):63–72, Jan. 1978.
- [117] W. Schumaker, N. Nakanii, C. McGuffey, C. Zulick, V. Chvykov, F. Dollar, G. Kalinchenko, A. Maksimchuk, K. A. Tanaka, A. G. R. Thomas, V. Yanovsky, and K. Krushelnick. Ultrafast electron beam radiography of self-generated magnetic fields from high intensity laser-solid interactions. Submitted 2012.
- [118] H. Schwoerer, S. Pfotenhauer, O. Jäckel, K. Amthor, B. Liesfeld, W. Ziegler, R. Sauerbrey, K. Ledingham, and T. Esirkepov. Laser-plasma acceleration of quasi-monoenergetic protons from microstructured targets. *Nature*, 439(7075):445–448, 2006.

- [119] Y. Shimomura, R. Aymar, V. Chuyanov, M. Huguet, R. Parker, and I. Team. Iter overview. *Nuclear Fusion*, 39:1295, 1999.
- [120] R. A. Snavely, M. H. Key, S. P. Hatchett, T. E. Cowan, M. Roth, T. W. Phillips, M. A. Stoyer, E. A. Henry, T. C. Sangster, M. S. Singh, S. C. Wilks, A. MacKinnon, A. Offenberger, D. M. Pennington, K. Yasuike, A. B. Langdon, B. F. Lasinski, J. Johnson, M. D. Perry, and E. M. Campbell. Intense high-energy proton beams from petawatt-laser irradiation of solids. *Phys. Rev. Lett.*, 85:2945–2948, Oct 2000.
- [121] D. Strickland and G. Mourou. Compression of amplified chirped optical pulses. *Optics Communications*, 56(3):219 – 221, 1985.
- [122] M. Tabak, J. Hammer, M. Glinsky, W. Kruer, S. Wilks, J. Woodworth, E. Campbell, M. Perry, and R. Mason. Ignition and high gain with ultra-powerful lasers@ f—. *Physics of Plasmas*, 1:1626, 1994.
- [123] M. Tatarakis, I. Watts, F. Beg, E. Clark, A. Dangor, A. Gopal, M. Haines, P. Norreys, U. Wagner, M. Wei, et al. Measuring huge magnetic fields. *Nature*, 415(6869):280–280, 2002.
- [124] I. Thomann, A. Bahabad, X. Liu, R. Trebino, M. Murnane, and H. Kapteyn. Characterizing isolated attosecond pulses from hollow-core waveguides using multi-cycle driving pulses. *Optics express*, 17(6):4611–4633, 2009.
- [125] A. Thomas, R. Kingham, and C. Ridgers. Rapid self-magnetization of laser speckles in plasmas by nonlinear anisotropic instability. *New Journal of Physics*, 11:033001, 2009.
- [126] A. Thomas and K. Krushelnick. Betatron x-ray generation from electrons accelerated in a plasma cavity in the presence of laser fields. *Physics of Plasmas*, 16:103103, 2009.
- [127] A. G. Thomas. *Studies of Laser Propagation and Mono-Energetic Electron Beam Injection in Laser-Wakefield Accelerators*. PhD thesis, 2006.
- [128] T. Toncian, M. Borghesi, J. Fuchs, E. d’Humières, P. Antici, P. Audebert, E. Brambrink, C. Cecchetti, A. Pipahl, L. Romagnani, et al. Ultrafast laser-driven microlens to focus and energy-select mega-electron volt protons. *Science*, 312(5772):410–413, 2006.
- [129] E. Treacy. Optical pulse compression with diffraction gratings. *Quantum Electronics, IEEE Journal of*, 5(9):454–458, 1969.
- [130] D. Umstadter, S. Chen, A. Maksimchuk, G. Mourou, and R. Wagner. Nonlinear optics in relativistic plasmas and laser wake field acceleration of electrons. *Science*, 273(5274):472–475, 1996.

- [131] H. Vincenti and F. Quéré. Attosecond lighthouses: How to use spatiotemporally coupled light fields to generate isolated attosecond pulses. *Physical Review Letters*, 108(11):113904, 2012.
- [132] C. Wagner and N. Harned. Euv lithography: Lithography gets extreme. *Nature Photonics*, 4(1):24–26, 2010.
- [133] I. Watts, M. Zepf, E. Clark, M. Tatarakis, K. Krushelnick, A. Dangor, R. Allott, R. Clarke, D. Neely, and P. Norreys. Measurements of relativistic self-phase-modulation in plasma. *Physical Review E*, 66(3):036409, 2002.
- [134] E. W. Weisstein. Wolfram alpha computational engine. From MathWorld—A Wolfram Web Resource. Last visited on 6/20/2012.
- [135] S. Wilks, W. Kruer, and W. Mori. Odd harmonic generation of ultra-intense laser pulses reflected from an overdense plasma. *Plasma Science, IEEE Transactions on*, 21(1):120–124, feb 1993.
- [136] S. Wilks, W. Kruer, M. Tabak, and A. Langdon. Absorption of ultra-intense laser pulses. *Physical review letters*, 69(9):1383–1386, 1992.
- [137] S. Wilks, A. Langdon, T. Cowan, M. Roth, M. Singh, S. Hatchett, M. Key, D. Pennington, A. MacKinnon, and R. Snavely. Energetic proton generation in ultra-intense laser–solid interactions. *Physics of Plasmas*, 8:542, 2001.
- [138] L. Willingale. *Ion Acceleration from High Intensity Laser Plasma Interactions : Measurements and Applications*. PhD thesis, 2007.
- [139] L. Willingale, G. Petrov, A. Maksimchuk, J. Davis, R. Freeman, T. Matsuoka, C. Murphy, V. Ovchinnikov, L. Van Woerkom, and K. Krushelnick. Front versus rear side light-ion acceleration from high-intensity laser–solid interactions. *Plasma Physics and Controlled Fusion*, 53:014011, 2011.
- [140] R. R. Wilson. Radiological use of fast protons. *Radiology*, 47(5):487–491, 1947.
- [141] H. Winick. The linac coherent light source (lcls): a fourth-generation light source using the slac linac. *Journal of electron spectroscopy and related phenomena*, 75:1–8, 1995.
- [142] X. Q. Yan, C. Lin, Z. M. Sheng, Z. Y. Guo, B. C. Liu, Y. R. Lu, J. X. Fang, and J. E. Chen. Generating high-current monoenergetic proton beams by a circularly polarized laser pulse in the phase-stable acceleration regime. *Phys. Rev. Lett.*, 100:135003, Apr 2008.
- [143] V. Yanovsky, V. Chvykov, G. Kalinchenko, P. Rousseau, T. Planchon, T. Matsuoka, A. Maksimchuk, J. Nees, G. Cheriaux, G. Mourou, et al. Ultra-high intensity-300-tw laser at 0.1 hz repetition rate. *Optics Express*, 16(3):2109–2114, 2008.

- [144] V. Yanovsky, C. Felix, and G. Mourou. High-energy broad-band regenerative amplifier for chirped-pulse amplification. *Selected Topics in Quantum Electronics, IEEE Journal of*, 7(4):539–541, 2001.
- [145] L. Yin, B. Albright, B. Hegelich, and J. Fernandez. GeV laser ion acceleration from ultrathin targets: The laser break-out afterburner. *Laser and Particle Beams*, 24(02):291–298, 2006.
- [146] M. Yoshida, Y. Fujimoto, Y. Hironaka, K. Nakamura, K. Kondo, M. Ohtani, and H. Tsunemi. Generation of picosecond hard x rays by tera watt laser focusing on a copper target. *Applied physics letters*, 73:2393, 1998.
- [147] M. Zepf, G. Tsakiris, G. Pretzler, I. Watts, D. Chambers, P. Norreys, U. Andiel, A. Dangor, K. Eidmann, C. Gahn, et al. Role of the plasma scale length in the harmonic generation from solid targets. *Physical Review E*, 58(5):5253–5256, 1998.